Equilibrium quantum phases and quench dynamics of dipolar bosons in 2D optical lattices

A thesis submitted in partial fulfilment of

the requirements for the degree of

Doctor of Philosophy

by

Hrushikesh Sable

(Roll No. 17330015)

Under the supervision of

Prof. Angom Dilip Kumar Singh

Professor

Department of Physics, Manipur University

(formerly at Physical Research Laboratory, Ahmedabad, India)

DISCIPLINE OF PHYSICS

INDIAN INSTITUTE OF TECHNOLOGY GANDHINAGAR

2022

to

Mummy, Papa, and Pushkar,

for your unconditional love and support

Declaration

I declare that this written submission represents my ideas in my own words and where others' ideas or words have been included, I have adequately cited and referenced the original sources. I also declare that I have adhered to all principles of academic honesty and integrity and have not misrepresented or fabricated or falsified any idea/data/fact/source in my submission. I understand that any violation of the above will be cause for disciplinary action by the Institute and can also evoke penal action from the sources which have thus not been properly cited or from whom proper permission has not been taken when needed.

Signature

Name: Hrushikesh Sable

(Roll No: 17330015)

Date:

CERTIFICATE

It is certified that the work contained in the thesis titled **Equilibrium quantum phases and quench dynamics of dipolar bosons in 2D optical lattices** by Mr. Hrushikesh Sable (Roll No. 17330015), has been carried out under my supervision and that this work has not been submitted elsewhere for a degree.

Prof. Angom Dilip Kumar Singh
Professor
Theoretical Physics Division,
Physical Research Laboratory,
Ahmedabad, India.

(Thesis Supervisor)

Date:

Thesis Approval

The thesis entitled

Equilibrium quantum phases and quench dynamics of dipolar bosons in 2D optical lattices

by

Hrushikesh Sable

(Roll No. 17330015)

is approved for the degree of

Doctor of Philosophy

_____	_____
Examiner	Examiner
_____	_____
Supervisor	Chairman

Date: _____

Place: _____

Acknowledgments

Abstract

The emergence of novel phases of matter at low temperatures has been a motivation to cool systems to lowest temperatures possible. At low temperatures, quantum statistics become important and the quantum fluctuations dominate over the thermal fluctuations. These fluctuations drive the quantum phase transitions (QPTs) which are associated with a change in the ground state of the system Hamiltonian. The bosonic quantum gases cooled to quantum degeneracy temperatures exhibit the Bose-Einstein condensation phenomena, which corresponds to the macroscopic occupation of the lowest energy single particle level. These Bose Einstein condensate (BEC) atoms when loaded in optical lattice potentials can exhibit the quantum phases in the strongly interacting domain; and are novel quantum systems to study the quantum many-body physics and QPTs. In this thesis, we investigate the quantum phases of the neutral and dipolar ultracold bosonic gases trapped in square lattice, and the quench dynamics across the QPTs exhibited by these systems. Furthermore, we also study the quantum phases and phase transitions of these atoms loaded in disordered lattice potentials.

We study the quantum phases of the dipolar quantum gases, in particular, the parameter domain of the novel supersolid (SS) phase. The SS phase exhibits the properties of being a solid and a superfluid simultaneously. We model the system with the extended Bose-Hubbard model and obtain the ground state phase diagrams. We utilize the single-site Gutzwiller mean-field (SGMF) and cluster Gutzwiller mean-field (CGMF) to obtain the ground states of the model. As a result of the quantum fluctuations incorporated in the CGMF method, the parameter domain of the SS phase is shrinked in comparison to the one obtained with the SGMF method. We also perform a cluster finite size scaling to find out the critical points of the QPTs in the exact calculation limit, demonstrating the role of quantum fluctuations. Furthermore, we show that the presence of the artificial gauge field enlarges the domain of the SS phase. This enlargement is due to the localizing effect of the Landau quantization due to the artificial gauge fields. We numerically demonstrate the gauge invariance of the phase boundaries obtained using the SGMF and CGMF methods.

Next, we study the dynamics associated with quenching a parameter of the system Hamiltonian across the critical point, over a finite time duration. We study the

spontaneous symmetry breaking and the order parameter development in the dynamics following the Kibble-Zurek (KZ) mechanism. The KZM categorizes the entire dynamics into three temporal regimes based on the competition between the relaxation time and the quenching rate. And it predicts the power-law scaling of certain quantities like the correlation length and the amount of defects generated as a function of quench rate. In this thesis, we consider quenching across certain second-order QPTs like the Mott-Insulator to superfluid QPT of the Bose-Hubbard model (BHM) and the stripe density wave to stripe supersolid QPT of the dipolar BHM and investigate the KZ scaling laws. The scaling exponents obtained also satisfy the expected scaling relations. Next, we consider quenching the polarizing angle of the dipoles which results in the structural QPT from the stripe ordering to the checkerboard ordering in the system. We demonstrate the power-law scaling of the number of checkerboard ordered domains formed in the dynamics, which is reminiscent of the KZM.

Apart from studying the atoms in "clean" lattice potentials, we also investigate the quantum phases in disordered lattice potentials. In particular, the Bose glass (BG) phase, characterized by SF islands in an MI background emerges, when the disorder is present. We apply the methods of percolation theory and numerically identify the SF domains in the BG phase and study their average size (or the correlation length). As the SF phase is approached, there is a divergence of the correlation length, and the critical exponent is in good agreement with the value predicted by the 2D site percolation universality class. This suggests that the BG-SF phase transition belongs to 2D site percolation class of transitions.

Contents

List of Figures

Chapter 1

Introduction

There has been a long interest in understanding the phases of matter and the associated phase transitions between different phases. Initial understanding was based on studying the phase transitions induced by changing the temperature - phase transition from ice to water to vapour phase; paramagnetic to ferromagnetic transition of Ising spin chain are some well-known examples of the thermal phase transitions. Apart from the temperature, certain phase transitions can also be induced by a change in the pressure. However, there exist an entirely different class of phase transitions primarily concerned to quantum systems. Phase transitions in these systems occur when a parameter of the underlying Hamiltonian of the quantum system is changed. This is an important distinction from the classical phase transitions where the change in external parameters induce the transition. Another important difference lies in the nature of the fluctuations. The classical phase transitions are driven by the thermal fluctuations while the quantum phase transitions (QPTs) are through the quantum fluctuations. The quantum fluctuations arise from the uncertainty principle. The ground state energy becomes non-analytic at the critical point of the QPTs. This non-analyticity is associated with a level crossing or an avoided level crossing [1, 2] between the ground state and the excited state. Furthermore, the closing of the gap between the ground and excited state determines the critical exponents of the QPT.

To study the QPTs, it is important that the quantum fluctuations dominate over the thermal fluctuations, suggesting that these transitions should be studied at extreme low temperatures. This is because at such low temperatures, the thermal de-Broglie wave-

length of the particles of mass m, given as $\lambda_{\mathrm{dB}} = h/\sqrt{2\pi m k_{\mathrm{B}} T}$, overlap with one another and the quantum degeneracy effects can be observed. Experimental advances in laser cooling of the vapours of atomic gases enabled to reach temperatures in μK order, but was insufficient to observe the quantum mechanical degeneracy. However, with the further evaporative cooling technique, the temperature could be further lowered to nK. These novel cooling techniques were honored with Nobel prize in 1997 [3–5].

An immediate consequence of the experimental achievement of cooling to extreme low temperatures was the observation of Bose-Einstein condensation of dilute atomic gases in the laboratory experiments [6]. The Bose-Einstein condensation refers to the macroscopic occupation of bosonic particles in the lowest single particle state of the system [7] and is a direct consequence of the Bose-Einstein distribution relying on the indistinguishably of the bosonic particles. The Bose-Einstein distribution and the condensation phenomenon were predicted by Albert Einstein [8] following the work of the Satyendra Nath Bose on the quantum statistics of photons [9]. The ground breaking work of Bose also explained the Planck's law of the blackbody radiation. However, this theoretical prediction could be verified experimentally as the Bose-Einstein condensates (BECs) could be created nearly 70 years later due the developments in cooling techniques. The BEC is a state of matter and is characterized by a coherent macroscopic giant matter wave. The coherent nature of the BEC is expressed using the off-diagonal long-range order (ODLRO), defined such that the off-diagonal matrix element of the one-body density matrix is non-zero. The coherent nature of BEC is extremely efficient as the quantum mechanical effects can be observed and investigated at the length scales of μm. Most BECs realized in laboratory experiments are of alkali atoms. This is because the alkali atoms have relatively simpler electronic structure with one electron in the valence orbit which is beneficial in developing cooling strategies based on laser cooling. The density of these alkali gases in the BEC state is around $10^{13} - 10^{15}\mathrm{cm}^{-3}$, which means that they are dilute than the air at room temperature which have densities around $10^{19}\mathrm{cm}^{-3}$. These ultralow densities are required to prevent the formation of the solid phase of matter at low temperatures, which usually is thermodynamically stable phase at such low temperatures. Due to such low densities,

the interactions among the constituent particles are weak, and is approximated with a pseudo contact potential

$$U_{\text{int}} = g\delta(\mathbf{r} - \mathbf{r}'), \tag{1.1}$$

where g is the strength of the contact interaction. The strength of this contact interaction can be controlled by Feshbach resonance [10]. Thus the theoretical and experimental research on the BECs initially focused on the weakly interacting BECs. However, by loading these cold Bose condensed atoms in optical lattices, it became possible to study the strongly correlated physics, as we shall discuss in the next section.

1.1 BECs in optical lattice

Optical lattices are periodic potentials of light created by superimposing counter-propagating pair(s) of laser beams. There is a conservative as well as dissipative interaction of the Bose condensed ultracold atoms with the laser light. The conservative interaction involves an induced dipole moment in the atoms that leads to the ac-Stark shift. The dissipative interaction is due to the absorption of the photons of light by the atoms. When the laser light is off-resonant with the resonances of the atoms, this process is suppressed. Then the only conservative interaction leads to a potential periodic "layout" in which the atoms occupy the potential wells. One crucial aspect is that the depth of these potential wells is proportional to the intensity of the laser beams, which can be controlled in lab. Another useful feature of these systems is that by changing the angle between the laser beams, different lattice geometries like the honeycomb [11, 12], triangular [13, 14] and kagome [15, 16] lattices can be synthesized. Furthermore, they offer an unparalleled control over the dimensionality of the lattice, interatomic interaction strength and number of atoms trapped in the lattice. As such, these are clean systems and are free of any defects. However, there are controlled ways of introducing the disorder in the lattice potentials which is an additional advantage of these systems. These systems have a minimal interaction with the environment, and hence are excellent proxy to the closed quantum systems. Ultracold atoms trapped in optical lattices resemble the electrons moving in the periodic potential in the atoms in condensed mat-

ter systems. Therefore various studies of the condensed matter physics can be done using the ultracold atoms, however, with greater experimental tunability.

As discussed earlier, the ultracold atomic gases are dilute systems. However, when trapped in optical lattice, the kinetic energy analogue - the quantum mechanical tunneling between the wells, can be tuned and made smaller for deep lattice wells. Then, the itinerancy of the atoms is reduced and the system can be driven into the strongly interacting regime. These strong interactions lead to localization of atomic wavefunctions and the system exhibits the Mott Insulator (MI) phase. In the opposite limit of low-interaction strength, the atoms possess itinerant behaviour and are in the coherent superfluid (SF) phase. Therefore, by varying the depth of the lattice wells, the QPT from the MI to SF phase is studied [17, 18]. The potential field for a one-dimensional optical lattice can be written as

$$V(x) = V_0 \cos^2(kx), \tag{1.2}$$

where $k = 2\pi/\lambda$ and λ is the wavelength of the laser. The above equation can be generalized to 2D and 3D optical lattices.

The experimental demonstration of the SF-to-MI QPT [17] has lead to numerous research works to study the QPTs. Theoretically, the system is modeled with the Bose-Hubbard model (BHM) [19, 20] which is the bosonic version of the Hubbard model [21]. The model describes the competition between the hopping of atoms with strength J and the onsite interaction of strength U and is apt to describe the interacting bosons in a lattice. For low J/U, the system is in MI phase and the atomic wavefunctions are localized at lattice sites. While for high J/U, the system is in SF phase and the atomic wavefunctions are delocalized over the system. This indicates the ODLRO of the SF phase. The description of the BHM and the details of the quantum phases of it is in Chapter 2.

Apart from the BECs of neutral atoms, experimental advances have enabled cooling the atomic gases possessing a permanent magnetic dipole moment or polar molecules featuring an electric dipole moment. The BECs of dipolar chromium (Cr) [22, 23], dysprosium (Dy) [24], erbium (Er) [25–28] atoms have been realized in experiments. Very recently, this year (2022), the BEC of europium (Eu) has been claimed [29]. Ultracold polar molecules, possessing a high electric dipole moment, have also been

experimentally cooled to quantum degeneracy temperatures [30–34]. Both the dipolar atoms and the polar molecules interact due to the dipole- dipole interaction in addition to the contact interaction -

$$U_{\text{int}}(\mathbf{r}-\mathbf{r}^{'}) = g\delta(\mathbf{r}-\mathbf{r}^{'}) + \frac{C_{\text{dd}}\left(1-3\text{cos}^2\alpha_{\mathbf{r},\mathbf{r}'}\right)}{|\mathbf{r}-\mathbf{r}^{'}|^{\mathbf{3}}} \tag{1.3}$$

The important feature of this dipole-dipole interaction is that it is long-ranged and is anisotropic due to the $\alpha_{\mathbf{r},\mathbf{r}'}$ factor, which leads to novel phenomena like the Rosensweig instability [35], supersolidity and self-organized structures [36].

Theoretically, the dipole-dipole interaction modifies the BHM Hamiltonian with an additional dipolar interaction term. The dipolar BHM leads to novel quantum phases that have a periodic density modulation, or in other words, are structured quantum phases. For the BHM, the incompressible MI phase has an uniform density distribution, and has integer occupancy. However with the dipole-dipole interaction terms, there are fractional filling incompressible quantum phases [37–39]. The incompressible quantum phases arising in the presence of long-range dipolar interaction are discussed in Chapter 3. Apart from the incompressible phases, the dipolar BHM also exhibits the novel supersolid (SS) phase. This is perhaps one of the most important advantage of using the dipolar BECs as the quest for the SS phase has been long. We shall discuss the phenomenon of supersolidity in the next subsection.

1.1.1 Supersolid phase

Supersolidity is a counter-intuitive phenomenon as it combines the properties of a solid and a superfluid. This phase has a periodic density modulation, or the diagonal long-range order, which is a characteristic property of a solid. And, it also exhibits the ODLRO which means it has dissipation-less flow that of a superfluid. In terms of the symmetry, it breaks the $U(1)$ gauge invariance and the translational symmetry. The SS phase had been theoretically proposed around 1970s [40–43], against the proof of Onsager and Penrose stating that the state with crystalline order cannot be Bose condensed [44]. The initial predictions were to study the superflow in solid ^{4}He [45]. The experimental observation of supersolidity in this system has remained elusive [46–49]. However, there has been a recent surge of interest in investigating and studying

the SS phase following the remarkable theoretical insights and experimental advances in ultracold atoms in optical lattices.

The tunable interactions of the ultracold atoms make them ideal candidates to observe the supersolidity. As the SS phase has an underlying periodic density modulation, it is important that the interaction is momentum dependent. This also explains why the neutral ultracold atoms interacting via the contact pseudopotential do not exhibit the SS phase. The presence of a roton minimum (like in the ^{4}He) for the dipolar BECs was shown in [50], and this initiated a quest of the SS phase using the dipolar atoms [51–55]. Apart from the dipolar atomic gases, this phase also emerges with the cavity-mediated long-range interactions [56–59] and spin-orbit coupled BECs [60–62], Rydberg atoms [63, 64]. Furthermore, the excitation spectrum and various properties of SS phase have been observed in recent quantum gas experiments [65–67].

Theoretically, the existence of the SS phase has been studied using the dipolar BHM model. In most studies, the long-range dipolar interaction terms are restricted to the nearest-neighbours (NN), and then the resulting model is the extended BHM (eBHM). The dipolar interaction strength between two lattice sites is determined by the Wannier functions overlap which decreases exponentially as the inter-site separation is increased. Hence approximating the long-range dipolar interaction with NN interaction provides a good qualitative description of the quantum phases supported by the system [68]. However, theoretical calculations have demonstrated that the SS phase is unstable towards the phase separation for hardcore bosons interacting upto NN sites in bipartite lattices [69–71]. The hardcore bosons means that occupancy of more than one atom at a site is prohibited, which is the case when the onsite repulsive interaction is very high. The phase separation leads to separate solid and superfluid phases with the formation of domain wall and no supersolid phase. However, with the incorporation of next-nearest neighbour interaction in the eBHM, the SS phase can be stabilized for the hardcore bosons. Also, studies have demonstrated that the soft-core bosons interacting upto NN can lead to stable SS phase [72–74]. This is due to the larger Fock-space and higher number fluctuations. The existence and stability of supersolidity have also been confirmed for bosons with infinite-range cavity-mediated interactions [75]. The SS phase has been explored in various lattice systems, such as

one-dimensional (1D) chain [76, 77] and ladder [78], two-dimensional (2D) square [73, 79–84], triangular [85–90], honeycomb [70, 71], kagome [91, 92], bilayer lattice of dipolar bosons [93], and three-dimensional (3D) cubic lattice [81, 94, 95]. The properties of this phase have been reviewed in [96]. We shall discuss the phase diagrams of the eBHM for softcore bosons in 2D square lattice and the parameter domain of the SS phase in Chapter 3.

1.1.2 Artificial gauge fields

Ultracold atoms trapped in optical lattices are charge neutral, and hence cannot experience a Lorentz force. However, several novel experimental approaches like the laser assisted tunneling [97, 98], dynamical shaking [99] have been developed to engineer or simulate the effect of magnetic field on the cold atoms. One of the main motivations towards this direction is to study the Fractional Quantum Hall effect (FQH) using the ultracold atoms in optical lattice. The magnetic flux to obtain the FQH states require magnetic fields of the order of 100T with the electrons moving in a periodic potential in atoms and subjected to magnetic fields, which makes the study difficult. However, with the ultracold atoms, as the lattice spacing is relatively larger, the magnetic flux piercing through an unit call can be tuned to large values and then the study of FQH states can be done. Several tutorials and reviews on the realization of the bosonic analogoes of the FQH states using cold atoms are [100–103].

The effect of the gauge fields on the quantum phases of the cold atoms have also been investigated in detail. In general, the cyclotronic motion of the atoms due to the gauge potential leads to an enhanced localization of the quantum phases. For instance, the parameter domain of the MI phase is enlarged when the gauge field is applied [104]. Similarly, the Bose-glass phase, which is an insulating yet compressible phase that emerges in the presence of disordered potential, enhances in the presence of the gauge fields [105]. The eBHM with artificial gauge field has been studied to examine the fractional quantum Hall [104] and vortex-solid states [106]. In Chapter 3, we shall study the effect of the gauge fields on the parameter domain of the SS phase.

1.2 Quantum quench dynamics

The study of the dynamical evolution of the quantum mechanical state is immensely important and extensively studied. The equilibrium conditions are often an idealization and hence it is important to study the out-of-equilibrium dynamics of these quantum systems. There are different ways to take a quantum mechanical system out of equilibrium. For instance, by connecting the system to a bath, energies and particles are pumped in the system, and their transport is studied. Due to the bath, the system is not a closed system. And so the dynamics of the system is not unitary. Another way to take system out of equilibrium concerns the variation of the parameter(s) of the governing Hamiltonian of the quantum system. In this process, the equilibrium state corresponding to the initial parameter regime becomes unstable, and evolves unitarily under the new Hamiltonian. This process of changing the parameter of the Hamiltonian, either slowly or suddenly, is referred as the quantum quench. There are various research pursuits in this broad field - thermalization and relaxation of quantum systems after a quench [107, 108], spontaneous symmetry breaking and the associated universal scaling laws [109–112], phase ordering kinetics and domain growth laws after a sudden quench [113, 114] to list a few. Apart from the theoretical studies, the experimental advances in these research pursuits have been made using the ultracold atoms. Ultracold atoms in optical lattice have a very minimal interaction with the environment, making them ideal candidates of closed quantum systems. The observation of the MI to SF QPT using the ultracold atoms [17, 18] provided a major impetus to study the dynamics across QPTs.

1.2.1 Kibble-Zurek mechanism

An important and extensively studied problem in quench dynamics involves the slow quenching of a parameter of a Hamiltonian (with a finite rate) across the quantum critical point (QCP) involving two quantum phases. A crucial theoretical framework to study the spontaneous symmetry breaking and the associated formation of domains of order parameter values in such problems is the Kibble-Zurek mechanism (KZM). This theory predicts the formation of topological defects when quenched across (or to) the

QCP, and the scaling of the density of these defects with the quench rate [111, 112]. As the quench rate is decreased, the density of the defects produced in the dynamics also decreases. This problem is one remarkable example of the congruence of the high and low energy physics, as this problem was first encountered and solved by Tom Kibble in the context of cosmology [109] and was later generalized to condensed matter systems by W.H. Zurek [110, 115]. We shall discuss the KZM in detail and derive the KZ scaling laws in Chapter 4.

The theoretical predictions of the KZM were experimentally verified qualitatively [116] and quantitatively [117, 118] using the superfluid ^{3}He and ^{4}He. For the ^{4}He, only the $U(1)$ gauge symmetry is broken across the superfluid transition. However in ^{3}He, there is a superposition of broken spin rotation, broken orbital rotation and broken gauge symmetries ($SO(3)^S \times SO(3)^L \times U(1)$) which has better resemblance with the early universe cosmological phase transitions [117]. Apart from the superfluid helium, other systems like the liquid crystals [119, 120], superconducting loops [121–123], ferroelectrics [124], ion traps [125–128] have been used to test the KZM. These early investigations were developed and investigated for quenches across the thermal phase transitions. Later it was extended to the dynamics of quantum phase transitions [129, 130].

1.2.2 Quench dynamics using ultracold atoms

Ultracold atoms have been used to study the quench dynamics problem and the KZM physics. Initial investigations were for the quenches across the BEC transition and the associated defect production [131–134]. They have also been used to study the phase ordering kinetics and the domain growth studies across the BEC transition [135]. After the extension of the KZM to the QPTs, the quantum quenches using the ultracold atoms in optical lattices have been investigated in detail. There are experimental studies concerning the quenches across the zero temperature QPTs [136–141] using these systems.

In a recent experiment [142], the dynamics of QPT from MI to SF phase has been studied by linearly varying down the lattice depth using the ^{39}K atoms. After the ramp time, the lattice potentials were switched off and the time-of-flight absorption

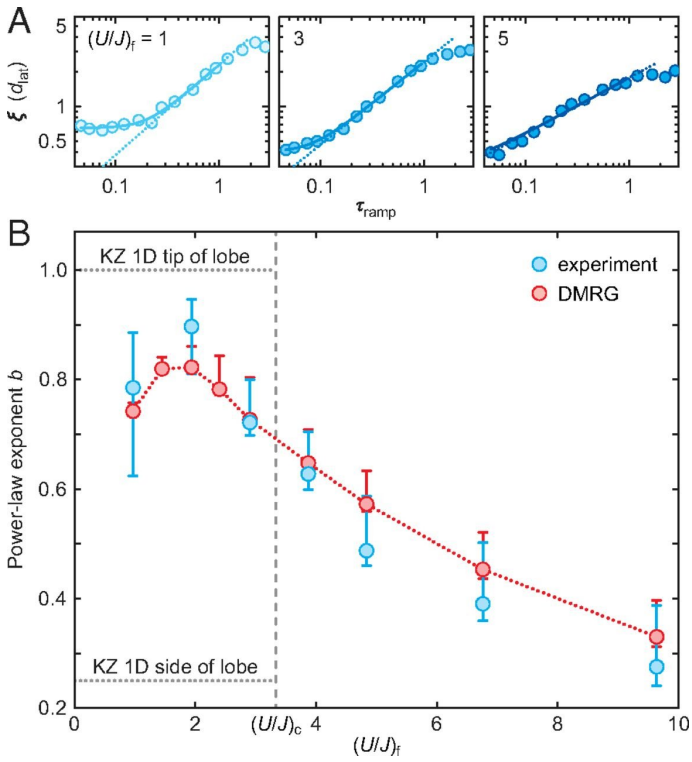

Figure 1.1: The power-law scaling of the coherence length as a function of the ramp time τ_{ramp} for the quench across the MI-SF QPT in 1D lattice, as obtained in the experimental work in [142]. For intermediate range of τ_{ramp}, the coherence length follows a power-law scaling. The exponent b of the coherence length is dependent on the final value of U/J and inconsistent with the value predicted by KZM $(b = 1)$. However, there is a good agreement between the experimental and numerically obtained exponent b. Reprinted figure from [Braun *et* al., PNAS 112 (12), (2015).] Copyright © 2015, Proceedings of the National Academy of Sciences.

images were obtained. The width of the interference peaks in these images was used to obtain the coherence length. As expected, the coherence length grows as the system enters the SF phase, and the growth is dependent on the quenching rate as illustrated in Fig. 1.1. For slower quenches, or larger τ_{ramp}, the coherence length is larger. The ramp times considered in the experiment ensure no mass transport, leading to a fixed density transition between the MI to SF phase.

In this experiment, the coherence length obtained fits with a power-law for intermediate values of τ_{ramp}. Theoretical simulations using the DMRG were done and as illustrated in the figure, are in good agreement with the experimental values. However,

the critical exponent of the coherence length b is seen to be dependent on the final U/J, and not in accordance with the value predicted by the KZM $(b = 1)$. Similar conclusion was drawn for the 2D system, as the exponent b obtained experimentally was in the range $0.6 - 0.7$, while the value of b based on the KZM is 0.4. Hence these discrepancies call for additional theoretical work to investigate the dynamics of quantum systems across the QPTs. Following this motivation, [143] have investigated the dynamics across the MI-SF QPT at the tip of the MI lobe. However, the scaling exponents obtained do not exhibit the scaling relations. We have investigated this QPT in detail, as we shall see in Chapter 4, and have shown that the scaling exponents obey the scaling relations. Furthermore, we have also demonstrated the scaling of the number of SF domains formed in the dynamics, and have shown the equivalence between the scaling of the topological defects and of the number of domains. In chapter 4, we shall also demonstrate the KZ scaling for the dynamics across the first order QPT between the striped to checkerboard supersolid phase for the dipolar bosons.

1.3 Highlights of the thesis

The list of research work done in this dissertation is as follows:

- We have presented a novel algorithm that we have developed to study the cluster identification and percolation theory. We have discussed in detail the steps of the algorithm, and have demonstrated its supremacy in terms of speed and efficiency with respect to existing standard cluster identification algorithms.

- We have examined the phase diagrams of the eBHM for two-dimensional square lattice and have studied the effect of the artificial gauge field on the parameter domains of the quantum phases in the phase diagram.

- We have examined the quantum quench dynamics across the MI-SF quantum phase transition. We have obtained the KZ scaling laws for impulse-adiabatic crossover time instant $\hat{t}$, the correlation length of the system $\hat{\xi}$, and the vortex density $N_v(\hat{t})$. Our study reveals that the KZ scaling exponents for the MI-SF quench exhibits the scaling relations.

- We have systematically obtained the impulse-adiabatic crossover time $\hat{t}$ using the overlap between the evolving wavefunction and that at criticality. This is in contrast to the previous definitions of locating $\hat{t}$.
- We have demonstrated that the number of the SF domains formed at $\hat{t}$ across the MI-SF quench obeys similar quenching law as that displayed by the vortex density N_v.
- We have examined the quench dynamics across the QPTs exhibited by the ultracold dipolar bosons in optical lattices. We have demonstrated the universal scaling relations across the stripe density wave to stripe supersolid phase transition by linearly varying the hopping amplitude.
- Further, for the dipolar bosons, we have examined the quench dynamics across the stripe supersolid to checkerboard supersolid phase transition. We have demonstrated the KZM like scaling relations for this first order quantum phase transition. The obtained scaling exponents obey the expected scaling relations.
- We have studied the BG-SF transition by using the percolation theory. We have demonstrated the divergence of the correlation length obtained using the methods of the percolation theory. The obtained scaling exponent quantifying the power-law divergence suggests that the BG-SF transition is in two-dimensional percolation universality class. We have also supplemented the location of the critical point of the phase transition by computing the superfluid stiffness.

1.4 Overview of the chapters

The overview of the chapters in the rest of the thesis is as follows.

- Chapter 2 describes the minimal theoretical model - BHM, and its quantum phases. We also illustrate the numerical methods that are used in this thesis to solve the BHM model and obtain the ground state quantum phases. These include the single-site Gutzwiller mean-field (SGMF) and the cluster Gutzwiller mean-field (CGMF) methods. Next we also present a novel algorithm that we have developed to count the clusters in a lattice and for their percolation studies.

- Chapter 3 is based on the equilibrium quantum phases of the BHM and the eBHM. We have discussed the parameter domains of the novel SS phase in the phase diagrams of eBHM with different strengths of the nearest neighbour interaction V. We have further demonstrated the enlargement in the domain of the SS phase in the presence of the artificial gauge fields. The phase diagrams are obtained using the SGMF and the CGMF methods.

- Chapter 4 discusses the quantum quench dynamics across the across certain QPTs of the BHM and the dipolar BHM models. We have derived the KZ scaling laws and have then obtained them in the quench dynamics. Specifically, we have obtained the KZ scaling laws across the MI-SF QPT, and have illustrated that the scaling relations among the obtained critical exponents. For the dipolar bosons, we have quenched across the density wave to supersolid transition, and have computed the KZ scaling laws. Furthermore, we have also quenched across the stripe to checkerboard supersolid structural phase transition and have discussed the universal scaling laws in the dynamics. This is a salient feature of the work as it demonstrates the KZM for the first-order QPT.

- Chapter 5 is based on the critical properties of the Bose-glass (BG) to SF QPT, using the percolation theory. We have discussed the disordered BHM and its quantum phases and then the divergence of the correlation length of the SF clusters across the BG-SF QPT. We have computed the critical exponent ν characterising the divergence and have shown that it belongs to the 2D percolation universality class. The percolation studies are performed using the novel domain counting method that we discuss in Chapter 2.

- Chapter 6 states the conclusions of the thesis and the future research directions that can be pursued.

Chapter 2

Theoretical and Numerical methods

Ultracold Bose condensed atoms trapped in optical lattices are novel engineered quantum systems used to explore the quantum many-body physics. These systems act as efficient quantum simulators due to the high level of controllability of the system parameters [144–146]. The BECs of dilute atomic gases are weakly interacting systems due to the low densities of the gases. The typical density of such gases used is five to six orders of magnitude lesser than the typical density of the surrounding air. A satisfactory description then of these dilute atomic gases is provided by the Gross-Pitaevskii (GP) equation [147, 148]. When such dilute Bose condensed atomic gases are trapped in optical lattices, it is possible to drive the system towards the strongly correlated regime. This is surprising given the low densities of the atomic gases. In these systems, the ratio of the kinetic energy to the interaction energy can be lowered as the itinerancy in a lattice potential is restricted. The prime examples of the strongly correlated quantum states displayed by ultracold atoms in optical lattices are the MI [17] and the FQH states [104, 149, 150]. For describing these quantum phases, the macroscopic wavefunction obtained from the GP equation is incorrect.

To correctly describe the strongly interacting domain of these quantum systems, the BHM is used. The BHM is a minimal model that describes the physics of interacting bosonic atoms in lattices [19] at $T = 0$ K. The kinetic energy counterpart in the BHM Hamiltonian is the hopping between the NN lattice sites. The interatomic interaction of the dilute gas is approximated by the pseudo contact potential, i.e. if the atoms are at the same lattice site. The ground state of this model exhibits two distinct quan-

tum phases, MI and SF. The theoretical studies complemented with the experimental demonstration of the quantum phase transition between MI and SF phase [17, 18] have boosted the studies on the equilibrium and non-equilibrium properties of the ultracold atoms in optical lattices. These systems have become a toolbox to investigate a wide variety of exotic quantum phases [145, 151–153].

In this chapter, we shall first discuss the physics of the BHM and the quantum phases exhibited. We shall demonstrate the Gutzwiller ansatz employed to obtain the ground state quantum phases. We shall then discuss the CGMF method that is an improvement over the SGMF method. After discussing these methodologies to obtain the equilibrium quantum phases, we shall present a novel cluster identification algorithm that we have developed for percolation analysis. We shall discuss the algorithm in detail, and also demonstrate its supremacy over the existing algorithms for percolation analysis.

2.1 Bose-Hubbard model

We begin our discussion by deriving the Hamiltonian for the BHM. A general two-body Hamiltonian of interacting bosonic neutral atoms in the grand canonical ensemble can be written as

$$\begin{aligned}\hat{H} &= \int \mathrm{d}\mathbf{r}\hat{\Psi}^{\dagger}(\mathbf{r})\left[-\frac{\hbar^2\nabla^2}{2m}+V^{\mathrm{ext}}(\mathbf{r})\right]\hat{\Psi}(\mathbf{r})-\mu\int \mathrm{d}\mathbf{r}\hat{\Psi}^{\dagger}(\mathbf{r})\hat{\Psi}(\mathbf{r}) \\ &+ \frac{1}{2}\int \mathrm{d}\mathbf{r}\mathrm{d}\mathbf{r}'\hat{\Psi}^{\dagger}(\mathbf{r})\hat{\Psi}^{\dagger}(\mathbf{r}')U_{\mathrm{int}}(\mathbf{r}-\mathbf{r}')\hat{\Psi}(\mathbf{r}')\hat{\Psi}(\mathbf{r}), \qquad (2.1)\end{aligned}$$

where $\hat{\Psi}(\mathbf{r})$ is the time independent bosonic field operator which creates an atom at the position $\mathbf{r}$. The confining potential $V^{\mathrm{ext}}(\mathbf{r})$ has the form of a sinusoidal lattice potential and the interatomic interaction is $U_{\mathrm{int}}(\mathbf{r}-\mathbf{r}')=\frac{4\pi\hbar^2 a_s}{m}\delta(\mathbf{r}-\mathbf{r}')$. Note that the interatomic interaction is a contact interaction potential. This is an assumption that is valid for dilute gases. The quantity a_s is the s-wave scattering length, and m is the atom's mass. Also, μ is the chemical potential that acts as a Lagrange multiplier to determine the mean number of atoms in the grand canonical ensemble. The above Hamiltonian can be equivalently written in terms of the Wannier basis functions. These are localized basis functions with a discrete symmetry of the lattice system. The field

operators in the continuous space can be expressed in terms of the Wannier states localized at lattice sites. For our analysis, we assume that the lattice potential is deep such that the relevant energy scales are smaller than the energy gap between the first and second bands. This is a reasonable assumption since the occupation of the higher bands can be neglected at low temperatures. That is, the dynamics of the system is frozen to the lowest Bloch band, and this is referred to as *lowest-band approximation*. Also, for the deep potentials, the *tight-binding limit* is applicable in which the Wannier states are localized at the lattice sites. The expansion of the field operators in terms of the Wannier functions of the lowest band is then

$$\hat{\Psi}(\mathbf{r}) = \sum_i w_{i,0}(\mathbf{r})\hat{b}_i, \tag{2.2}$$

where the subscript 0 of $w_{i,0}$ denotes the lowest band, and $\hat{b}_i$ corresponds to the annihilation operator for the i^{th} lattice site. Substituting Eq. (2.2) in Eq. (2.1) and using the tight-binding and the lowest-band approximation, we obtain

$$\hat{H}_{\text{BHM}} = -\sum_{\langle i,j\rangle} J_{ij}\hat{b}_i^\dagger\hat{b}_j + \frac{U}{2}\sum_i \hat{n}_i(\hat{n}_1 - 1) - \mu\sum_i \hat{n}_i, \tag{2.3}$$

where the $\hat{n}_i = \hat{b}_i^\dagger\hat{b}_i$ is the occupation number operator, the hopping strength is

$$J_{ij} = -\int \mathrm{d}\mathbf{r} w_{i,0}^*(\mathbf{r})\left[-\frac{\hbar^2\nabla^2}{2m} + V^{\text{ext}}(\mathbf{r})\right] w_{j,0}(\mathbf{r}), \tag{2.4}$$

and the strength of the onsite interaction is

$$U = \frac{4\pi\hbar^2 a_{\text{s}}}{m}\int \mathrm{d}\mathbf{r}|w_{i,0}(\mathbf{r})|^4. \tag{2.5}$$

In Eq. (2.3) $\langle\cdots\rangle$ is to denote the sum over NN lattice sites. The Hamiltonian in Eq. (2.3) is referred as the Bose-Hubbard model. Due to the tight-binding limit and the subsequent vanishing overlap of the Wannier functions of neighbouring sites, the tunneling term is restricted to the NN, and the interaction term is limited to the same site. The bosonic creation $\hat{b}_i^\dagger$ and annihilation $\hat{b}_i$ operators satisfy canonical commutation relations:

$$\begin{aligned}\left[\hat{b}_i, \hat{b}_j^\dagger\right] &= \delta_{i,j},\\ \left[\hat{b}_i^\dagger, \hat{b}_j^\dagger\right] &= \left[\hat{b}_i, \hat{b}_j\right] = 0.\end{aligned} \tag{2.6}$$

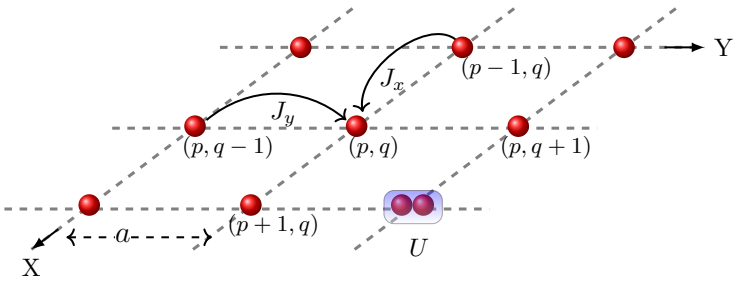

Figure 2.1: A schematic illustration of the NN hopping and onsite interaction terms in BHM for a 2D lattice.

In this thesis, we have considered a two-dimensional square optical lattice formed by interfering two pairs of counterpropagating laser beams along the x and y direction. The motion along the z direction is suppressed by the strong confinement, thereby obtaining a quasi-2D lattice. For a 2D square lattice, the site index $i \equiv (p, q)$ and $j \equiv (p \pm 1, q \pm 1)$ is its NN. If the system is homogeneous, then J_{ij} is invariant under the lattice translational operation. In that case, we drop the subscripts from the J_{ij}. A schematic to illustrate the hopping and interaction terms of the BHM is shown in Fig. 2.1.

2.2 Single-site Gutzwiller mean-field theory

The off-diagonal hopping terms in Eq. (2.3) are quadratic in operators of neighbouring sites. This prevents recasting the BHM Hamiltonian as a sum of single-site local Hamiltonians and sophisticated techniques like exact-diagonalization with respect to coupled basis states [154, 155] are required to obtain the ground state quantum phases. However one can use the mean-field technique to obtain the approximate ground states of the BHM. In the SGMF method, the bosonic annihilation and creation operators of a site (p, q) are decomposed as [156, 157]

$$\hat{b}_{p,q} = \phi_{p,q} + \delta\hat{b}_{p,q}, \tag{2.7a}$$

$$\hat{b}^{\dagger}_{p,q} = \phi^{*}_{p,q} + \delta\hat{b}^{\dagger}_{p,q} \tag{2.7b}$$

where, $\phi_{p,q} = \langle\hat{b}_{p,q}\rangle$, and $\phi^{*}_{p,q} = \langle\hat{b}^{\dagger}_{p,q}\rangle$ are the mean field and its complex conjugate, respectively. Here the expectation values are taken with respect to the ground state of

the system. When these decompositions are substituted in the hopping terms in the BHM Hamiltonian, we obtain the mean-field Hamiltonian as

$$\begin{aligned}\hat{H}_{\mathrm{MF}} &= \sum_{p,q}\Big\{ -J\Big[\Big(\hat{b}^{\dagger}_{p+1,q}\phi_{p,q}+\phi^{*}_{p+1,q}\hat{b}_{p,q}-\phi^{*}_{p+1,q}\phi_{p,q}\Big)\\ &\quad+\Big(\hat{b}^{\dagger}_{p,q+1}\phi_{p,q}+\phi^{*}_{p,q+1}\hat{b}_{p,q}-\phi^{*}_{p,q+1}\phi_{p,q}\Big)+\mathrm{H.c.}\Big]\\ &\quad+\frac{U}{2}\hat{n}_{p,q}(\hat{n}_{p,q}-1)-\mu\hat{n}_{p,q}\Big\}. \end{aligned} \tag{2.8}$$

In deriving the above mean-field Hamiltonian, the quadratic fluctuation operator terms are neglected. Note that the mean-field Hamiltonian is linear with respect to the bosonic creation and annihilation operators. The hopping between two neighbouring sites is via the mean-fields ϕ (or ϕ^{*}). As is evident from the Eq. (2.8), the total Hamiltonian is a sum of single site Hamiltonians

$$\hat{H}^{\mathrm{MF}}=\sum_{p,q}\hat{h}_{p,q}, \tag{2.9}$$

where the single-site mean-field Hamiltonian for site (p,q) is given as

$$\begin{aligned}\hat{h}_{p,q} &= -J\Big[\Big(\phi^{*}_{p+1,q}\hat{b}_{p,q}-\phi^{*}_{p+1,q}\phi_{p,q}+\phi^{*}_{p,q+1}\hat{b}_{p,q}-\phi^{*}_{p,q+1}\phi_{p,q}\Big)+\mathrm{H.c.}\Big]\\ &\quad+\frac{U}{2}\hat{n}_{p,q}(\hat{n}_{p,q}-1)-\mu_{p,q}\hat{n}_{p,q}. \end{aligned} \tag{2.10}$$

2.2.1 Gutzwiller ansatz

After reducing the BHM Hamiltonian to the mean-field Hamiltonian, we need to solve for the eigenstates and eigenenergies of the Hamiltonian. To obtain the ground state of the system, we use the Gutzwiller ansatz [84, 105, 150, 158]. In this, the eigenstate at each site is written as a linear combination of Fock states

$$|\psi\rangle_{p,q}=\sum_{n=0}^{N_{\mathrm{b}}-1}c_{n}^{(p,q)}\,|n\rangle_{p,q}\,, \tag{2.11}$$

where the $\{|n\rangle_{p,q}\}$ are occupation number states at (p,q), N_b is total number of local Fock states used in the computation, and $c_n^{(p,q)}$ is complex coefficient of the nth Fock state of the ground state $|\psi_{p,q}\rangle$. The total wavefunction of the system is a tensor product of site wavefunctions

$$|\Psi_{\mathrm{GW}}\rangle=\prod_{p,q}|\psi\rangle_{p,q} \tag{2.12}$$

The normalization of $|\Psi_{\mathrm{GW}}\rangle$ is ensured by the normalized wavefunction of every site

$$\langle\psi_{p,q}|\psi_{p,q}\rangle = \sum_{n=0}^{N_{\mathrm{b}}-1} |c_n^{(p,q)}|^2 = 1 \tag{2.13}$$

The Gutzwiller ansatz becomes exact for localized ground states obtained in the strongly interacting regime ($J \ll U$). The mean-field at the site (p, q) is

$$\phi_{p,q} = \langle\Psi_{\mathrm{GW}}|\hat{b}_{p,q}|\Psi_{\mathrm{GW}}\rangle = \sum_{n=1}^{N_{\mathrm{b}}-1} \sqrt{n} c_{n-1}^{(p,q)^*} c_n^{(p,q)}. \tag{2.14}$$

The occupancy at a lattice site (p, q) is the expectation of the number operator

$$\langle\hat{n}_{p,q}\rangle = \sum_{n=0}^{N_{\mathrm{b}}-1} n|c_n^{(p,q)})|^2. \tag{2.15}$$

For a given J/U and μ/U, the single-site Hamiltonian is diagonalized, and the eigenstate at each site is computed. The single-site Hamiltonian is expressed as a matrix using the Fock states basis $\{|n\rangle_{p,q}\}$. The matrix of the single-site Hamiltonian is of size $N_b \times N_b$, where the diagonal terms are constituted by the interaction and the chemical potential terms. Furthermore, the hopping terms constitute the off-diagonal terms in the local Hamiltonian. Due to the $\hat{b}_{p,q}$ and $\hat{b^\dagger_{p,q}}$ terms, the Fock basis $|n\rangle$ is coupled with $|n-1\rangle$ and $|n+1\rangle$. So the local Hamiltonian matrix is a tridiagonal matrix. We choose large N_b (=10) for our computations and have verified that the results do not change if it is further increased. We obtain the eigenstates and eigenvalues by iteratively diagonalizing the BHM Hamiltonian. For that, we consider a guess solution for the $|\Psi_{\mathrm{GW}}\rangle$ and compute the initial mean-field order parameter $\phi_{p,q}$. This guess solution is chosen based on the expected number and order parameter distribution of the quantum phase. In general, we choose $c_n^{(p,q)} = 1/\sqrt{N_b}$, for every Fock state basis for each site. This results in the uniform distribution of the $\phi_{p,q}$ and $\langle\hat{n}_{p,q}\rangle$ at the beginning of the self-consistent iteration procedure. For the parameters that result in checkerboard or striped density ordering, we consider the initial state that respects this ordering. Based on the initial $\phi_{p,q}$ obtained, the matrix is diagonalized and the new $\phi_{p,q}$ are computed using the Eq. (2.14). This procedure is repeated for all lattice sites and this constitutes a single iteration. We continue these iterations till we achieve the required convergence. The convergence criterion is based on the change in the value of $\phi = (K \times L)^{-1} \sum_{p,q} \phi_{p,q}$; we consider $\delta\phi = 10^{-12}$ as the convergence criterion.

To consider the thermodynamic limit corresponding to an infinite lattice, we employ the periodic boundary conditions (PBC) along and x and y-directions. That is, the computations are performed on the surface of a torus, as the square lattice with periodic boundary conditions gets mapped to a torus. Near the phase transition point, the convergence is poor, and thereby a large number of iterations are required.

The ground state phases of the BHM - MI and SF phases are distinguished based on the SF order parameter $\phi_{p,q}$. As defined previously, the SF order parameter $\phi_{p,q}$ is the expectation value of the annihilation operator $\hat{b}_{p,q}$. It is zero in the MI phase, and non-zero in the SF phase. This is because, in the MI phase of density m, the only non-zero Fock state that contributes is $c_m^{(p,q)}$. Therefore, integer commensurate m number of atoms are present at each site in the MI phase of density m. Thus, the number fluctuations are highly suppressed in the MI phase. On the other hand, in the SF phase, the system possesses the ODLRO. And more than one Fock state coefficient $c_n^{(p,q)}$ contributes to the wavefunction, owing to which the number fluctuations prevail in this phase. Also, unlike the MI phase, the system does not have integer commensurate occupancy at every site. The density is a real number in the SF phase. The phase transition between the MI-SF phase is marked $\phi \to 0$. The MI-SF phase boundary can be obtained analytically using the perturbation theory [84, 159].

2.3 Cluster Gutzwiller mean-field theory

The mean-field Hamiltonian in Eq. (2.8) describes the hopping in terms of the mean-fields $\phi_{p,q}$. Then the intersite correlations are not accounted accurately in the mean-field method. To incorporate the effects of these correlations, the CGMF method is used. In this method, the $K \times L$ lattice is divided into clusters of size $M \times N$. The key point is that the model is solved exactly inside a cluster, and the hopping between sites of neighbouring clusters is considered via the mean-fields. We can define a cluster Hamiltonian for every cluster, and the total Hamiltonian is then the sum of the cluster Hamiltonians. The Hamiltonian of a cluster is

$$\hat{H}_C = {\sum_{p,q\in C}}' \Big[-J\big(\hat{b}^\dagger_{p+1,q}\hat{b}_{p,q} + \hat{b}^\dagger_{p,q+1}\hat{b}_{p,q} + \text{H.c.}\big)\Big]$$

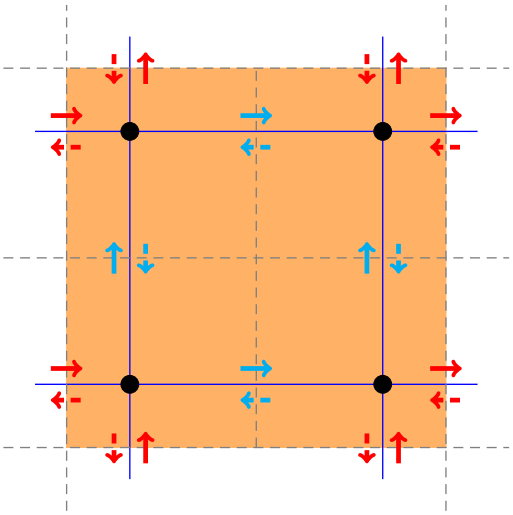

Figure 2.2: A cluster of size 2×2. The solid (dashed) blue arrows represent the exact hopping term (hermitian conjugate) within the cluster. The solid (dashed) red arrows represent the intercluster hopping term (hermitian conjugate).

$$+ \sum_{p,q\in\delta C} \Big[-J\big(\phi^*_{p+1,q}\hat{b}_{p,q} + \phi^*_{p,q+1}\hat{b}_{p,q} + \text{H.c.}\big)\Big]$$
$$+ \sum_{p,q\in C} \Big[\frac{U}{2}\hat{n}_{p,q}\left(\hat{n}_{p,q}-1\right) - \mu\hat{n}_{p,q}\Big] \tag{2.16}$$

where the prime over the summation means that the sum is over the bulk sites (p, q) such that their neighbouring sites $(p+1, q)$ and $(p, q+1)$ belong to the same cluster C. And $(p, q) \in \delta C$ indicates the sites on the boundary of the cluster. The order parameter $\phi_{p+1,q} = \langle\hat{b}_{p+1,q}\rangle$ is required for the intercluster hopping, where $(p+1, q) \notin C$. The intra-cluster exact hopping and intercluster hopping terms for a 2×2 cluster are shown in Fig. 2.2. The cluster Hamiltonian matrix can be constructed using the local Fock basis of the cluster $\{|n_0n_1n_2\ldots n_{m'}\rangle\}$, where $m' = M \times N - 1$. These are coupled basis states formed by the direct products of Fock states of the sites within the cluster. The total number of such basis states possible is $N_b^{M\times N}$. Thus the matrix dimension scales exponentially with the cluster size, thereby restraining the largest sizes of the cluster that can be considered. Certain constraints on the possible number of atoms in a cluster can be applied based on the expected quantum phases. For instance, for a 2×2 cluster and near the MI-SF phase boundary, the possible number of atoms in a cluster can be constrained to $n_0 - 2$ to $n_0 + 2$ with $n_0 = 4$ being the number of atoms in the MI phase in the four site cluster. These constraints reduce the Fock space

dimension considerably and the computations can be performed with a reduced time. With increasing cluster size, the intersite correlations are better accounted. The ground state of the cluster Hamiltonian is then given as

$$|\psi_\alpha^C\rangle = \sum_{n_0 n_1 \ldots n_{m'}} c^{(\alpha)}_{n_0 n_1 \ldots n_{m'}} |n_0 n_1 \ldots n_{m'}\rangle, \tag{2.17}$$

where the symbol α indicates the cluster index, and $c^{(\alpha)}_{n_0 n_1 \ldots n_{m'}}$ are the complex coefficients of the ground state $|\psi_\alpha^C\rangle$. Then, by employing Gutzwiller ansatz, the ground state of the entire lattice can be computed as

$$|\Psi_{\mathrm{GW}}\rangle = \prod_{\alpha=1}^{W} |\psi_\alpha^C\rangle = \prod_{\alpha=1}^{W} \sum_{n_0 n_1 \ldots n_{m'}} c^{(\alpha)}_{n_0 n_1 \ldots n_{m'}} |n_0 n_1 \ldots n_{m'}\rangle, \tag{2.18}$$

where $W = (K \times L) / (M \times N)$ are the number of clusters. The local superfluid order parameter and average occupancy at the (p, q) lattice site are computed as

$$\begin{aligned} \phi_{p,q} &= \langle \Psi_{\mathrm{GW}} | \hat{b}_{p,q} | \Psi_{\mathrm{GW}} \rangle, \\ n_{p,q} &= \langle \Psi_{\mathrm{GW}} | \hat{n}_{p,q} | \Psi_{\mathrm{GW}} \rangle. \end{aligned} \tag{2.19}$$

The computational steps performed in the CGMF method are similar to the SGMF method. An initial guess state $|\Psi_{\mathrm{GW}}\rangle$ is considered, and the order parameter $\phi_{p,q}$ is computed using this solution. The Hamiltonian matrix is then constructed and diagonalized to obtain the new $|\Psi_{\mathrm{GW}}\rangle$ and thereby the new $\phi_{p,q}$. We cover the entire lattice by this procedure, and one such sweep constitutes an iteration. These iterations are continued until the desired convergence in $\phi_{p,q}$ is obtained.

There are both qualitative and quantitative differences between the results obtained using the SGMF and CGMF theory. As an example of the former case, a strongly correlated Quantum Hall (QH) state is obtained only by using the CGMF method, as the approximated intersite correlations in SGMF fail to render the QH state. There are quantitative differences in terms of the phase boundaries when computed using SGMF and CGMF theory. For the BHM, the phase boundary between the MI-SF transition enhances as the sizes of the clusters are increased. In fact, the results converge toward the Quantum Monte Carlo (QMC) results as higher clusters are employed. A detailed comparison of the phase diagrams of the BHM obtained using clusters of different sizes can be found in [160].

Apart from the two mean-field techniques discussed to study the the MI-SF phase boundary of the BHM, there exists a variety of other methods to solve the BHM. The QMC simulations are considered as a benchmark in the numerical approaches, for instance, the QMC results in [161] for the 2D BHM. Some of the other approaches that are employed to study the MI-SF phase boundary are the bosonic dynamical mean-field theory [162], Bethe approximation [163], the perturbative analysis based on strong coupling expansion [164], the process chain approach [165], random phase approximation [166] etc.

2.4 Fine-grained percolation analysis

In this thesis, we shall use the methods of the percolation theory to discuss certain results in the upcoming chapters. Following that, in this section, we shall discuss a fine-grained computational method that we have developed to study the percolation analysis in 2D lattices. We shall first discuss the percolation theory in the following subsection.

2.4.1 Percolation theory

Percolation theory deals with the *clustering* of particles in a medium. A generic site-percolation problem consists of an infinite lattice with lattice sites labeled randomly with either of the two labels. Then, the sites are generically denoted as *occupied* with probability p and *unoccupied* with probability $1 - p$ [167, 168]. A collection of occupied sites that are connected through bonds is a cluster. The terminology of occupied and unoccupied sites is general, and depending on the application, a different set of binary labels may be used. For instance, to address the electrical conduction of a composite mixture of conducting and insulating materials, the sites would be labeled as belonging to either conducting or insulating constituents. And the percolation problem, in this case, would aim to answer what percentage of the composite mixture must be of conducting phase so that the whole material would be conducting. Alternatively, specific applications require the bond percolation wherein all sites are occupied, but the bonds between neighbouring sites are either present with probability p or absent

with probability $1 - p$. In this case, a cluster is a set of sites connected by bonds. For our purpose, we restrict to the site-percolation problem. The distribution and the size of these clusters are determined by the probability of a site being occupied. As the probability p exceeds a particular threshold value, the system undergoes a percolation phase transition. Then, there exists a spanning cluster that extends from one edge of the system to the opposite edge. This is a geometric phase transition, and the main goal is to compute the value of this critical probability so that system hosts a spanning cluster. Unfortunately, the analytical approaches to obtaining this critical probability and studying percolation are limited. However, numerical methods and techniques are used to understand the percolation properties of the system. As an example, for the site percolation on the square lattice, the numerical estimate is $p_c \approx 0.5927462$. The calculation of the exact percolation threshold for the site and bond percolation problem is an active research topic. For the list of these thresholds for various lattice geometries in different dimensions, see [167, 168]. The numerical techniques of the percolation theory involves identifying the clusters or the domains and then compute the percolation properties. Some of the well-known domain identification algorithms are the recursive neighbour search algorithm and the iterative algorithm. For the bond-percolation problem, the Newman-Ziff algorithm [169] is used.

In this section, we describe a fine-grained approach of cluster labeling and describe its application in the percolation analysis of 2D lattices. The discussed algorithm uses the linked-list data structure to describe a domain. A linked-list is a data type that consists of several linked nodes such that each node stores data and the address of the next node in the list. The linked-lists are used to define a path connecting the sites of a cluster. The advantage of the linked-lists is that domains can be labeled in a single scan. Since the path links sites, it is fine-grained, and we can employ it to analyse cluster properties. That is, different geometrical properties of the clusters, including the center of mass, the radius of gyration, and the correlation length can be computed by accessing the data stored in the linked-lists. Furthermore, the march along the boundary of a cluster can be performed using this method. Such a march has been shown very effective in determining the fractal dimensions. Therefore the algorithm constitutes a complete package for the cluster labeling and percolation properties on

lattice systems. We shall use this approach for detailed analysis of results encountered in the studies of optical lattices. The configurations obtained from these studies shall be examined using the tools from percolation theory. In this thesis, this approach is used to enumerate the domains formed in the quench dynamics across the QPTs as described in chapter 4, and also perform the percolation analysis across the Bose-glass to superfluid transition, described in chapter 5.

2.4.2 Mapping domain to a linked-list

We consider a 2D square lattice and assume each lattice site is labeled at random with either 0 or -1. Without the loss of generality, assume the label 0 is for the occupied sites. As mentioned earlier, the aim is to identify and label the domains of occupied sites, i.e of label 0. The lattice sites are denoted by (i, j), where i is the x- and j is the

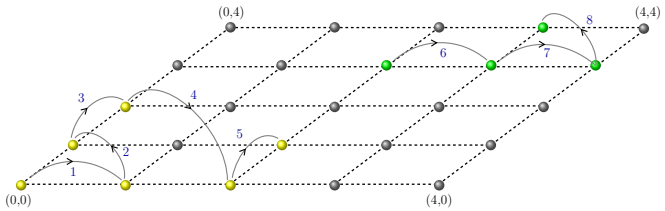

Figure 2.3: A schematic diagram to illustrate the paths defining a cluster in a 2D lattice. The arrows indicate the links between sites constituting a domain. Here distinct domains are identified with different colors representing domain labels; while the gray shaded lattice sites are of label -1. The numbers over the arrows represent the chronological sequence in linking the sites.

y-axis coordinate. The linked-list data structure [170] is used to identify a domain. As mentioned before, this data structure stores a data sequence in non-contiguous memory locations. Every element of the sequence is stored in the form of a node of the list. The node also has a reference or *address* of the location of the next element of the sequence. Thus, a node in the linked-list stores data and the address of the next node in the list. This continues till the last element of the sequence. In our work, every occupied site is mapped to the node of a unidirectional linked-list uniquely. This node (or the lattice site) is then linked to another node (another site) belonging to the same cluster. Thus each domain is represented by one linked-list and every site of a domain is a node of

the list. In this node, the data corresponding to the label being 0 and the address of the next node (meaning the next site) of the list is stored. In this way, we can traverse through all the lattice sites constituting a domain once the starting site is provided. Therefore the linked-list associated with a domain is a *path* that traverses through it. Such a path passes through each lattice site in the domain once. Thus by enumerating the number of unique paths, the number of domains and the domain identification can be done.

We now define certain variables to understand the algorithm. The two variables $x_{i,j}$ and $y_{i,j}$ are used to define the links in the linked-list. The variable $x_{i,j}$ ($y_{i,j}$) is the location along the x (y) direction of the next lattice site in the path. That is, the location of the next site in the path is stored in these variables. So assume that the sites $(1, 2)$ and $(1, 3)$ are a part of the same cluster, and are linked using the linked-list. To model this *linking*, the variable $x_{1,2} = 1$, and the variable $y_{1,2} = 3$.

These variables should have well defined values for the lattice sites at the beginning and intermediate nodes of a path for traversing. However, for the end node, there should not be any emergent connection from the end site. Thus, we assign a negative integer to these two variables of the end node. The lattice site indices, since labeled from 0, cannot be negative, and this is why negative integers are assigned for the end node. It is to be noted that the linked-list that we use is unidirectional. It is essential to define the location of the first lattice site or first node of the path. To store the location of the starting lattice site, we introduce two variables α^k and β^k for each path. Here α^k and β^k are the x and y locations of the first lattice site of the kth path, respectively. Similarly, we introduce γ^k and δ^k as the pair of variables defining the x and y lattice site corresponding to the last site of the path. We denote the total number of lattice sites in the kth domain by using the variable $\mathcal{N}^k$. So to summarise, the set of variables

$$\{\alpha^k, \beta^k, x^k_{i,j}, y^k_{i,j}, \gamma^k, \delta^k, \mathcal{N}^k\}, \tag{2.20}$$

are sufficient to define the kth path or the domain uniquely. The schematic diagram of typical paths defining clusters on a 2D square lattice are shown in Fig. 2.3.

2.4.3 Domain identification

Since we enumerate the domains of label 0, we check the label at each lattice site of a column, beginning from the left edge. Suppose that we are at a site (i, j) during the scan. If the label of this site is 0, then the counter variable k for domain label is incremented by 1, and the site is assigned the label k. That is, the site is identified as a member of the kth domain, and is included to the path of domain k. If the site is already identified as a member of a domain, then there is no change in the label. After site (i, j), the label of the right neighbour $(i + 1, j)$ site is scanned. If the label of this site is also 0, then, it is relabeled as k. This step makes the site $(i + 1, j)$ as a part of the same kth domain. The path for the domain also needs to be updated to include the site $(i + 1, j)$. After checking the right neighbour, the scan is continued to the lattice site $(i, j + 1)$. The details of linking the site in a path are given in the next section. The site (i, j) can also have label -1. In that case, the scan proceeds to $(i, j + 1)$, without checking the right neighbour. This process is repeated till the topmost lattice site of the column is reached. Then, the next column is scanned, and this process is continued till the entire system is covered. Therefore, we scan the lattice columnwise, from the left to the right column. In such a scanning process, two distinct cases arise. The first case corresponds to the left edge column, that is the first column that is scanned. In this column, the domains are not identified. The second case corresponds to the column in the bulk and the right edge of the system. We use the variable κ to record the number of domains identified.

2.4.4 Left edge column

We shall now discuss the algorithm when the leftmost column is scanned. At the beginning of the scan, the variable k is initialized to zero. It is incremented by one when a new domain is encountered. To demonstrate the algorithm, assume that the lattice site $(0, 3)$ is the first lattice site of label 0 along the column. During the scan, on reaching this lattice site, we increment k to 1 and relabel the lattice site $(0, 3)$ as 1. This is a newly identified domain. Also, the site $(0, 3)$ is the first node of the path for the domain with $k = 1$ and the last. Accordingly, we store the first or the starting site of the $k = 1$ path in the variables as $\alpha^1 = 0$ and $\beta^1 = 3$. At this step, since the

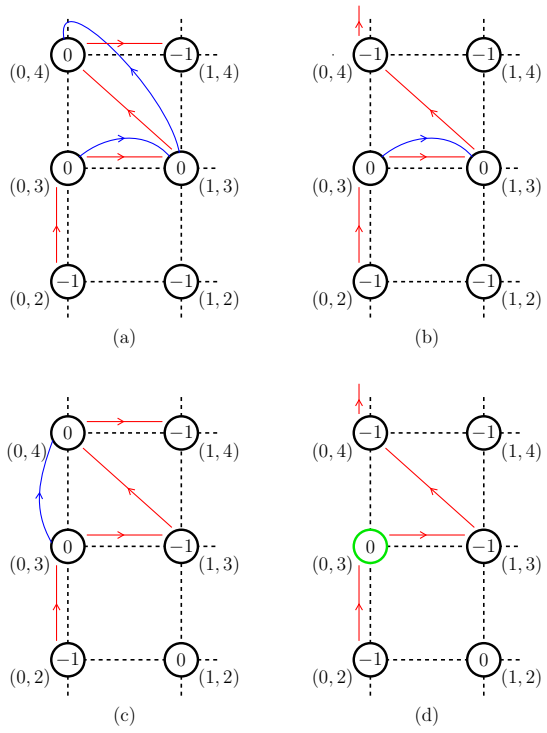

Figure 2.4: A schematic diagram to illustrate the possibilities arising in the scan along the lattice sites of the leftmost column. The red arrows indicate the scanning direction, and the blue arrows represent the inter-site links. The sites are represented by circles and the labels are shown within the circles. Panels (a)-(c) represent different cases of linking the site $(0, 3)$ with its right and/or upper neighbours. In panel (d), the possibility of a domain constituting a single site is shown.

path consists of a single site $(0, 3)$, the end node variables are updated as $\gamma^1 = 0$ and $\delta^1 = 3$. The counter for the number of nodes in the domain is updated as $\mathcal{N}^1 = 1$. Since this is the last node of a path, we set $x^1_{0,3} = -2$ and $y^1_{0,3} = -2$. The choice of -2 is arbitrary. It is a number that is not assigned to any of the variables and denotes no connection emerging from the site. As described previously, we then check the label of the right nearest neighbour lattice site $(1, 3)$. There are four possible outcomes.

Case A: If this lattice site has 0 label, then it is relabeled as 1. The end node of the path is updated to $(1, 3)$ by assigning $x^1_{1,3} = x^1_{0,3}$ and $y^1_{1,3} = y^1_{0,3}$, so that $x^1_{1,3} = -2$ and $y^1_{1,3} = -2$. The last node variables are updated as $\gamma^1 = 1$ and $\delta^1 = 3$. To update the path, the lattice site $(0, 3)$ is linked to $(1, 3)$ by setting $x^1_{0,3} = 1$ and $y^1_{0,3} = 3$. This means that the location of the next site in the list after $(0, 3)$ has x index as 1 and y

index as 3. We also update the member counter $\mathcal{N}^1 = 2$, as there are now two member sites in the $k = 1$ path. Then, we continue the scan to site $(0, 4)$ located above $(0, 3)$. If this too is 0, we extend the path to this lattice site by making this the end node with the assignment $x^1_{0,4} = x^1_{1,3}$ and $y^1_{0,4} = y^1_{1,3}$, and update the end node variables to $\gamma^1 = 0$ and $\delta^1 = 4$. The site $(0, 4)$ is linked to the lattice site $(1, 3)$ by redefining $x^1_{1,3} = 0$ and $y^1_{1,3} = 4$. It is important to note the sequence of appending the sites in the path. This possibility is schematically shown in Fig. 2.4(a).

Case B: In this case, the site $(1, 3)$ is labeled zero but not $(0, 4)$. This possibility is depicted schematically in Fig. 2.4(b). Here, the last step of linking the site $(0, 4)$ to the site $(1, 3)$ is not performed. That is, updations are the $x^1_{0,3} = 1$ and $y^1_{0,3} = 3$, $x^1_{1,3} = -2$ and $y^1_{1,3} = -2$, $\gamma^1 = 1$ and $\delta^1 = 3$ and $\mathcal{N}^1 = 2$. After this, the site $(0, 4)$ and its right and above neighbours are scanned.

Case C: The lattice site $(1, 3)$ is labeled -1, but $(0, 4)$ is labeled 0. This is similar to the Case A, but without the intermediate step of linking the lattice site $(1, 3)$ is not performed here. That is, the scan finds out the label on site $(1, 3)$ as -1 and hence does not link it with site $(0, 3)$. Instead the site $(0, 4)$ labeled 0 is linked with the site $(0, 3)$. This example therefore illustrates that the new site or node is always linked to the last identified site or node of the list. The situation is schematically shown in Fig. 2.4(c).

Case D: This is the last case and correspond the situation when both the lattice sites $(1, 3)$ and $(0, 4)$ are -1. Then, the $(0, 3)$ is an isolated domain as shown in Fig. 2.4(d), and here no updations are required.

2.4.5 Column in the bulk and right edge

We shall now discuss the steps to scan the remaining columns of the system. For concreteness, let us consider scanning of the ith column and jth row. Thus the lattice site to be scanned is (i, j). The steps of scanning the remaining columns of the system are the same. If the label on this site is -1, then this is a trivial case, as the site does not belong to any domain. In this case, the scan then continues to the next lattice site $(i, j + 1)$ in the column. However, if the label of the site (i, j) is not -1, then the scan has three possible outcomes. We shall discuss these cases now.

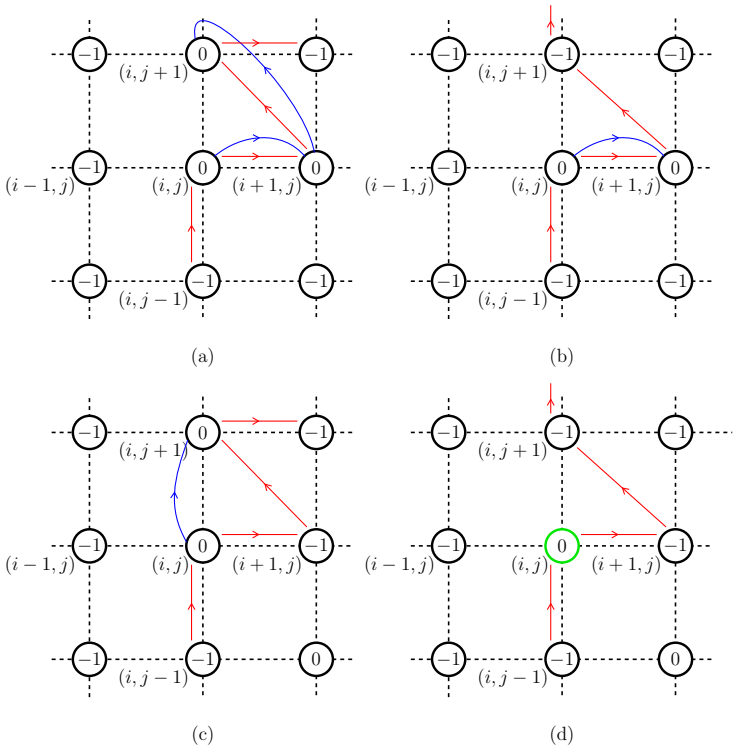

Figure 2.5: A schematic diagram to illustrate the formation of a new domain comprising of sites in bulk. The site (i, j), labeled 0, is the starting node of the path. The steps of scanning and linking the sites in the path are similar to that in Fig. 2.4

.

New domain

The first possible outcome is that the site (i, j) is labeled as 0. This is the case of the formation of a new domain, beginning from the site (i, j). The current value of κ and k is incremented by one. As done in the case of the left edge, we set $x^k_{i,j} = -2$ and $y^k_{i,j} = -2$ for the path, as the site (i, j) is identified as the last node. We also set $\mathcal{N}^k = 1$, indicating that the domain of label k has one member at this stage. The first (last) node variables of the path are set as $\alpha^k = i$ ($\gamma^k = i$) and $\beta^k = j$ ($\delta^k = j$). We, then, scan the lattice site $(i + 1, j)$ followed by $(i, j + 1)$. Similar to the case of the left edge column discussed earlier, we can have four possible outcomes. The only difference is, in each of the cases, the lattice site $(0, 3)$ is replaced by (i, j). These four cases are schematically shown in Fig. 2.5.

Old domain

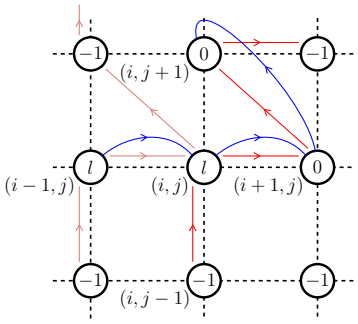

Figure 2.6: A schematic diagram to illustrate the case when the lattice site being scanned is already labeled with a domain label. As shown, the site (i, j) is labeled with label l. In this case, the right and upper neighbours are checked for label 0, and are added to the path of label l.

As a second possibility, consider that the label of the lattice site is a positive integer l, indicating that (i, j) is already identified as a member of the lth domain. Here, no modifications pertaining to the variables of (i, j) are done. However, we need to find out if the nearest neighbours of (i, j) are of label 0, in which case, they must be linked to the domain l. We check the label of the right nearest neighbour lattice site $(i+1, j)$. If the label is -1, then the scan continues to the upper nearest neighbour site $(i, j+1)$. On the other hand, if the site label of $(i + 1, j)$ is 0, then the lattice site belongs to the lth domain. So, we have to update the site label and path variables to include $(i + 1, j)$ as a part of this domain. For this, we label site $(i + 1, j)$ with l and link the end node of the lth path to the $(i + 1, j)$ by setting $x^l_{\gamma^l,\delta^l} = i + 1$ and $y^l_{\gamma^l,\delta^l} = j$. That is, the last added site of the lth path is linked to the site $(i + 1, j)$. It is important to note that this last node need not always be site (i, j). After these updations are done, the site $(i + 1, j)$ is made the end node by assigning $x^l_{i+1,j} = -2$ and $y^l_{i+1,j} = -2$, and then, update the end node variables to $\gamma^l = i + 1$ and $\delta^l = j$. The modifications associated with the addition of a node is complete by incrementing the node count $\mathcal{N}^l$ by one. The schematic diagram of this possibility is shown in the Fig. 2.6. For illustration, the path identified in the previous column scanning is shown in light red. Like the earlier cases, the next step is to consider the possibility of linking the upper neighbour lattice site

$(i, j+1)$ to domain l. We again follow same steps discussed in linking site $(i+1, j)$ to the domain l.

Therefore adding a site (i, j) as a new node to a path consists of three steps in general. The first step is site (i, j) is linked to the current end node of the path. The second step is where the site (i, j) is identified as the new end node of the path. The last step is where the end nodes and the member counter variables are updated. These steps are common to all the cases discussed.

Domain merging

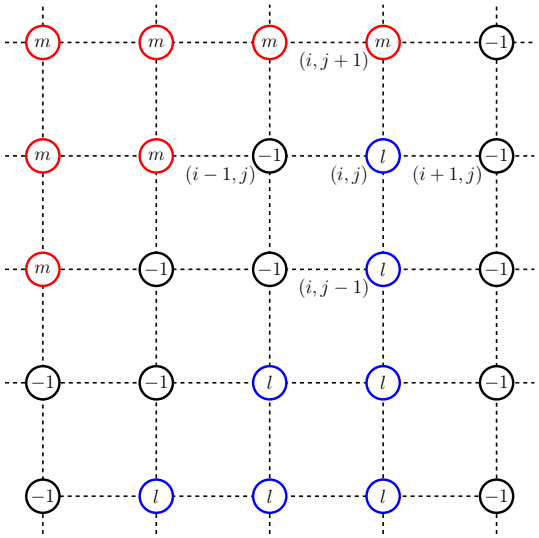

Figure 2.7: A schematic diagram to show the possibility of domain merging. The neighbouring sites (i, j) and $(i, j+1)$ obtain different labels during the scan. In this case, the two domains need to be merged, and a single label is to be retained.

If the two neighbouring sites are assigned two different domain labels, then these two domains need to be merged, and only one label must be retained. In the proposed algorithm, the merging of two domains occurs when labels of neighbouring sites (i, j) and $(i, j+1)$ in a column are two distinct labels. For example, consider the labels of these sites are l and m, respectively, and assume $l < m$. A representative case of such a situation is shown in Fig. 2.7. Following the Fig. 2.7, it is clear that only one domain label needs to be retained, as the sites form one single domain. Following the conventions adopted, the domain variables of the two are $\{\alpha^l, \beta^l, x^l_{i,j}, y^l_{i,j}, \gamma^l, \delta^l, \mathcal{N}^l\}$

and $\{\alpha^m, \beta^m, x^m_{i,j}, y^m_{i,j}, \gamma^m, \delta^m, \mathcal{N}^m\}$. The first step in merging the two domains is to link the two corresponding paths and consolidate the two into a single one. For doing this, the last node of the lth domain is linked to the first node of the mth node, thereby *connecting* the two paths. This connection is done by setting $x^l_{\gamma^l,\delta^l} = \alpha^m$ and $y^l_{\gamma^l,\delta^l} = \beta^m$. We tag the merged domain with the variables corresponding to the one with the lower label, which in this case is l. The merger is complete by updating the last node variables as $\gamma^l = \gamma^m$ and $\delta^l = \delta^m$, and the total number of lattice sites in the domain $\mathcal{N}^l = \mathcal{N}^l + \mathcal{N}^m$. As the last step, the mth domain is effectively nullified by setting $\mathcal{N}^m = 0$.

We shall now see an example for illustrating the working of our algorithm. In Table 2.1, a configuration for 2D lattice with sites labeled 0 and -1 randomly is shown.

-1	-1	-1	-1	-1	$\mathbf{0}$	$\mathbf{0}$	$\mathbf{0}$	-1	$\mathbf{0}$
-1	-1	$\mathbf{0}$	$\mathbf{0}$	$\mathbf{0}$	-1	-1	-1	$\mathbf{0}$	-1
-1	-1	-1	-1	-1	$\mathbf{0}$	-1	$\mathbf{0}$	$\mathbf{0}$	-1
-1	$\mathbf{0}$	-1	-1	$\mathbf{0}$	$\mathbf{0}$	-1	$\mathbf{0}$	-1	-1
-1	$\mathbf{0}$	$\mathbf{0}$	$\mathbf{0}$	-1	$\mathbf{0}$	$\mathbf{0}$	$\mathbf{0}$	-1	$\mathbf{0}$
$\mathbf{0}$	-1	$\mathbf{0}$	$\mathbf{0}$	-1	$\mathbf{0}$	$\mathbf{0}$	-1	$\mathbf{0}$	-1
-1	$\mathbf{0}$	$\mathbf{0}$	-1	-1	-1	$\mathbf{0}$	-1	$\mathbf{0}$	-1
$\mathbf{0}$	-1	$\mathbf{0}$	$\mathbf{0}$	-1	-1	-1	$\mathbf{0}$	-1	$\mathbf{0}$
$\mathbf{0}$	-1	$\mathbf{0}$	$\mathbf{0}$	-1	$\mathbf{0}$	-1	$\mathbf{0}$	-1	-1
-1	$\mathbf{0}$	-1	-1	-1	$\mathbf{0}$	$\mathbf{0}$	-1	$\mathbf{0}$	$\mathbf{0}$

Table 2.1: A random 2D configuration with sites labeled by binary values 0 and -1.

The identified domains are as shown in Table 2.2.

To summarize the developed algorithm, we present the flowchart in Fig. 2.8.

-1	-1	-1	-1	-1	**7**	**7**	**7**	-1	**9**
-1	-1	**5**	**5**	**5**	-1	-1	-1	**6**	-1
-1	-1	-1	-1	-1	**6**	-1	**6**	**6**	-1
-1	**4**	-1	-1	**6**	**6**	-1	**6**	-1	-1
-1	**4**	**4**	**4**	-1	**6**	**6**	**6**	-1	**11**
2	-1	**4**	**4**	-1	**6**	**6**	-1	**10**	-1
-1	**4**	**4**	-1	-1	-1	**6**	-1	**10**	-1
1	-1	**4**	**4**	-1	-1	-1	**8**	-1	**1**
1	-1	**4**	**4**	-1	**7**	-1	**8**	-1	-1
-1	**3**	-1	-1	-1	**7**	**7**	-1	**9**	**9**

Table 2.2: Configuration of the identified domains.

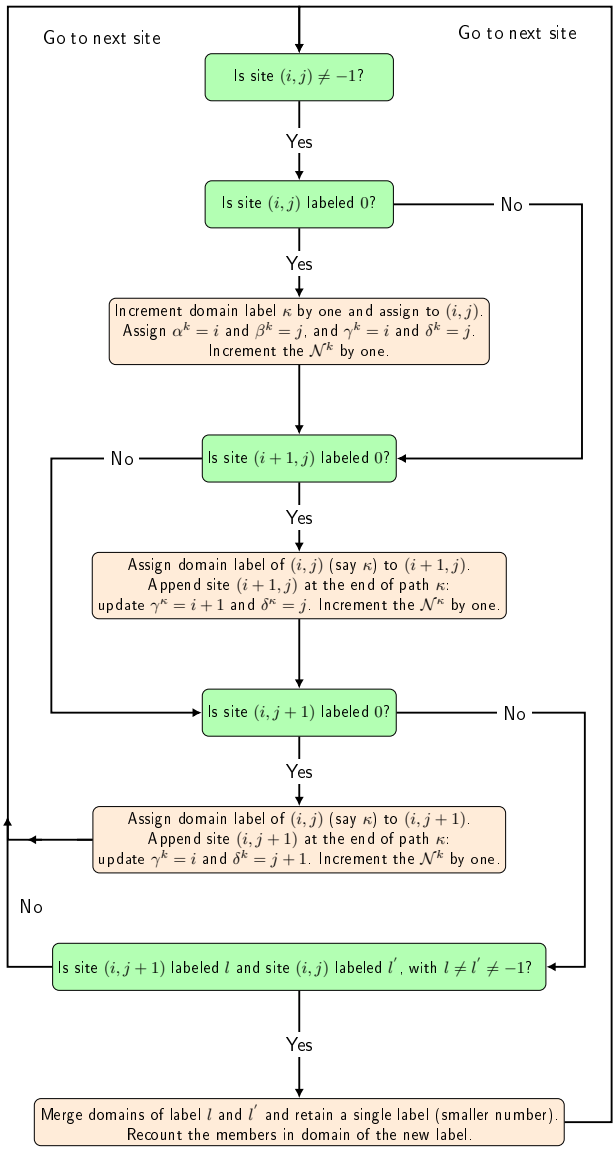

Figure 2.8: Flowchart of the developed algorithm.

As is evident from the flowchart, the label at site (i, j) being either 0 or a positive integer l is of interest. If it is labeled 0, then it is assigned a new domain label, and its right and upper nearest neighbours are scanned for their labels. If the site (i, j) has label l, then its right and upper neighbours are checked for their labels. In all the cases, the newly identified site of a cluster is appended, or "connected" to the last identified site of that cluster. Due to the way we scan the lattice, the merging of the domains can only occur when the (i, j) and $(i, j + 1)$ sites have different, non-zero domain labels.

2.4.6 Charting the boundary

The method introduced in the previous sections enables domain identification. Here we demonstrate the steps to map the boundary or the outer edge of a domain. In this context, it is crucial to note that a simple scan of the occupied site which possesses unoccupied sites as NN is incorrect in identifying the boundary of a domain. This is because a domain may contain a hole, and therefore the outer sites of a hole shall also qualify as a boundary of the domain. Hence it is essential to have a set or rules or an algorithm to chart out the boundary of a domain such that it excludes the internal boundaries associated with voids within the domains. This process is referred as the hull generating algorithm in the context of percolation theory [171, 172]. Determining the boundary is essential to investigate the properties of the domains and apply the methods rooted in the percolation theory.

In our method, to identify the boundary, we shall *march* along it in the clockwise direction, one bond at a time. A starting site (x_s, y_s) on the boundary must be identified to initiate this march. This is a very crucial step for the method outlined here. This starting site is identified as the leftmost site along one of the rows of a domain. Then the march is initiated after identifying the direction of the hop along the boundary to reach (x_s, y_s). We refer to this as the *prior hop*.

Identifying the prior hop

The starting point (x_s, y_s), as mentioned earlier, is the leftmost site of the domain along a row. Let the domain be labeled with m. Hence, there are only two possibilities of the prior hop through which it can reach the site. First, the prior hop in the upward

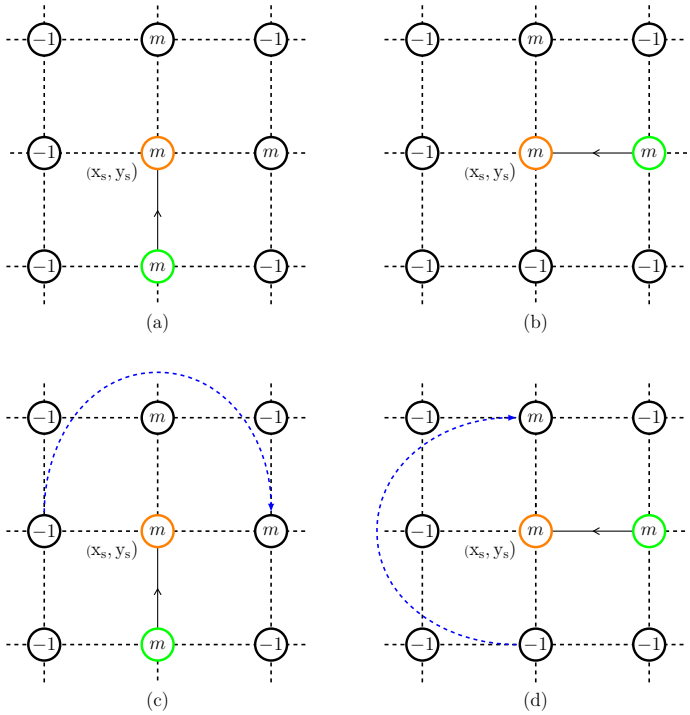

Figure 2.9: A schematic diagram to illustrate the prior hop and the clockwise scanning for the boundary *march*. The march is started from the leftmost site (x_s, y_s) as highlighted by the peach color. The black arrow represents the prior hop to reach the site (x_s, y_s). As illustrated in the text, this prior hop can be either in the upward direction (case (a)) or leftward direction (case (b)). In (c) and (d), the blue dashed arrow indicates the scanning of the neighbours of (x_s, y_s) in a clockwise manner with respect to the orientation of the prior hop. The neighbour of label m encountered in this clockwise scan then becomes the next site on the boundary.

direction to reach the site (x_s, y_s). This possibility is shown in Fig. 2.9 (a). The second possible prior hop is the leftward direction, as shown in Fig. 2.9 (b). Thus, it is sufficient to check the label at the two lattice sites (x_{s+1}, y_s) and (x_s, y_{s-1}). The one with the label m defines the originating site of the prior hop. After identifying the starting site (x_s, y_s) and the prior hop direction, the march along the boundary proceeds. The determination of the next hop requires the identification of the previous hop. This information is thus checked for every marching step in our method.

Clockwise scan

After locating the starting site, we need to identify the next site on the boundary. Thus we scan the other three nearest neighbours of (x_s, y_s) excluding the neighbour from which the prior hop originates. To do this systematically, the scanning is done in the clockwise direction with respect to the orientation of the prior hop. This is schematically shown in Fig. 2.9 (c) where the blue dashed arrow represents the sequence of scanning the neighbours of (x_s, y_s), in a clockwise manner with respect to the upward prior hopping direction. Thus, for this case, the first NN to be scanned is the left NN $(x_s - 1, y_s)$, followed by the upward NN $(x_s, y_s + 1)$, and then last the rightward NN $(x_s + 1, y_s)$. At any step of this scan, if a NN with label m is obtained, that is the next site on the boundary. For the case in Fig. 2.9 (a), the next site on the boundary is $(x_s, y_s + 1)$. Similarly, in Fig. 2.9 (d), the clockwise scan with respect to the leftward prior hopping orientation is shown. Let this next site on the boundary be identified as $(x_{s'}, y_{s'})$. Then the bond connecting the two sites (x_s, y_s) and $(x_{s'}, y_{s'})$ defines the orientation of the prior hop to scan for the next lattice site on the boundary after $(x_{s'}, y_{s'})$. It may happen that all the three neighbours of (x_s, y_s) have label -1. Then the march proceeds by retracing along the prior hop, and the origin of the prior hop is identified as the lattice site (x'_s, y'_s). This process of scanning is repeated till we return to the starting site (x_s, y_s), whereby the domain's boundary is completed.

We show the path along the boundary of a cluster in Fig. 2.10. The starting site (x_s, y_s), highlighted in green color, is the left most site of the bottom row. The prior hop to reach (x_s, y_s) is leftward in this case as shown by a gray arrow. After identifying the starting site and the prior hop, the scanning of nearest neighbours proceeds to

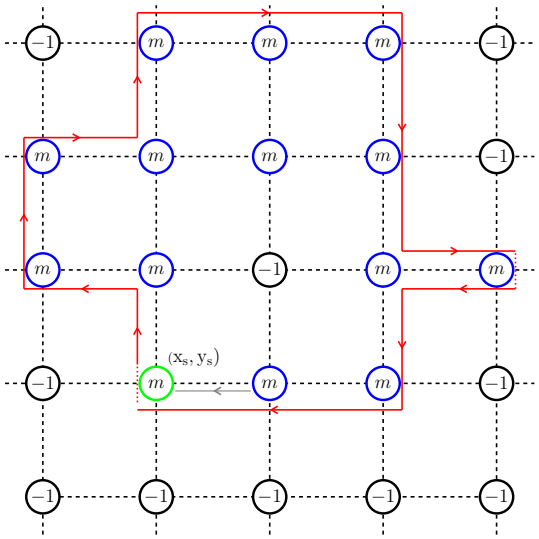

Figure 2.10: A schematic illustration of the march along the boundary of a cluster of label m. The leftmost site (x_s, y_s) in the bottom row is the starting site of the march. The prior hop along the boundary to reach (x_s, y_s) is the site (x_{s+1}, y_s), thereby this is leftward prior hop. This is shown by the gray colored arrow. The red arrows denote the directionality of the boundary march of the cluster shown in the figure.

identify the next site on the boundary. For the case illustrated in Fig. 2.10, this next site is upward NN of the starting site (x_s, y_s). As explained, the march is completed when we return to the initial starting site (x_s, y_s). Therefore an essential prerequisite for the boundary march is in the identification of the starting site and the prior hop.

2.5 Comparison of the algorithm with known methods

There are several well-known algorithms for domain identification in the percolation analysis. In this section, we shall present our algorithm's advantages and limitations over standard algorithms like the Hoshen-Kopelman (HK) and the recursive neighbour search algorithm. The comparisons are based on the computational efficiency and the execution time. We first discuss the comparison with the HK algorithm.

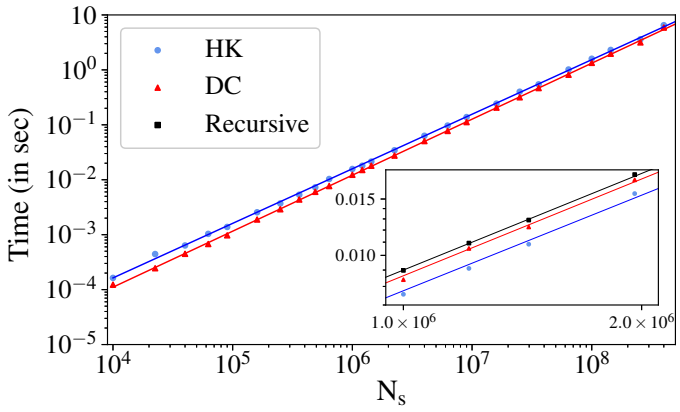

Figure 2.11: The plot of the execution time for the HK (solid blue circles), the presented domain counting (DC) (solid red triangles) and recursive neighbour search algorithms (solid black squares in the inset) for different lattice sizes N_s. The main panel includes the time required for the first scan and the post-processing steps for the HK and the DC algorithms. A marginal gain in the execution time for the DC algorithm as compared to the HK algorithm can be noticed. Further, the inset illustrates the time required for the first scan by the three mentioned algorithms. The recursive neighbour search algorithm takes the maximum time compared to the DC and the HK algorithm for the first scan. The solid blue (red, black) lines are the least square fit for the HK (DC, recursive neighbour search) algorithms. The data points are obtained by averaging over 40 pseudo-random configurations.

2.5.1 Hoshen-Kopelman algorithm

The HK algorithm is a multiple cluster labeling algorithm widely used in clustering and percolation studies [173]. In this algorithm, lattice sites are checked if they are occupied and are then relabeled with a cluster label. This cluster label is based on the labels of the scanned neighbouring sites. A new cluster label is assigned if there are no neighbouring occupied sites. While if there is one neighbouring occupied site, then the cluster label of the neighbouring site is assigned to the current site. When there are more than one occupied neighbours having different cluster labels, then the lowest cluster label is assigned. This results in cases when the cluster gets labeled with multiple cluster labels. Then, an equivalence class of these multiple labels is created to maintain a record that these labels denote the same cluster. There are now several variations of the HK [174–178] including a proposal to use a linked-list to group the clusters

belonging to the same domain [179]. The application of the percolation analysis and the HK algorithm are in diverse fields like - food and chemical engineering [180, 181], ecology [182] and biology [183]. The HK algorithm constructs a coarse-grained linking between the cluster labels. On the contrary, our approach is fine-grained as the linking involves sites. This fine-grained approach is efficient for the cluster characterization studies of the percolation theory. In the HK framework, we need to scan the lattice every time for the percolation studies. However, in our approach, we can traverse through the linked-lists to compute the cluster properties without any lattice scan.

Furthermore, an additional scan after the first lattice scan is required in the HK algorithm to label the clusters with a unique cluster label. This post-processing step in the HK algorithm makes it slower than the DC algorithm, as shown in Fig. 2.11 main panel. The details on computations in Fig. 2.11 and the discussion on the inset plot is given in Appendix A. In summary, the DC algorithm is computationally efficient due to the fine-grained linking and is also faster than the HK algorithm. These are the key advantages of the DC algorithm in comparison with the HK algorithm.

The memory required in the DC algorithm is about three times larger than the memory required by the HK algorithm. This is expected as the DC method needs memory to construct the linked lists. However, this extra memory requirement is not a significant limitation given the recent advances in memory hardware.

2.5.2 Recursive neighbour search algorithm

The recursive neighbour search algorithm involves searching and labeling the neighbours of the occupied sites recursively. If an occupied site is obtained during the scan, then it is relabeled by the current label counter. Then, the neighbours of this site are scanned in search of occupied sites. If an occupied neighbouring site is obtained, it is relabeled, and the function to search the neighbours of this site is called. This process is continued recursively till all the sites of the cluster are identified. The crucial advantage of this approach is that only the required cluster can be identified without needing to identify other clusters.

There are no domain mergers in the recursion method, and hence there is no post-

processing of the labels in this method. Therefore, we have compared the recursive approach only in the inset where the execution times shown do not involve post-processing. The black solid line in Fig. 2.11 is the least square fit to the data of the recursive algorithm. The plots illustrate that the recursive neighbour search is slower than the DC and the HK algorithm, which is a disadvantage of this method. On the contrary, for the DC algorithm, the first scan over the lattice which labels the clusters and constructs the linked-lists is faster. Hence within a lesser time, the more efficient DC algorithm can be executed. The recursion method is a simplistic domain identification approach and it does not links the sites of the cluster. Also, there are studies [184] that demonstrate that the number of the recursive function calls becomes very large for larger system sizes, limiting the stack memory required and making it inefficient. The DC algorithm is not based on recursion; hence, this limitation does not apply. Also, as the linked-lists are constructed, it is efficient to compute the geometrical properties of the clusters. However, in the recursive approach, each calculation requires scanning over the lattice. In this context, complementing the recursive approach with the fine-grained linking using linked-lists would be efficient.

2.6 Summary of the chapter

To summarize, we have discussed the BHM Hamiltonian for the ultracold bosonic atoms in two-dimensional optical lattices. We have studied the methods that we employ in this thesis to obtain the ground states of the BHM and its variations. The first method is the single-site Gutzwiller mean-field method which considers the NN hopping with the mean-field ϕ. The second method is the cluster Gutzwiller mean-field method, which encapsulates better correlations. We then discuss a novel method that we have developed to perform the studies related to the percolation in 2D lattices. This algorithm enumerates the domains of a particular label on the lattice and stores the locations of the sites constituting a cluster. We have discussed the comparison of the presented algorithm with the existing standard algorithms like the HK algorithm and the recursive neighbour search algorithm. We shall demonstrate the utility of this algorithm in the upcoming chapters in this thesis, whereby we shall apply it to the quench

dynamics studies and the percolation of the clusters in disordered optical lattice potentials.

Chapter 3

Equilibrium phases of eBHM

In the previous chapter, we have discussed the equilibrium quantum phases of the BHM and the theoretical methods employed to obtain the ground states. As discussed previously, BHM is a minimal model to describe the physics of neutral bosonic atoms in lattices. This model encapsulates the competition between the hopping and the onsite interaction, and depending on the relative strength between these two, the ground state is either in MI or SF phase. Owing to the low densities of these cold atomic gases, the interaction among the atoms are restricted to the same site. However, there are studies that dismiss these simplifications and approximations and show the presence of exotic, novel quantum phases. For instance, the density induced tunneling, the pair tunneling and the nearest neighbour interactions [185–191] are some of the additional terms that are obtained by going beyond the approximations. An extensive review of these non-standard BHMs can be found in [153]. Also, with the advent of the dipolar BECs, the offsite interactions are introduced in the BHM, as the onsite interaction is not sufficient to describe the long-range dipolar interaction between the dipolar atoms. In this chapter, we shall discuss the effect of these offsite interaction terms in the BHM. As the dipolar interaction term falls as cubic with respect to the separation, often it is restricted to the nearest neighbours (NN). And the anisotropy is excluded by assuming the dipoles to be perpendicular to the lattice plane. Then this minimal model with the NN interaction is called as extended BHM (eBHM). This model exhibits structured quantum phases which have off-site density-density correlations, which are otherwise not possible with the onsite interaction. Moreover, the model also exhibits the novel

supersolid (SS) phase. This makes the study of this model more important as the search for supersolidity in quantum materials is an active topic of research.

In this chapter, we shall investigate the QPTs exhibited by the eBHM in 2D square optical lattice. We shall discuss the parameter regime of the SS phase in the phase diagram, and shall study the robustness of this phase against the quantum fluctuations incorporated by using the clusters in CGMF. We shall begin by discussing the eBHM model Hamiltonian, and the characterization of the quantum phases. We shall then present the results pertaining to the phase diagrams of eBHM obtained using the SGMF and CGMF theory. In particular, we shall present the effect of considering larger clusters on the DW to SS and MI to SF phase transition. We shall also demonstrate the effect of the artificial gauge on the quantum phases in the eBHM. In particular, the localizing effect of the artificial gauge field leads to enlarged parameter domains of the SS phase in the phase diagrams. We now begin by describing the eBHM model Hamiltonian.

3.1 Extended Bose-Hubbard model

The Hamiltonian for the eBHM is defined as follows

$$\begin{aligned}\hat{H}_{\text{eBHM}} &= -\sum_{p,q} J\left(\hat{b}^{\dagger}_{p+1,q}\hat{b}_{p,q} + \hat{b}^{\dagger}_{p,q+1}\hat{b}_{p,q} + \text{H.c.}\right) \\ &+ \sum_{p,q} \hat{n}_{p,q}\left[(\epsilon_{p,q} - \mu) + \frac{U}{2}(\hat{n}_{p,q} - 1)\right] \\ &+ \sum_{p,q} V_{p,q}\,\hat{n}_{p,q}\,(\hat{n}_{p+1,q} + \hat{n}_{p,q+1}) \end{aligned} \tag{3.1}$$

where $p(q)$ is the lattice site index along $x(y)$ direction. Similar to the BHM Hamiltonian given in Eq. 2.3, J is the NN hopping strength, U is the strength of the onsite interaction, and the last term is the NN interaction term with V being its strength. The model Hamiltonian is similar to the BHM Hamiltonian, and has the extra NN interaction term with V as the interaction strength. This model has been experimentally realized with magnetic dipolar atoms in 3D optical lattices [26]. The offsite density-density interaction, together with the hopping and the onsite interaction leads to exotic quantum phases that will be described in the next subsection.

3.1.1 Characterization of phases

There are several combinations of the order parameters to identify the quantum phases exhibited by the eBHM. The NN interaction leads to the structured quantum phases like the DW and the SS phase. The DW phase is an incompressible phase like the MI phase, however, has a checkerboard order in the density distribution. That is, this phase has a periodic density modulation along both the x and y direction or has a long-range crystalline (solid) order (LRO). This phase has zero ϕ and integer occupancy for each lattice site. Notationally, DW (n_A, n_B) denotes that n_A atoms in sublattice A and n_B in sublattice B, with the average occupancy $(n_A + n_B)/2$. Such a density distribution leads to lesser NN interaction cost than the uniform density distribution. The SS phase is compressible phase, and has non-zero ϕ. Similar to the DW phase, this phase also has an underlying checkerboard density distribution. However, the densities at the two sublattices are real numbers. This periodic modulation of the density and the non-zero ϕ implies that the SS phase has both the LRO and the ODLRO, counter-intuitive to the common expectations. We use the SF order parameter to identity the incompressible-to-compressible phase boundary (MI-SF, DW-SS). The SS-SF phase transition involves density redistribution, as it is a transition from the ordered to uniform phase. To identify the SS-SF phase boundary, we use the static structure factor $S(\pi, \pi)$. It is defined as the Fourier transform of the density-density correlations, and it reveals the underlying periodicity in the density distribution -

$$S(\mathbf{k}) = \frac{1}{N^2} \sum_{i,j} e^{i\mathbf{k}.(\mathbf{r}_i - \mathbf{r}_j)} \langle \hat{n}_i \hat{n}_j \rangle, \tag{3.2}$$

where $\mathbf{k} = k_x\hat{i} + k_y\hat{j}$ is the two-dimensional reciprocal lattice vector, and N is the total number of bosons in the lattice. In the checkerboard ordered SS phase, $S(\pi, \pi)$ is non-zero, while in the uniform density SF phase, it is zero. Thus it serves as an order parameter to distinguish between the SS and the SF phase. Table 3.1 summarizes the classification of all the phases discussed in the present work.

Quantum phases	$n_{p,q}$	$\phi_{p,q}$	$S(\pi,\pi)$	κ
Mott insulator (MI)	integer	0	0	0
Density wave (DW)	integer	0	$\neq 0$ (integer)	0
Supersolid (SS)	real	$\neq 0$	$\neq 0$ (real)	$\neq 0$
Superfluid (SF)	real	$\neq 0$	0	$\neq 0$

Table 3.1: Classification of quantum phases of the eBHM at zero temperature.

3.2 Phase diagram of eBHM

In this section, we shall discuss the phase diagrams of the eBHM obtained using the SGMF and the 2×2 CGMF theory. As described earlier, the introduction of the NN interaction leads to the emergence of DW and SS phases in the phase diagram. We shall first examine the phase diagram for the homogeneous systems, that is with no artificial gauge field. We, then, study the impact of artificial gauge field on the phase diagram. We also study the effect of the quantum fluctuations by performing computations with varying cluster sizes. We note the change in the critical point of the DW-SS and MI-SF transition with different cluster sizes.

3.2.1 Homogeneous case

In Fig. 3.1, the phase diagrams of the eBHM for different values of V/U, in the $J/U - \mu/U$ plane using the SGMF theory. The incompressible MI and DW phases are denoted by the sublattice occupancies (n_A, n_B). When $zV/U < 1$, the ground state for low J/U alternates between the MI and DW phases - see Fig. 3.1 (a). And, the SS phase is seen to envelope the DW phase lobes. Thus, on increasing the J/U, the superfluidity in the checkerboard DW solid is induced, thereby leading to the simultaneous occurrence of the solid and superfluid behavior. For $J/U = 0$ (atomic limit), the width of the DW lobes along the is zV, while that of the Mott lobes is U [192]. This can be analysed by comparing the energies of the DW and MI lobes as a function of μ. At high J/U, the system is in SF phase.

In the opposite limit $zV/U > 1$, the DW phase is the only incompressible phase in the phase diagram. Based on the energy analysis, it can be shown that at critical

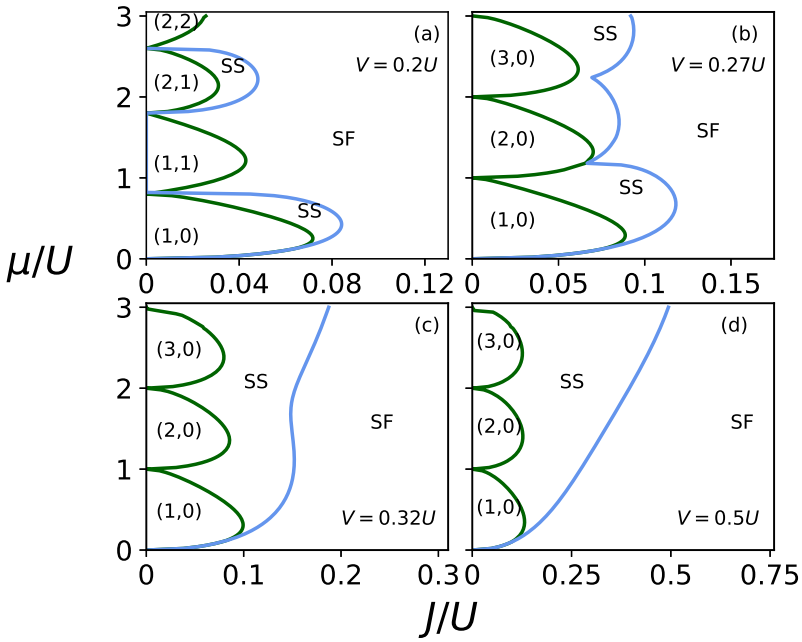

Figure 3.1: The phase diagrams of the eBHM with uniform hopping amplitude ($J_x = J_y = J$) for $V/U = 0.2, 0.27, 0.32$, and 0.5 (a-d). The solid green line indicates the incompressible to compressible MI-SF, DW-SF and DW-SS phase boundaries. The solid blue line represents the SS-SF phase boundary. Here, the DW and MI phases are indicated by their sublattice occupancies (n_A, n_B).

$V_c = U/z$, the MI lobes are transformed in the DW phase. Formally, the DW $(2n, 0)$ phase becomes degenerate with the MI (n, n) phase [192]. Another notable change is that the width of the DW lobes in the atomic limit is U in this strong interaction regime. Also, the SS phase occupies a relatively larger region in the phase diagram. As V is increased, the critical J_c/U for the DW-SS transition also increases. We also note that for $zV \gtrsim 1.5U$, the SS-SF phase boundary appears as a linear function of the J, as discernible from Fig. 3.1(d). The phase boundaries obtained numerically are in good agreement with the analytical site-decoupled mean-field theory given in [193].

To consider the effect of the quantum fluctuations on the ground state phase diagrams, we perform the computations using 2×2 cluster, and the obtained phase diagrams are shown in Fig. 3.2. The qualitative features of the phase diagram are similar to the ones based on the SGMF, however, there are certain quantitative differences based on the phase boundaries. First, compared to the SGMF results, the MI lobes are enhanced with 2×2 cluster. Such an increase in the MI phase lobe in the BHM

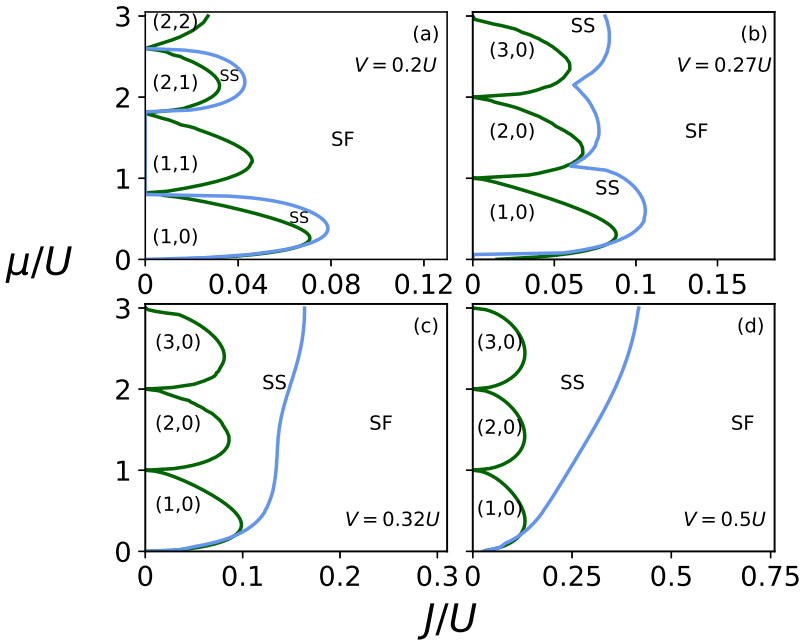

Figure 3.2: The phase diagrams of the eBHM obtained from the CGMF theory with 2×2 clusters for uniform hopping amplitude ($J_x = J_y = J$) at $V/U = 0.2, 0.27, 0.32,$ and 0.5 (a-d). The solid green line indicates the incompressible to compressible MI-SF, DW-SF and DW-SS phase boundaries. The solid blue line represents the SS-SF phase boundary. Here the DW and MI phases are indicated by their sublattice occupancies (n_A, n_B).

with the CGMF is reported in [160]. However, the DW lobes are suppressed with the 2×2 cluster. With the use of higher cluster sizes, there can be significant change in J_c values, which is discussed later. The SS domains are also smaller in size with the CGMF theory. Another difference is that at higher values of V and $\alpha = 1/2$, the SS-SF phase boundary commences at $J/U \approx 0$ and $\mu/U \approx 0$ with the SGMF theory, while with the CGMF theory, the SS-SF boundary starts at finite value of J/U and $\mu/U = 0$ [Fig. 3.2(c,d)]. Our results demonstrate the greater accuracy of the CGMF theory by correcting the overestimation of the SS domain obtained from the single-site mean-field theory. Similar corrections of the mean-field results is obtained by using the QMC [74, 75]. Another notable difference is that the SS-SF phase boundary for large V/U is linear with SGMF theory, while it is curved with the CGMF theory. Qualitatively, the value of J_c obtained using SGMF and CGMF are close to the QMC results available in the literature. The value of J_c/U of the DW(1,0) - SS quantum phase tran-

sition at $zV/U = 1$ obtained using SGMF and CGMF methods are 0.0841 and 0.0832, respectively, and the QMC result is 0.0822 [74]. This further justifies the progressive decrease of J_c/U of the DW-SS transition. We can systematically study the change in the value of J_c of various QPTs by using clusters of larger size. Such an analysis - cluster finite-size scaling, is discussed in the next subsection.

3.2.2 Cluster finite size scaling

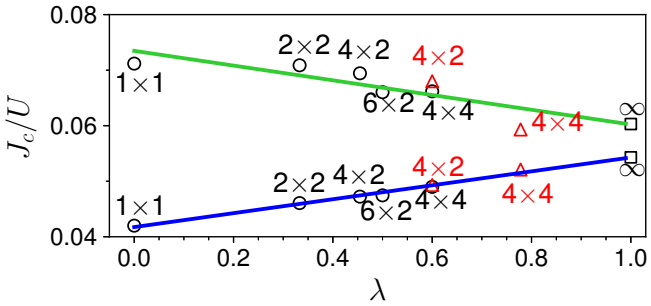

Figure 3.3: The finite size scaling of J_c for (1,1) MI-SF (blue) and (1,0) DW-SS (green) transition for different cluster sizes. The circles (triangles) represent the critical values obtained using periodic boundary conditions along both (one) spatial dimension. The square symbols represent the exact values in the thermodynamic limit. The scaling is performed for $\alpha = 0$ and $V = 0.2U$.

The phase diagrams obtained from the 2×2 cluster show a correction over the ones obtained by the SGMF theory. This is because of the better representation of the quantum fluctuations with the 2×2 cluster. To incorporate better quantum correlation effects, we can work with higher cluster sizes. However, the computation of an entire phase diagram with the larger cluster sizes is compute extensive as the size of the Hilbert space increases exponentially with cluster size. Hence, it is often reasonable to study the shift of the critical J_c/U value with an increase of the cluster sizes. This study is referred to as the cluster finite-size scaling. This analysis provides the location of the phase boundary in the thermodynamic limit. As a case study, we examine the location of the DW and MI lobe tips J_c for $\alpha = 0$, and $V = 0.2U$. We consider a series of square and rectangular clusters of size $N_C = 2 \times 2$, 4×2, 6×2, and 4×4 for this analysis. We also include the results from 4×2 and 4×4 clusters with

exact hopping along one spatial direction. Note that we have used the clusters with even number of sites along the x and y direction so that the underlying checkerboard pattern is obtained. We use the scaling parameter $\lambda = N_{\mathrm{B}}/(N_{\mathrm{B}} + N_{\delta\mathrm{B}})$ which varies from 0 to 1. Here, N_{B} is the number of intracluster bonds and $N_{\delta\mathrm{B}}$ is the number of bonds at the boundary which couples with neighbouring clusters through the mean-field terms [160, 194]. For the SGMF theory, $N_{\mathrm{C}} = 1 \times 1$ which corresponds to $\lambda = 0$, while $N_{\mathrm{C}} = \infty$ results correspond to $\lambda = 1$. Thus, λ is a measure of the correlations considered by using the clusters of varying sizes. Thus, the value of J_c improves as λ of the cluster approaches to 1.

The finite size scaling analysis for the DW $(1, 0)$ and MI $(1, 1)$ phases with $\alpha = 0$, and $V = 0.2U$ are shown in Fig. 3.3. As is evident from the figure, the J_c/U of the tip of MI lobe increases as λ increases. That is, the overestimation of the SF phase by the SGMF is corrected with the use of clusters, leading to an enhancement of the MI lobe. Based on the linear fit, the thermodynamic limit of J_c is 0.05428. The results from the exact hopping in one direction (shown by the red color) have higher λ as there are lesser bonds coupled to the mean field. The scaling behaviour of J_c is in good agreement with the scaling results of MI-SF in BHM [160, 195].

For the DW $(1, 0)$ - SS transition, we observe a decrease of J_c with increasing cluster size. The domain of the DW order shrinks with larger clusters, which also implies that the SGMF theory overestimates the DW order. The important point is, this phase transition shows an opposite trend as compared to the MI-SF phase transition. From the finite size scaling analysis, the linear fit gives the thermodynamic limit of J_c as 0.06021. This trend of J_c is also reported in earlier studies of hard-core eBHM [90, 194]. Furthermore, the scaled J_c values of eBHM phase boundaries at $zV/U = 1$ are in good agreement with the QMC results [74].

3.2.3 Artificial gauge field

There has been tremendous experimental progress to simulate the effect of magnetic fields on the charge neutral cold atoms. In particular, a combination of laser fields can be utilized to make the atoms experience the equivalence of Lorentz force. These fields are in general, referred to as artificial gauge fields. The presence of the artificial

gauge field introduces the Peierls phase in the hopping, and the modified Hamiltonian is [150, 196]

$$\begin{aligned}\hat{H}_{\text{eBHM}} &= -\sum_{p,q} J\left(e^{i2\pi\alpha q}\hat{b}^{\dagger}_{p+1,q}\hat{b}_{p,q} + \hat{b}^{\dagger}_{p,q+1}\hat{b}_{p,q} + \text{H.c.}\right) \\ &+ \sum_{p,q}\hat{n}_{p,q}\left[(\epsilon_{p,q}-\mu) + \frac{U}{2}(\hat{n}_{p,q}-1)\right] \\ &+ \sum_{p,q} V_{p,q}\,\hat{n}_{p,q}\,(\hat{n}_{p+1,q}+\hat{n}_{p,q+1}) \end{aligned} \tag{3.3}$$

where the strength of the magnetic field is reflected in the number of flux quanta per plaquette $\alpha = (e/\hbar)\int d\mathbf{r}.\mathbf{A}(\mathbf{r})$. and $0 \leqslant \alpha < 1$; $\mathbf{A}(\mathbf{r})$ is the vector potential leading to the synthetic magnetic field $\mathbf{B} = \nabla \times \mathbf{A}$, the atoms acquire a $2\pi\alpha$ phase while hopping around a plaquette. The Hamiltonian in Eq. 3.3 is written in the Landau gauge, where the vector potential $\mathbf{A}(\mathbf{r}) = -By\hat{x}$. At zero magnetic field, the system possesses the translational invariance along both axes, while with the magnetic field, the system preserves the invariance only along the x-axis of the lattice. It is possible to introduce artificial gauge fields in experiments with lasers [97, 197–199].

We consider $\alpha = 0.5$ to study the effect of artificial gauge field on the quantum phases of the eBHM. The dashed lines in the phase diagram are with $\alpha = 0$, while the solid lines are $\alpha = 0.5$. We first consider the SGMF theory to obtain the ground state phase diagrams. It is evident from Fig. 3.4 that the artificial gauge field modifies the phase boundaries of MI, DW and SS phases. As an example, the tip of the DW $(1,0)$ lobe for $V/U = 0.2$ is enhanced from $J_c/U \approx 0.0717$ by 40% to 0.101 with artificial gauge field. This enhancement in the insulating lobes and the phase boundaries of MI (DW) - SF (SS) transition with artificial gauge field is in agreement with the site-decoupling theory given in [193]. The tip of the SS lobe is enhanced from $J_c/U \approx 0.084$ to ≈ 0.119 implying a larger domain of SS phase surrounding the DW(1,0) phase. This is a crucial point as the artificial gauge fields can serve better to identify the SS phases in the ultracold atoms owing to larger phase domains. The enhancement in the quantum phases can be understood from the localizing effect of the Landau quantization on the itinerant bosons. Additional differences can be noted by studying the phase diagrams obtained in the presence of gauge fields using the CGMF theory given in Fig. 3.5. As an example, in the presence of the gauge fields, the tip

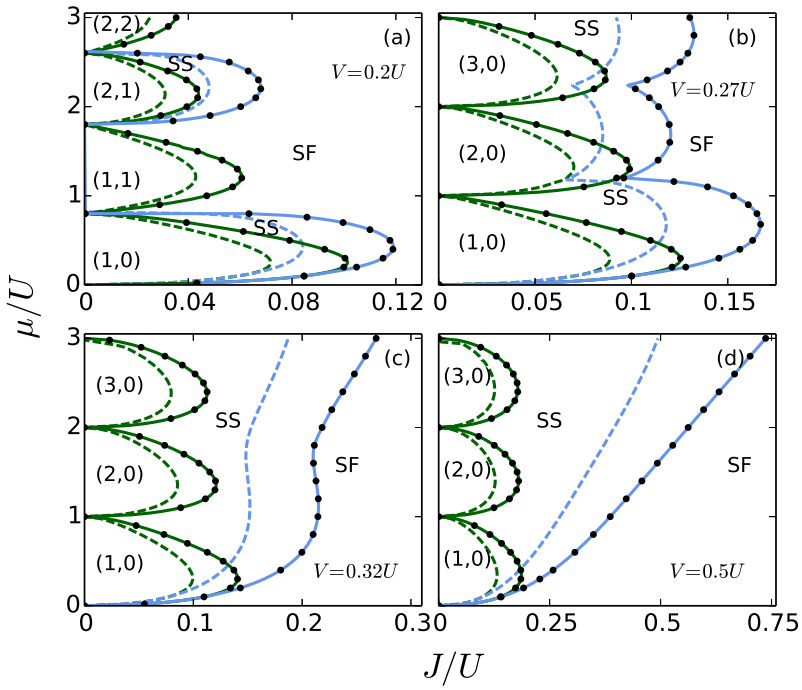

Figure 3.4: The phase diagrams of the eBHM with uniform hopping amplitude ($J_x = J_y = J$) for $V/U = 0.2, 0.27, 0.32$, and 0.5 (a-d). The plots show the phase boundaries for two cases $\alpha = 0$ and $\alpha = 1/2$. The dashed (solid) green line indicates the MI-SF, DW-SF and DW-SS phase boundaries for $\alpha = 0$ ($\alpha = 1/2$) case. The dashed (solid) blue line represents the SS-SF phase boundary for $\alpha = 0$ ($\alpha = 1/2$) case. The phase boundaries for $\alpha = 1/2$ case are obtained using the Landau gauge. The data points obtained using the symmetric gauge are represented by black solid filled circles. Here, the DW and MI phases are indicated by their sublattice occupancies (n_A, n_B).

of the DW $(1, 0)$ lobe is increased from $J_c/U \approx 0.101$ in SGMF to $J_c/U = 0.110$ in CGMF. This increasing trend of J_c/U for the DW-SS transition in presence of the gauge fields is opposite to the one without the gauge fields. The stability of soft-core SS phase is consistent with the QMC results of Ref. [73, 74]. In addition, the results also demonstrate the stability of the SS phase in the presence of the artificial gauge field.

We also check the gauge-invariance of the phase boundaries obtained using the SGMF and CGMF method. To do that, we use the symmetric gauge and compute the phase boundaries for $\alpha = 0.5$. The vector potential is $\mathbf{A}(\mathbf{r}) = (1/2)(-By\hat{x} + Bx\hat{y})$ for the symmetric gauge. We observe that the phase boundaries obtained from the

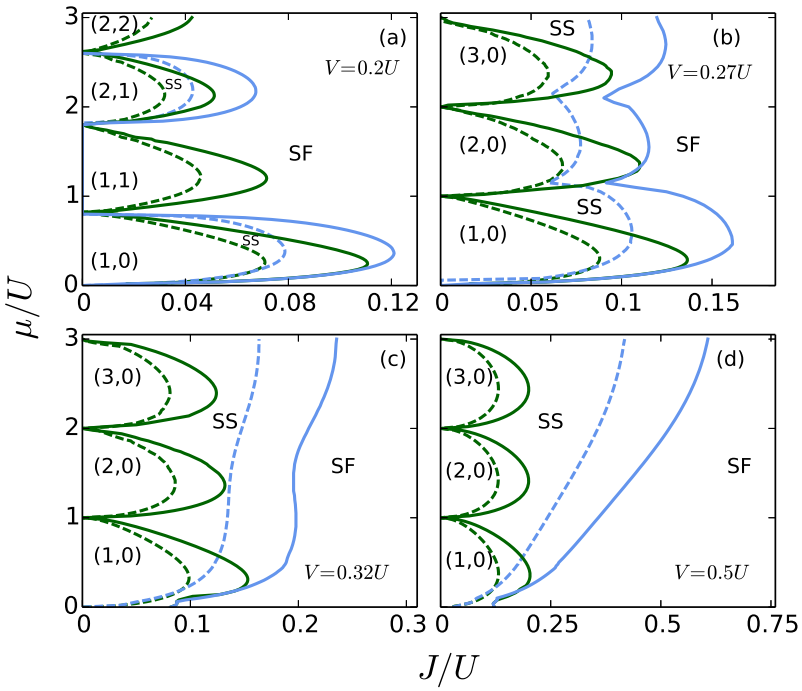

Figure 3.5: The phase diagrams of the eBHM obtained from the CGMF theory with 2×2 clusters for uniform hopping amplitude ($J_x = J_y = J$) at $V/U = 0.2, 0.27, 0.32,$ and 0.5 (a-d). The plots show the phase boundaries for two cases $\alpha = 0$ and $\alpha = 1/2$. The dashed (solid) green line indicates the MI-SF, DW-SF and DW-SS phase boundaries for $\alpha = 0$ ($\alpha = 1/2$) case. The dashed (solid) blue line represents the SS-SF phase boundary for $\alpha = 0$ ($\alpha = 1/2$) case. Here the DW and MI phases are indicated by their sublattice occupancies (n_A, n_B).

symmetric gauge are in excellent agreement with those from the Landau gauge. This can be seen from Fig.(3.4), where the filled black circles are the data points obtained using the symmetric gauge. Similar overlap of the Landau and the symmetric gauge results is observed for the CGMF theory as well. The SS-SF phase boundaries are gauge-invariant as well. Thus, the SGMF and CGMF methods give gauge-invariant phase boundaries. This is consistent with the expectation that the observable quantities are gauge invariant [200, 201]. It also shows that the numerical methods we have used are robust as the results are gauge invariant.

3.3 Summary of the Chapter

In this chapter, we have studied certain equilibrium phase diagrams of the eBHM. In particular, we have focused on the effect of the artificial gauge fields on the novel supersolid phase. The enlargement in the domain of the SS phase in the presence of the artificial gauge fields shall be an experimental advantage in studying the properties of the supersolid phase. In the context of the artificial gauge fields, we have demonstrated the gauge invariance of the phase boundaries of the phase diagrams. We have also discussed the effects of incorporating better fluctuations by considering large cluster sizes. In this cluster finite-size scaling analysis, we have noticed that the density-wave to supersolid phase boundary shifts to lower critical values of the hopping parameter. This is contrast to the Mott Insulator to superfluid phase boundary which enhances with larger clusters.

Chapter 4

Quench dynamics of ultracold bosons in optical lattices

In the previous chapter, we have discussed the equilibrium quantum phases of the ultracold atoms trapped in optical lattices. We have studied the phase diagrams of the prototypical Bose-Hubbard model and its variants used for modeling these systems. We shall now focus on the non-equilibrium aspects of these quantum systems. The evolution state in the Hilbert space is rich and sheds light on the ground state and the excited states of the system. Understanding such dynamics is of paramount importance for developing quantum technologies. The real-time evolution of the quantum setups in the experiments is crucial, for example, in the state preparation: certain non-adiabatic effects set it when a critical point of a phase transition is crossed; then it would be important to understand the dynamical properties to reduce these excitations. The promising quantum computing technologies involves real time manipulations of an initial quantum state which again requires an understanding of the dynamics of these quantum systems. An important insight can be gained by understanding the route to the equilibrium of a non-equilibrium initial quantum state. There are different approaches to take a quantum system out of equilibrium - connecting the system to an external bath or applying a driving field. One simple way is by changing one of the parameters of the underlying Hamiltonian of the system. By doing this, an initial quantum state which is an equilibrium state of the initial Hamiltonian, goes out of equilibrium, and shall try to approach the eigenstate of the final Hamiltonian corresponding to the

changed parameter value. This process of changing a parameter is called the quench. The quenching process can be of two types: sudden quench in which the parameter is changed abruptly, and then the system is allowed to evolve under the action of a new Hamiltonian; or slow quench in which the parameter is changed over some time duration. This thesis will focus on the slow quenches or finite rate quenches in the system of ultracold atoms across certain QPTs.

Ultracold atoms in optical lattices are ideal candidates to study the dynamics of closed interacting quantum systems. The long coherence times, minimal interaction with the environment and experimental feasibility for controlling the system parameters make them the workhorse systems for studying the quantum dynamics. The quenching across one or multiple QCP often leads to interesting scenarios. Intuitively, the idea is to investigate how the spontaneous symmetry is broken in the dynamics as the QCP is crossed. In such a scenario, the slow variation of tuning the parameter across the QCP leads to the non-adiabatic dynamics near the critical point, characterized by excitations and topological defects. The reason for the loss of the adiabaticity is the divergence of the relaxation time near the critical point (which is referred to as critical slowing down). A cornerstone to understanding these excitations and topological defects formation for quenches across the continuous phase transitions is the Kibble-Zurek mechanism (KZM), which is described in the next section. The KZM predicts universal scaling laws of certain physical quantities with respect to the quench rate. The study of the universality in the quantum dynamics and the governing critical exponents is important and not settled as that of the universality of equilibrium quantum systems. Another aspect of the quench dynamics studies concerns the route to equilibrium of an initial non-equilibrium quantum state. The properties of the steady state after the quench are also extensively studied. In this context, understanding the thermalization of a quantum system is an active area of research [111, 202].

We begin this chapter by deriving the key equations of the scaling laws predicted by the KZM theory. Then, we shall study the quench dynamics across the QPTs of the BHM and dipolar BHM models, and investigate the universality in the quench dynamics across these QPTs.

4.1 Kibble-Zurek Mechanism

4.1.1 Introduction

The Kibble-Zurek mechanism is a theory that describes the non-equilibrium dynamics of the system when quenched across continuous phase transitions. When an external parameter - like the temperature or pressure or a parameter of the Hamiltonian is quenched with a finite rate across the critical point, the non-adiabatic effects set in. This breakdown of the adiabaticity near the critical point is inevitable due to the critical slowing down, which refers to the divergence of the relaxation time of the system near the critical point. Based on this non-adiabatic regime in the dynamics, KZM describes the spontaneous symmetry breaking and the associated formation of the broken symmetry domains. The key predictions of this theory are certain universal scaling laws with respect to the quench rate.

The pioneering works by Tom Kibble [109, 203] on the early universe constitute the roots of this theory. Kibble studied the formation of the topological defects during the cooling of the early universe. After the Big Bang, the universe expanded and cooled, undergoing different cosmological phase transitions. This led to the spontaneous symmetry breaking and the occurrence of a non-zero order parameter. However, Kibble argued that the choice of the broken symmetry should be limited to the causally connected regions. That is, there would be regions of space where the order parameter value is correlated. Moreover, outside these domains, the order parameter values will not be correlated. Then, the meeting points or boundaries of different domains constitute a defect. Kibble studied the dependence of the defect formation on the topology of the manifolds corresponding to the degenerate symmetry choices of the system, and so these defects are referred to as topological defects.

An important step in further developing the KZM theory was done by Wojciech H. Zurek in the novel work [110]. He tested the ideas of Kibble of the topological defect formation in non-relativistic condensed matter system like the He^4 . However, the key point employed in this work was the critical slowing down, which means the divergence of the relaxation time of the system near the critical point. Zurek demonstrated that the competition between the relaxation time and the quench rate determines the

size of the broken symmetry domains being formed across the critical point. Thus, unlike the cosmological setting, the relativistic causality does not govern the size of the ordered domains in non-relativistic condensed matter systems. He derived a set of scaling laws for the topological defects being produced in the quench. These set of ideas together constitute the KZM. The key testable predictions of the KZM are the universal scaling laws of the size of the domains and the associated defect density as a function of quench rate. We shall now discuss the theoretical aspects of the KZM and derive the KZ scaling laws.

4.1.2 Theory

For a second order phase transition, the correlation length ξ and the relaxation time τ of the system diverge at the critical point. This divergence is responsible for the critical phenomena observed near the critical point of a phase transition [2]. For many phase transitions, this is a power-law divergence governed by the critical exponents:

$$\xi \propto |\epsilon|^{-\nu} \tag{4.1}$$

and

$$\tau \propto |\epsilon|^{-\nu z}. \tag{4.2}$$

The exponent ν characterizes the divergence of the correlation length, and z is the dynamical critical exponent. Here the parameter ϵ is the reduced distance from the critical point of the phase transition. Let us denote the quenching parameter by the symbol J, and assume that this parameter is quenched from $J_i < J_c$ to $J_f > J_c$, where J_i, J_c and J_f represent the initial, critical and the final value of the parameter J. Without any loss of generality, we can set $J_i = 0$. Thus, we have

$$\epsilon = \frac{J - J_c}{J_c}. \tag{4.3}$$

We assume that the initial state of the system is in the symmetric phase for $J < J_c$, while for $J > J_c$, this symmetry is spontaneously broken, giving rise to a non-zero order parameter. When the parameter J is slowly quenched across J_c, the reduced distance ϵ becomes time dependent. Near the critical point, a linearized quench protocol can be assumed:

$$\epsilon(t) = \frac{t}{\tau_Q}. \tag{4.4}$$

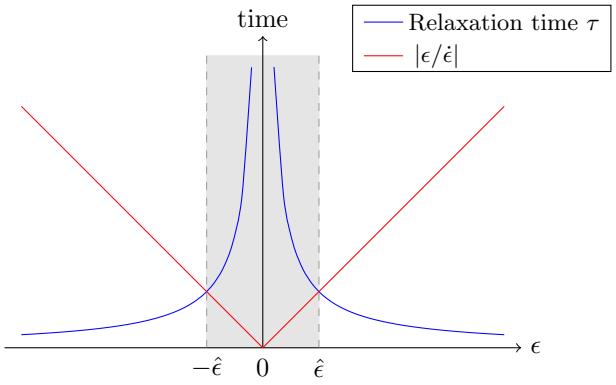

Figure 4.1: The relaxation time (blue) and the inverse transition rate $|\epsilon/\dot{\epsilon}|$ (red) as a function of the ϵ. The relaxation time equals the inverse transition rate at $-\hat{\epsilon}$ and $\hat{\epsilon}$. The shaded region between $-\hat{\epsilon}$ and $\hat{\epsilon}$ is the impulse regime, whereby the system's relaxation time is larger than the timescale of the transition.

Here the quench time τ_Q determines the rate of the quenching. With this protocol, the critical value J_c is crossed at $t = 0$. We further assume that the quench is initiated at time $t = -\tau_Q$ so that $J(-\tau_Q) = J_i = 0$. The fate of the evolving state of the system is determined by the relaxation time. When the quench parameter is far away from the critical point, the relaxation time of the system is small. In this case, the evolution is adiabatic and the evolving state is close to the actual ground state. However, as the critical point is approached, the divergence of τ breaks the adiabaticity of the system. Thus, there are two adiabatic regimes separated by a non-adiabatic regime close to the critical point. The switch between these different regimes is of interest in the KZM theory. To understand this point further, consider the time scales as shown in the Fig. 4.1.

There are two competing time scales in the dynamical evolution. The first time scale corresponds to the one at which the parameter is quenched. That is, the time scale is related to the inverse transition rate, or the rate at which the parameter is being quenched. This inverse transition rate is given as $|\epsilon/\dot{\epsilon}|$. The second time scale is the relaxation time of the system. In Fig. 4.1, we plot these two times as a function of reduced distance ϵ. For $\epsilon \ll 0$ (corresponding to negative initial times), the inverse transition rate is larger than the relaxation time of the system. That is, the time scale

on which the system parameter is quenched is larger than the relaxation time, and therefore the system "adjusts" to the variation of the parameter. This is the adiabatic regime in the evolution, where the evolving state remains close to the ground state. This lasts till $-\hat{\epsilon}$ after which the relaxation time of the system is larger. This persists till $\hat{\epsilon}$. Thus, in the regime between $-\hat{\epsilon}$ to $\hat{\epsilon}$, the system is unable to adjust itself according to the parameter that is quenched due to the diverging relaxation time. In the KZM framework, this region is called the impulse regime. The dynamics of the system is assumed to be frozen in this region. The post-impulse adiabatic regime begins from $\hat{\epsilon}$ since the relaxation time becomes smaller than the transition time. Thus based on the Fig. 4.1 and the discussions, the switching between the adiabatic and impulse occurs when

$$\tau(\hat{\epsilon}) = \left|\frac{\hat{\epsilon}}{\dot{\hat{\epsilon}}}\right| \tag{4.5}$$

Using the power-law divergence of τ: $\tau \propto 1/|\epsilon|^{\nu z}$, a scaling relation for the switching $\hat{\epsilon}$ can be determined.

$$\begin{aligned} \tau(\hat{\epsilon}) &= \left|\frac{\hat{\epsilon}}{\dot{\hat{\epsilon}}}\right| \\ 1/|\hat{\epsilon}|^{\nu z} &= \left|\frac{\hat{\epsilon}}{\dot{\hat{\epsilon}}}\right| \\ 1/|\hat{\epsilon}|^{\nu z} &= |\hat{\epsilon}|\tau_Q \\ |\hat{\epsilon}| &\propto \tau_Q^{-1/(1+\nu z)} \end{aligned} \tag{4.6}$$

Based on the scaling relation given in Eq. (4.6) and the quench protocol, we can write the scaling relation for the transition time instant $\hat{t}$ -

$$\hat{t} \propto \tau_Q^{\nu z/(1+\nu z)}. \tag{4.7}$$

Note that the time spent in the impulse region by the system increases as the quench is made slow, as stated by Eq. (4.7). However, the reduced distance ϵ becomes smaller, due to the negative exponent in Eq. (4.6). That is, the system gets closer to the critical point as the quench is made slower. A comparison for two different quench rates is provided in the Fig. 4.2.

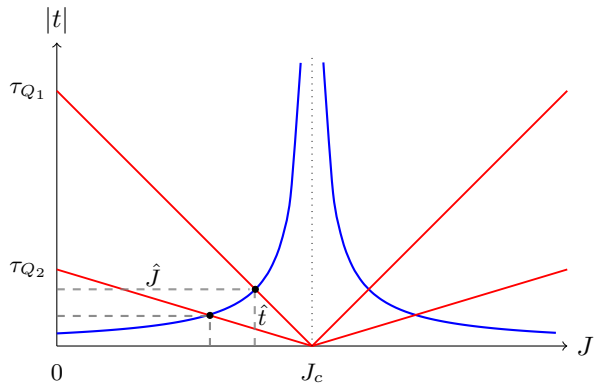

Figure 4.2: Schematic illustration of the adiabatic and impulse regimes for two quench rates. For $\tau_{Q_1} > \tau_{Q_2}$, the $\hat{t}_1 > \hat{t}_2$, as seen by the y-intercept. However, the reduced distance $\hat{J} - J_c$ is lesser for τ_{Q_1} than in τ_{Q_2}, illustrating that for slow quenches, the width of the impulse region in terms of the reduced distance is lesser.

The timescale of the transition $\epsilon/\dot{\epsilon} = t$ can be expressed as

$$t = \tau_Q \left(\frac{J}{J_c} - 1 \right). \tag{4.8}$$

In Fig. 4.2, we plot $|t|$ for a better representation along the y axis. So for $J = J_i = 0$, we have $|t| = |\tau_Q|$. As shown in Fig. 4.2, we consider two quench times $\tau_{Q_1} > \tau_{Q_2}$. The two lines corresponding to the two quench rates intersect the relaxation time at different points. But the trend is such that for large quench times, or slower quenches, the system gets closer to the critical point $\hat{J} \to J_c$, and the intermediate impulse regime is narrow. However, the time that it spends in the impulse domain, given by the y ordinate of the intersecting points, is large for the slow quenches: $\hat{t}_1 > \hat{t}_2$.

After the time $\hat{t}$, the dynamics of the system becomes adiabatic. The frozen state in the duration $[-\hat{t}, \hat{t}]$ is an initial state for the adiabatic dynamics that follows after $\hat{t}$. The correlation length at $-\hat{\epsilon}$ gets imprinted onto the system. Since the post-impulse adiabatic regime lies in broken symmetry parameter domain ($J > J_c$), the spontaneous symmetry breaking occurs, and non-zero order parameter develops. But due to the finite correlation length $\hat{\xi} = \xi(-\hat{\epsilon})$, domains of size $\hat{\xi}$ are formed. That is, the system undergoes a spontaneous symmetry breaking and choose a uniform order parameter within a distance $\hat{\xi}$. Using the divergence of correlation length: $\xi \propto |\epsilon|^{-\nu}$, the scaling relation for $\hat{\xi}$ can be obtained.

$$\begin{aligned} \xi &\propto |\epsilon|^{-\nu} \\ \hat{\xi} &\propto |\hat{\epsilon}|^{-\nu} \\ \hat{\xi} &\propto \tau_Q^{\nu/(1+\nu z)}. \end{aligned} \tag{4.9}$$

We denote the exponent of $\hat{\xi}$ as b, that is $b = \nu/(1+\nu z)$.

An important consequence of the KZM then is in the scaling of the topological defect density with the quench rate. The defect density N at $\hat{t}$ should scale as [110, 204]:

$$\begin{aligned} \hat{\xi} &\propto \tau_Q^{\nu/(1+\nu z)} \\ \hat{N} &\propto \hat{\xi}^{\mathrm{def}}/(\hat{\xi})^D \\ \hat{N} &\propto \tau_Q^{(\mathrm{def}-D)\nu/(1+\nu z)} \end{aligned} \tag{4.10}$$

where D is the spatial dimension and def is the dimension of the defect. For the point-like defects like vortices, the $\mathrm{def} = 0$. The exponent of the defect density can be denoted as d, i.e $N \propto \tau_Q^{-d}$, so that $d = (D - \mathrm{def})\nu/(1+\nu z)$. From Eq. (4.9) and Eq. (4.10), we obtain a scaling relation between the critical exponents -

$$d = (D - \mathrm{def})b. \tag{4.11}$$

The origin of these topological defects are the meeting points of domains corresponding to different order parameter choice. As an example, there is $U(1)$ symmetry breaking when the temperature T of a Bose gas is cooled below T_c, thereby the wavefunction acquires a phase. However, as per the KZM, the domains of different phases shall be generated in the dynamics. In this case, the defects are the vortices that are formed at the meeting point of three or more domains. It is to be noted that the estimate of the defect density is accurate only upto the order of magnitude [112, 129]. The prediction often overestimates the actual density of defects obtained numerically. In such situations, a factor f is multiplied with $\hat{\xi}$ to obtain better estimates, where $f \approx 5 - 10$. However, this deviation does not affect the scaling of the defect density with the quench rate.

Thus the key testable predictions of the KZM are given in Eq. (4.7) - (4.10). The first experimental verification of the KZM predictions were performed with superfluid helium [116–118]. In [116], the superfluid He^4 was used and qualitative verification of the vortices being produced in the dynamics was done. In the later works [117, 118], superfluid He^3 was preferred due its resemblance of the broken symmetries that describe the early universe. The quantitative calculations of the vortices being produced were obtained. In this way, the justification of the scaling law was obtained. The KZM was originally developed and tested for thermal phase transitions. Later it was extended to the QPTs as well. One of the pioneering effort in this direction was the work in [129] that tested the predictions of the KZM for a 1D quantum Ising model. For the quantum systems, the relaxation time is inversely proportional to the energy gap Δ between the ground state and the first excited state. This gap vanishes at the QCP, which leads to the divergence of the relaxation time. This is similar to the critical slowing down for the thermal phase transitions, and thus the dynamics can be splitted into the near critical impulse regime and adiabatic regimes away from the QCP. The scaling relations can then be derived in a similar manner. Though it looks as a easy extension, the unitary dynamics of the QPTs is very different from the damping dynamics in the presence of a thermal bath for thermal phase transitions. Following the development of the quantum analogue of the KZM, there are several works in recent times which have tested the quantum KZM theoretically [130, 205–220] and experimentally [136–140, 221–223]. As discussed earlier, ultracold atoms exhibit plethora of quantum phases and the associated QPTs and are ideal systems to study the quench dynamics across the QPTs. In the context of the KZM, there are many works done using the ultracold atoms. The early investigations in the ultracold atoms were for harmonic trapping potentials [221, 224–228]. The experimental investigations of the dynamics of the QPT from the MI phase to the SF phase have been studied [136, 142]. On the theoretical side, there have been works investigating the evolution of the ground states during the quench process [115, 129, 143, 205, 207, 229–231].

In the quantum systems with a trapping potential, the effect of the inhomogeneity needs to be accounted in deriving the analogous Inhomogeneous Kibble-Zurek mechanism (IKZM). In such an analysis, a local critical value of the quenching parameter and

local quench rate are introduced [232–235]. Depending on the speed of the quench, the defect formation can be completely suppressed in the IKZM. Also, the assumption that the evolving state freezes-out in the impulse regime has been recently revisited. Coarsening of the defects being produced is observed in the impulse regime, thereby dismissing the frozen state approximation [236–238].

In this chapter, we shall consider the quantum quench dynamics across certain quantum phase transitions exhibited by the ultracold atoms in optical lattices. We study the non-equilibrium dynamics across these QPT from the KZM perspective, thereby obtaining the universal KZM scaling laws. We first discuss the quench dynamics across the MI-SF phase transition for the neutral bosonic atoms in optical lattice. Next, we consider the dipolar bosonic atoms and study the quench dynamics. The anisotropy of the dipolar interaction leads to structured quantum phases. In our study, these are the quantum phases of the checkerboard and stripe density ordering. We shall discuss the KZM scaling laws and the critical exponents for the QPTs exhibited by the dipolar atoms. After focusing on the continuous phase transitions, we shall also discuss the polarization angle quenching leading to the structural QPT between the stripe and checkerboard ordering. This QPT corresponds to the first order QPT, and we investigate the universality akin to the KZM for continuous QPTs.

4.2 Quench dynamics across Mott-Insulator to Superfluid phase transition

Ultracold atoms in optical lattice constitute novel quantum systems that are used to probe the strongly interacting regimes. As discussed before, BHM is apt to describe these systems and it exhibits two quantum phases: the MI and SF quantum phases. In this section, we shall discuss the quench dynamics across the MI-SF QPT, and obtain the KZ scaling laws. We shall demonstrate the number of SF domains formed, and verify the power-law scaling of it with the quench rate. The quench dynamics across this QPT has been previously studied experimentally [136, 142], and the theoretical predictions of the critical exponents are verified. On the theoretical side too, there are studies investigating the KZ scaling laws with sophisticated numerical techniques like the

truncated Wigner approximation [239], time-dependent Gutzwiller [143], variational wavefunction [209]. The KZM scaling laws investigated using the time-dependent Gutzwiller methods in [143] do not yield exponents satisfying the scaling relations. The work presented below, however, demonstrates a precise way to locate the time $\hat{t}$, and the exponents obtained thereafter are shown to obey the scaling relations. To begin with, we first discuss the equilibrium phase diagram and the quench protocol employed in our simulations. Next, we shall present the results of the quench dynamics across the MI-SF transition induced by varying the hopping strength J.

4.2.1 Equilibrium phase diagram

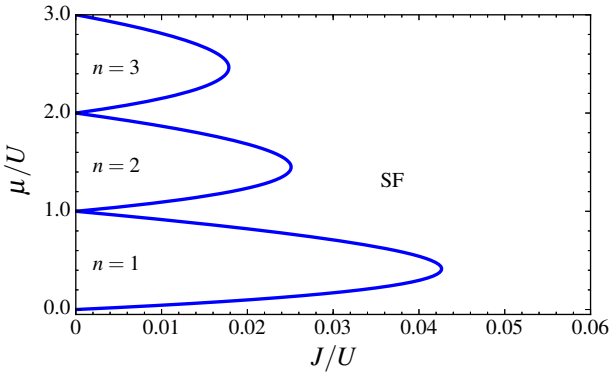

Figure 4.3: The phase diagram of the BHM in the $J/U - \mu/U$ plane, computed using the SGMF method.

The ground state phase diagram of the BHM in the $J/U - \mu/U$ plane, at zero temperature is shown in Fig. 4.3. The phase diagram is obtained by using the SGMF method and the Gutzwiller ansatz. It comprises of the characteristic MI lobes, whereby each lobe corresponds to an integer commensurate filling. The MI phase is obtained in the strongly interacting limit $J/U \to 0$ whereby the strong intersite repulsion prevents the hopping and renders the atoms pinned to the lattice sites. As discussed in Chapter 2, the SF order parameter $\phi = \langle \hat{b} \rangle$ is used as an order parameter to distinguish the MI and SF phase. It is non-zero in the SF phase, and zero in the MI phase. The MI-SF transition, at the tip of the Mott lobes, belongs to the $(D+1)$ dimensional XY model. This is a multi-critical point in the phase diagram. At the tip, the average density does not vary across the critical point, and the transition is driven by the phase fluctuations.

On the other hand, below and above the tip, the phase transition is driven by the density fluctuations and falls in the mean-field universality class [19].

4.2.2 Quench protocol

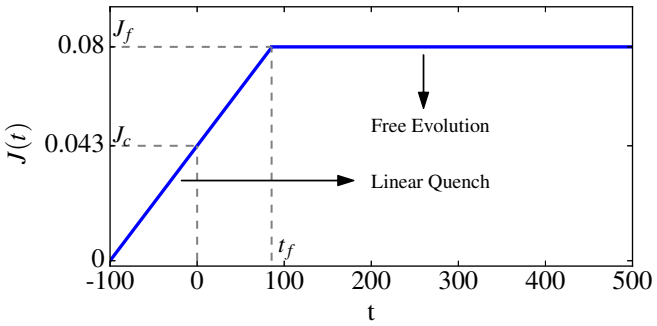

Figure 4.4: A schematic figure to illustrate the quench protocol used in our simulations. The hopping amplitude is ramped up from value J_i to J_c in time τ_Q (here $\tau_Q = 100$). After the quench is terminated at J_f, the system is freely evolved to attain a steady state. The value J_i corresponds to the MI(1) phase, and the value J_f to the SF phase.

For our study, we start from $t = -\tau_Q$ and reach the critical J_c at $t = 0$. That is, in time τ_Q, the hopping amplitude J should change from an initial J_i to J_c. The linear quenching protocol used is

$$J(t) = J_i + \frac{(J_c - J_i)}{\tau_Q}(t + \tau_Q). \tag{4.12}$$

The parameters in the Hamiltonian are scaled with U, and time is defined in the units of $\hbar/U$. We consider $J_i = 0.0U$ and $J_f = 0.08U$, and fix the chemical potential $\mu = 0.41U$. This value of the chemical potential corresponds to the tip of the MI(1) lobe, and the critical value J_c for this μ value is $J_c = 0.043U$. We therefore wish to understand the MI(1) to SF quench dynamics at the tip of the lobe. At $t = -\tau_Q$, the system is in the MI(1) phase, and at $t = t_f$, it is in the SF phase when the quantum quench ends. We consider the system of size 100×100 in our computations, and employ the PBC. These large system sizes facilitate better statistics of the topological defects and the domains formed in the dynamics. The quench protocol employed in our simulations is illustrated in Fig. 4.4, for $\tau_Q = 100$. As demonstrated in the figure, the hopping amplitude is increased till J_f. After that, the system is freely evolved

in time so that a steady state is attained. To initiate the quench, we first obtain the equilibrium wavefunction $|\Psi_i\rangle$ that corresponds to the parameter J_i, using the SGMF method. In the next step of the state preparation for the quench dynamics, we introduce the phase and density fluctuations to the coefficients of the wavefunction. The phase fluctuations are introduced to the non-zero coefficients of the $|\Psi_i\rangle$, by generating univariate random numbers in the domain $[0, 2\pi]$. The density fluctuations are introduced by adding noise to the amplitudes of the coefficients. This is done by generating the univariate random numbers in the domain $[0, \Delta]$, where $\Delta \approx 10^{-4}$. These fluctuations simulate the effects of the quantum fluctuations in the system that are essential to drive the QPT. The strength Δ for the density fluctuations is based on the Bogoliubov modes of the equilibrium SF state. The details are given in the Appendix C. We have consider an ensemble of 80 randomized initial states for reliable statistics. Each of these states are evolved in time using the time-dependent Gutzwiller equations. The derivation of the time-dependent Gutzwiller equations is given in Appendix B. All the physical quantities are obtained by considering the ensemble average over all the 80 samples.

4.2.3 Overlap measure

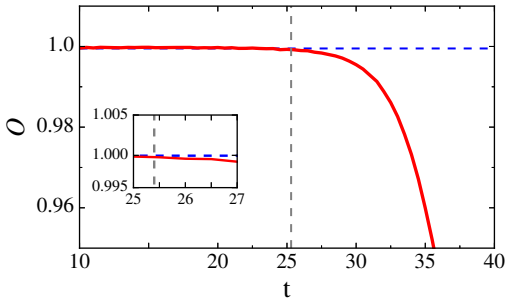

Figure 4.5: Plot of the overlap measure $O(t)$, defined in Eq. (4.13), to locate $\hat{t}$. The red curve indicates the overlap, while the vertical grey dashed line indicates the time $\hat{t}$ at which $O(t)$ begins to deviate from unity. The inset zooms into the region near $\hat{t}$. The dashed blue line is a visual guide to indicate the unity on the ordinate axis.

The KZM scaling laws are applicable at the transition time $\hat{t}$ between the impulse and adiabatic domain. Thus, it is important to identify the time $\hat{t}$ accurately. To locate the $\hat{t}$, we compute the overlap of the wavefunction of the system at $t > 0$ with the

wavefunction at $t = 0$ as

$$O(t) = |\langle \Psi(0) \, | \Psi(t) \rangle \, | \tag{4.13}$$

In the impulse domain, the state of the system is frozen, and it maximally picks up a phase factor [240] in the evolution in the impulse domain. So the overlap $O(t)$ should be equal to unity as long as the system is in the impulse regime or $t \leqslant \hat{t}$. At $\hat{t}$, when it passes from the impulse to adiabatic regime, the overlap shall start to deviate from unity. Thus, computing the $O(t)$, we locate the $\hat{t}$ by noting the time at which it deviates from unity. For numerical purposes, we consider the cutoff on the overlap in the impulse region as 0.9995. As an example, Fig. 4.5 shows a generic plot of $O(t)$ around $\hat{t}$. As discussed above, the key point about the overlap measure is that the evolution of the state is maximally upto a phase factor in the impulse regime. For the incompressible MI(1) phase, the only non-zero basis state that contributes is $|n = 1\rangle$. So the effect of the phase corresponding to this basis state is nullified while taking absolute value, and we get an almost constant overlap value in the impulse domain. However, when the quench dynamics involves a transition from a compressible state, the wavefunction is a linear superposition of different Fock states. We have observed that in the impulse regime, each basis state evolves with an independent phase factor, thereby making the overlap varying in the impulse region. The variations are about the unity value, however, the smoothness is lost, and locating $\hat{t}$ becomes non-trivial using the overlap.

4.2.4 Transition from the MI to SF phase

In this part, we shall discuss the results of the quenching between the MI(1) to SF QPT. As the SF order parameter is used to distinguish between these two quantum phases, we begin our discussions by studying the time evolution of the SF order parameter.

SF amplitude

As a first indicator of the quench dynamics, we consider the average of the amplitude of the SF order parameter, defined as

$$|\Phi| = \sum_{p,q} |\phi_{p,q}|/N_s,$$

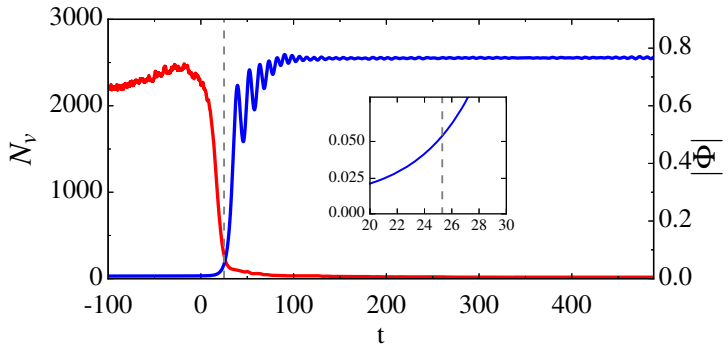

Figure 4.6: The time evolution of the vortex density N_v (red) and $|\Phi|$ (blue) for $\tau_Q = 100$. The QCP is crossed at $t = 0$, and the dashed grey line indicates the time $\hat{t}$. The order parameter $|\Phi|$ rises exponentially after $\hat{t}$, as shown in the inset. The vortex density N_v exhibits a steep decrease after crossing the QCP due to the annihilation of the vortex-antivortex pairs.

where N_s denotes the number of lattice sites. The time evolution of $|\Phi|$ is shown in Fig. 4.6 with the blue colored plot. In the initial stages of the quench dynamics, $|\Phi|$ is small (of order 10^{-3}), as the system is in the MI phase. In the equilibrium MI state, $|\Phi|$ is zero; but in the quench dynamics it is finite due to the fluctuations added to the initial state. As the QCP is crossed at $t = 0$, the system ought to evolve into SF phase for $t > 0$ and acquire a larger $|\Phi|$. However, there is a certain time delay for the increase in $|\Phi|$. We notice an exponential increase of Φ around $\hat{t}$, as depicted in the inset in Fig. 4.6. This delay is because the system is in the impulse domain upto $\hat{t}$, thereby the order parameter does not develop until reaching $\hat{t}$. That is, the symmetry is not spontaneously broken upto the time $\hat{t}$. Thus the delay in the transition to the SF state signifies the impulse domain of the dynamics. Post $\hat{t}$, there is a steep exponential increase of $|\Phi|$, which is discernible from the plot in Fig. 4.6. The quantum quench is terminated for $t \approx \tau_Q$, after which the system is let to free evolve. Once the quench is terminated, the growth of the $|\Phi|$ stops, and it settles to a steady state value in the free evolution.

The $|\Phi|$ is an averaged quantity, and does not sheds light on the local behaviour, or site-wise nature of the SF order parameter. Therefore, we present the snapshots of the $|\phi_{p,q}|$ for one noise realization at different times in Fig. 4.7. The small values of $|\phi_{p,q}|$ at initial time $t = -\tau_Q$ can be seen in Fig. 4.7 (a). The figure also indicates the

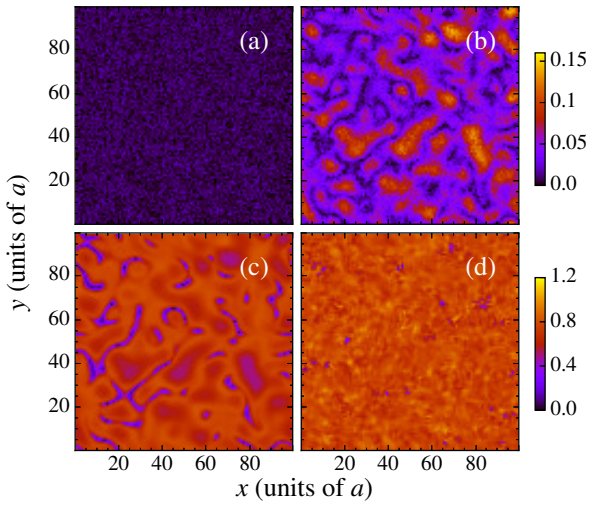

Figure 4.7: Snapshots of $|\phi_{p,q}|$ at certain time instants for $\tau_Q = 100$. At initial time $t = -\tau_Q$, $|\phi_{p,q}|$ is small as shown in (a). After $\hat{t}$, the $|\phi_{p,q}|$ increases and domains of SF are formed. This is shown in panel (b) which is at $t = \hat{t}$. These domains disappear due to the merging as time progresses and the system becomes homogeneous, as shown in panels (c) and (d).

fluctuations present in the values of $|\phi_{p,q}|$. Such profiles are observed until the time $\hat{t}$. Fig. 4.7 (b) shows the profile at $\hat{t}$. The formation SF domains is visible from the plot. The formation of the domains is the signature of the KZM physics. This indicates that there are local choices of the broken symmetry SF phase, resulting into a domain structure. When J/U is further increased, the domains grow in size, and merge through the phase ordering process. This is visible from the Fig. 4.7 (c)-(d), in these figures $|\phi_{p,q}|$ is almost uniform.

Vortex density

Next we discuss the behaviour of the phase of the SF order parameter in the quench dynamics. The MI-SF phase transition breaks the global $U(1)$ symmetry spontaneously, and hence the study of the phase acquired during the evolution becomes important. The domains of different phases can in-fact constitute a vortex, when the phase change across the domains is a multiple of 2π. The vortices are therefore the topological defects formed at the meeting points of different domains in the MI-SF transition. To

quantify the density of the vortices formed, we use [143, 230, 241]

$$N_v = \sum_{p,q} |\Omega_{p,q}|, \tag{4.14}$$

where

$$\begin{aligned} \Omega_{p,q} &= \frac{1}{4}\big[\sin(\theta_{p+1,q} - \theta_{p,q}) + \sin(\theta_{p+1,q+1} - \theta_{p+1,q}) \\ &\quad - \sin(\theta_{p+1,q+1} - \theta_{p,q+1}) - \sin(\theta_{p,q+1} - \theta_{p,q})\big]. \end{aligned} \tag{4.15}$$

Here, $\theta_{p,q}$ is the phase of the SF order parameter $\phi_{p,q}$, that is $\phi_{p,q} = |\phi_{p,q}|\exp(i\theta_{p,q})$. We plot the evolution of the vortex density N_v in Fig. 4.6. The evolution of defect density N_v is complimentary to that of $|\Phi|$. There are large number (≈ 2200) of vortices at the initial time of the quench. This is because of the phase fluctuations imprinted onto the initial state of the system as a part of state preparation. In principle, these are not true vortices as the initial state is MI phase, but these denote the phase windings. The N_v continues to be of this order as there is no transport in the dynamics when the state is in the MI(1) phase. However, after the system crosses the QCP at $t = 0$, we observe a decrease in N_v. The decrease is very steep, and is because of the SF domains that begin to form. Within these SF domains, there is phase coherence, and this prevents any phase discontinuity and thus the presence of a vortex inside a domain. As time progresses, we observe that the N_v decreases. This is because of the phase ordering process that takes place, which tries to establish the global phase coherence throughout the system by the domain mergers. The domain mergers results in the annihilation of the vortex-antivortex pairs, and thus the N_v decreases. We observe these salient features in the time evolution of the N_v in Fig. 4.6.

We plot the phase field of the SF order parameter $\phi_{p,q}$ for different time instants in the quench, in Fig. 4.8. Such a phase field helps in the direct visualization of the phase discontinuities and the associated vortices in the system. As mentioned before, the location of a vortex (antivortex) is defined as the point around which the phase changes by 2π along anti-clockwise (clockwise) direction. At the beginning of the quantum quench $t = -\tau_Q$, as seen from Fig. 4.8(a), many vortices are present in the system. The appearance of the SF domains after the system crosses the critical point is visible in the Fig. 4.8(b), which shows the phase profile at $t = \hat{t}$. There is phase coherence within each of the domains, as can be seen by the near uniform color. This is in

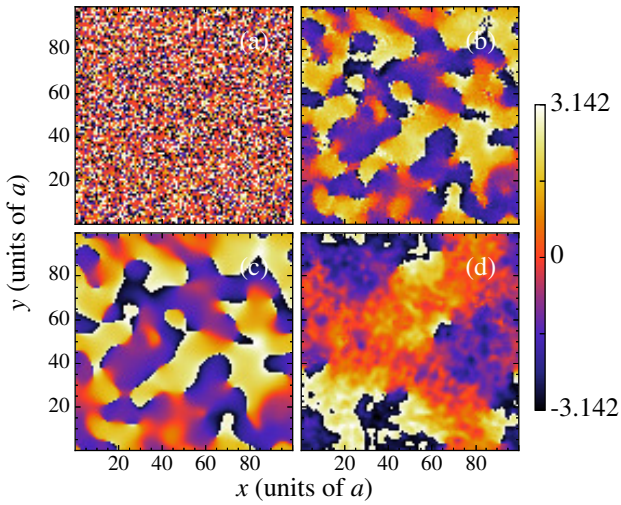

Figure 4.8: Snapshots of the phase of $\phi_{p,q}$ at certain times for $\tau_Q = 100$. Initially at $t = -\tau_Q$, the vortex density is high, as shown in (a), owing to the phase fluctuations imprinted to the system. The domains of uniform phase are formed after the system crosses the critical point, as shown in (b), which is at $t = \hat{t}$. There is phase ordering process which increases the size of the domains and eventually system retains an almost uniform phase, as shown in (c) and (d).

accordance with the KZM, where the $U(1)$ symmetry is spontaneously broken within "correlated regions or domains". The phase discontinuities at meeting points of these domains lead to the vortices. The reduction in the number of vortices (antivortices) through vortex-antivortex annihilation is visible when we compare the plots at later times shown in Fig. 4.8(c-d). From the sequence of the plots, post $\hat{t}$, the consolidation of the domains size or phase ordering in the system is quite prominent.

4.2.5 KZM scaling laws

After understanding the evolution of the order parameters, we study the KZM scaling laws, for the MI-SF QPT. To obtain the critical exponents, we perform a series of computations over quench time τ_Q ranging from 20 to 1000. For the considered set of J_i and J_f, we have observed that $J(\hat{t})$ is greater than J_f, when we reduce τ_Q below $\tau_Q = 20$. These cases are then not interesting as there is no symmetry breaking, and no development of SF order in the system. This is the reason for the lower limit of $\tau_Q = 20$ in our computations. There is no such constraint on the upper bound of τ_Q,

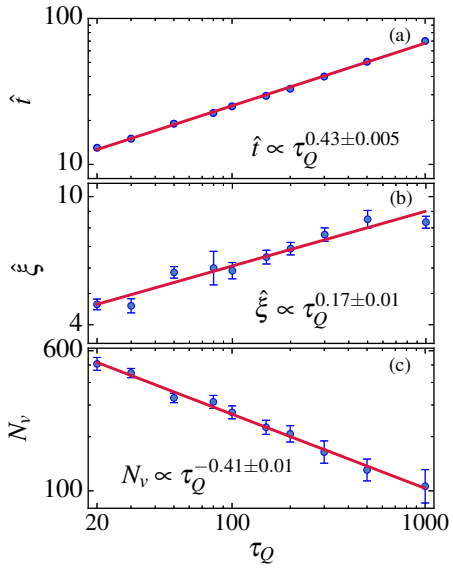

Figure 4.9: Power-law scaling of $\hat{t}$, $\hat{\xi}$ and N_v with respect to τ_Q. The blue error bars denote the standard deviation of the data values. The critical exponents b and d exhibit the scaling relation $d = 2b$.

apart from the exponentially increasing computation times for larger τ_Qs.

We first verify the KZ scaling law for the transition time $\hat{t}$ given in Eq. (4.7). The log-log plot of the values obtained is shown in Fig. 4.9 (a). As discussed previously, the $\hat{t}$ is obtained from the overlap plot. The red line is the least square fit to the data points, and the value of the exponent obtained is 0.43. We average the $\hat{t}$ over the 80 realizations. It is to be noted that the sample-to-sample variation in the $\hat{t}$ is very small (± 0.5). Therefore, we avoid displaying the error associated with the $\hat{t}$ in the plot.

We then compute the correlation length ξ of the system at the time $\hat{t}$. It is defined as

$$\langle b_i^\dagger b_j \rangle \propto \exp\left(\frac{-|i-j|}{\xi}\right). \tag{4.16}$$

For a given pair $\{i, j\}$ of lattice sites, we invert the above relation to calculate ξ for the pair. We then average this quantity over all possible pairs in the lattice, covering all possible spatial separations. We perform an ensemble average of the correlation length over 80 initial noise realizations, for a particular τ_Q. As discussed previously, this correlation length $\hat{\xi}$ is the average size of the SF domains that are formed at time $\hat{t}$, that is the size of correlated broken symmetry domains. The scaling of the ξ at $\hat{t}$ for different τ_Q is shown in Fig. 4.9 (b). The exponent obtained from the fitting is 0.17.

Hence the exponent $b = 0.17$.

The scaling of the vortex density N_v is further shown in Fig. 4.9 (c), and the scaling exponent is 0.41. These scaling laws demonstrate the applicability of the KZM to the second order MI-SF QPT. Furthermore, we observe that the scaling exponent b of the correlation length and d for the vortex density nearly obey the scaling relation $d = 2b$. This is an important feature of our results, as the previous works using the time-dependent Gutzwiller mean-field have obtained exponents that do not obey the scaling relation. Comparing the results of the power-law scaling with Eq. (4.7) - Eq. (4.10), we estimate the equilibrium critical exponents as $\nu = 0.36$, and $z \approx 2$. The exponent z is in good agreement with the mean-field theory prediction ($z = 2$). However, the exponent ν of the equilibrium correlation length differs from the predicted value $\nu = 1/2$. The possible reason might be the lesser correlations captured by the Gutzwiller mean-field theory, which affects the scaling of the correlation length.

We quantify the number of domains of the SF order formed at time $\hat{t}$, and investigate the power-law behaviour with the quench time τ_Q. Since the vortices are point defects, their density and the number of the domains formed are related with τ_Q in a similar way:

$$\begin{aligned} N_D(\hat{t}) &\propto \frac{1}{\hat{\xi}^D} \\ N_D(\hat{t}) &\propto \tau_Q^{-D\nu/(1+\nu z)} \end{aligned} \tag{4.17}$$

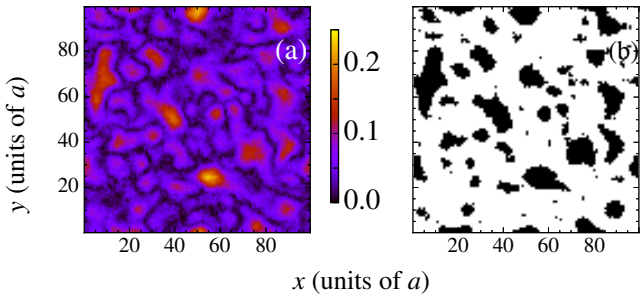

Figure 4.10: (a) The snapshot of the $|\phi_{p,q}|$ at $t = \hat{t}$. The local SF domains are visible in the plot. To count the SF domains, we label the lattice sites belonging to either the MI or SF domain, based on the cutoff $\epsilon = 0.07$. The corresponding snapshot after applying the cutoff is shown in (b). The black domains in in (b) are the SF domains.

We count the number of the SF domains formed at $\hat{t}$ using the percolation algorithm

described in Chapter 2. We first classify the lattice sites corresponding to the MI and SF phases by analysing the SF order parameter of the corresponding site. That is, we set a cutoff ϵ on the amplitude of SF order parameter $|\phi_{p,q}|$ to distinguish the SF phase from the MI phase. The MI regions also have a small non-zero SF order parameter, owing to the initial fluctuations. The value of ϵ is taken as an average of $|\phi_{p,q}|$ over the prominent MI phase regions in the system at $t = 0$. In our computations, based on this definition, we get $\epsilon \approx 0.07$. In Fig. 4.10, we show the snapshot of a configuration of $|\phi_{p,q}|$, and the corresponding image of binary labels obtained after applying the threshold ϵ. The black domains in Fig. 4.10 (b) are the SF domains that are counted using the percolation algorithm. We then calculate the ensemble-averaged value of N_D over the chosen 80 randomized initial states. The scaling of N_D with τ_Q is shown in Fig. 4.11. The least square fit to the data implies the exponent as 0.39, that is $N_D \propto \tau_Q^{-0.39}$. Note that the scaling of the N_D with τ_Q is approximately same as the scaling of the N_v with τ_Q, as expected for the point-defects. Therefore, we have examined the KZM scaling laws for the quench dynamics across the MI-SF phase transition, and have obtained the critical exponents obeying the scaling relations. Furthermore, we have explicitly counted the number of broken symmetry SF domains formed and have shown that its scaling behavior is analogous to that of the vortex density.

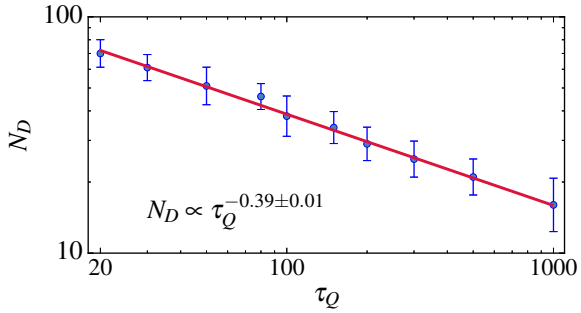

Figure 4.11: Power-law scaling of N_d with respect to τ_Q. The blue error bars denote the standard deviation of the data values. The critical exponent of N_D is in good agreement with exponent of N_v given in Fig. 4.9 (c).

4.3 Quench dynamics of dipolar bosons

In the previous section, we have studied the dynamics across the MI-SF QPT by varying the hopping amplitude in the BHM. The interaction term in the BHM, limited to onsite interactions, does not support the quantum phases with off-site density correlations. As we have discussed in Chapter 3, the variations of the BHM like the extended BHM models support the structured quantum phases. Dipolar atoms interact with via the long-range dipolar interactions, and are suitable candidates to study the structured phases, and the associated novel QPTs. Naturally, the study of the dynamics across these QPTs becomes important and interesting. The condensation of the atoms possessing magnetic dipole moments like the Cr [22, 39, 242, 243], Dy [24, 244] , Er [25, 26] have been important milestones along this direction. Apart from the dipolar atoms, polar molecules featuring electric dipole moments are also routinely used [32–34, 245–247]. To model these systems, the dipolar BHM is used, which has an extra dipole-dipole interaction term in the usual BHM Hamiltonian. The equilibrium quantum phases and the phase diagrams of the dipolar BHM have been extensively studied [68, 79, 81, 84, 248, 249] using various techniques. The general features of the phase diagrams, as studied in Chapter 3 include a density modulated insulating and the supersolid phases, apart from the usual MI and SF phases. As a simplification, the isotropic limit of the dipolar interaction, which physically corresponds to the dipoles polarized perpendicular to the lattice plane, is studied extensively, and the range of the dipolar interaction is cutoff at the nearest neighbouring sites. The resulting model, well known as the eBHM, has been studied to understand the quantum phases exhibited at equilibrium, and also the quench dynamics across the QPTs of the model [230, 241]. The repulsive and isotropic limit of the dipolar interaction results in the checkerboard ordered density wave and supersolid phases. In [84], the quantum phases and the corresponding phase diagrams of the tilted dipolar bosons in 2D square lattice were investigated in detail. As the dipoles are tilted, the dipolar interaction becomes anisotropic, and depends on the polarization angle of the dipoles. In addition to the checkerboard pattern phases, this leads to to stripe pattern in the system. Therefore, the model now features checkerboard and striped structured quantum phases. Note that these two orderings are obtained by the tuning of the polarization of the dipoles, while

the range of the dipolar interaction is truncated to NN. However, there are studies on the $V_1 - V_2$ model, which corresponds to considering the NN (V_1) and next-nearest neighbour NNN (V_2) terms, where the striped ordering is obtained [194]. Motivated by the rich phase diagram of the tilted dipolar model, we study the quench dynamics across different QPTs in this model. Specifically, we study the quantum quench dynamics across the stripe density wave to stripe supersolid, and obtain the KZM scaling exponents. The quenching across this second order QPT complements to that in [230], which considers the quench between checkerboard density wave to checkerboard supersolid phase. After investigating the universality in the dynamics across this QPT, we study the polarization quenching of the dipoles. This leads to the structural QPT from the stripe to checkerboard pattern, and is a first order QPT. We begin the discussions by illustrating the theoretical model employed in our study in the section below.

4.3.1 Theoretical Model

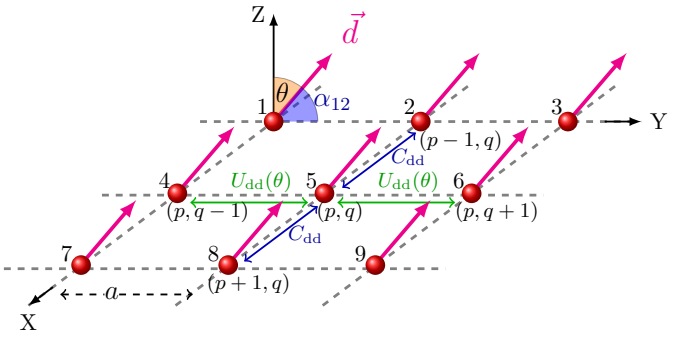

Figure 4.12: The schematic of the dipolar bosons in 2D optical lattice. The lattice is in the x-y plane, and the polarization of the dipoles is in the y-z plane. The angle between the direction of the dipole moment $\vec{d}$ and the z axis is the tilt angle θ, as is illustrated by the orange-shaded color. The dipolar interaction between the nearest neighbouring dipoles along the x direction is represented by $C_{\rm dd}$, while the interaction along the y direction is given by $U_{\rm dd}(\theta)$.

We consider a system of dipolar bosons in 2D optical lattice of square geometry with the lattice constant a. The co-ordinate system is chosen such that the lattice plane constitutes the x-y plane. The schematic of the system of dipolar atoms is shown in

Fig. 4.12. At zero temperature, the physics of the system is well described by the dipolar BHM whose Hamiltonian is [79, 81, 84, 248, 250]

$$\begin{aligned}\hat{H} &= -\sum_{\langle i,j\rangle} J\left(\hat{b}_i^\dagger \hat{b}_j + \text{H.c.}\right) + \sum_i \hat{n}_i\left[\frac{U}{2}(\hat{n}_i - 1) - \mu\right] \\ &+ \frac{C_{\text{dd}}}{2}\sum_{ij}\hat{n}_i\hat{n}_j\frac{(1-3\cos^2\alpha_{ij})}{|\mathbf{r}_i - \mathbf{r}_j|^3},\end{aligned} \tag{4.18}$$

where $i \equiv (p,q)$ represent the lattice indexes, and $j \equiv (p',q')$ are the lattice site indices of its nearest neighbours, $\hat{b}_i^\dagger$ ($\hat{b}_i$) are the creation (annihilation) operators, $\hat{n}_i$ is the bosonic occupation number operator and the summation indexes within $\langle\cdots\rangle$ denote the sum over the nearest neighbours. As is the case for the BHM, J is the nearest neighbour hopping strength, $U > 0$ is the on-site inter-atomic interaction strength, and μ is the chemical potential. The last term in Eq. 4.18 is the dipole-dipole interaction term. The coupling constant $C_{\text{dd}} \propto d^2/a^3$ represents the strength of the dipolar interaction. Here, d is the magnitude of either the permanent magnetic dipole moment, which atoms like Cr, Er and Dy possess, or electric dipole moment that the polar molecules posses. This interaction term in anisotropic, and depends on the angle $\alpha_{i,j}$, which is the angle between the polarization axis and the separation vector $\mathbf{r}_i - \mathbf{r}_j$. In the setup considered in Fig. 4.12, the polarization of the dipoles is in the y-z plane. The angle between the z-axis and the polarization axis is denoted by θ, and is referred to as the tilt angle. The tilt angle can be experimentally controlled by applying an external electric and magnetic field for the electric and magnetic dipoles, respectively. In this work, we consider the atoms with magnetic dipole moment, as these are primarily used in experiments on dipolar BECs [26]. Since the polarization is in the y-z plane, it should be noted that $\theta = \pi/2 - \alpha_{ij}$.

The long range and the anisotropic nature of the dipolar interaction induce various structured quantum phases. These structures are based on the anisotropy of the dipolar interaction, and therefore, in this study, we only retain the anisotropy based θ dependence. We restrict the long range dipolar interaction to the NN sites, for simplicity. This is an optimal model which encapsulates the physics of the long range dipolar interactions of ultracold atoms in a lattice. Then the Hamiltonian is

$$\hat{H} = -\sum_{\langle i,j\rangle} J\left(\hat{b}_i^\dagger \hat{b}_j + \text{H.c.}\right) + \sum_i \hat{n}_i\left[\frac{U}{2}(\hat{n}_i - 1) - \mu\right]$$

$$+\frac{C_{\rm dd}}{2}\sum_{\langle ij\rangle}\hat{n}_i\hat{n}_j(1-3\cos^2\alpha_{ij}). \tag{4.19}$$

For the configuration considered, the dipole-dipole interaction between the dipoles along the x-axis is always repulsive, constant and independent of θ. This is because the angle between these dipoles and the separation vector (which in this case would like along the x-axis) is $\pi/2$, and hence the angular dependent term is zero. However, for the dipoles separated along the y-axis, the interaction is θ dependent and has form $U_{\rm dd}(\theta) = C_{\rm dd}(1-3\sin^2\theta)$. The interaction along the y-axis is repulsive when $\theta < \theta_{\rm M}$, and attractive for $\theta > \theta_{\rm M}$, where $\theta_{\rm M} = \sin^{-1}\left(1/\sqrt{3}\right) \approx 35.3^\circ$, is referred to as the magic angle. At the magic angle, the dipole interaction along the y-axis is zero. In the next subsection, we shall discuss the structures that arise due to the attractive or repulsive dipolar interaction.

4.3.2 Characterization of quantum phases

We solve this model by using the SGMF method and the Gutzwiller ansatz as described previously. The creation and annihilation operators, and the number operator are decomposed into the mean field and a fluctuation operator. Then, the local Hamiltonian takes the following form

$$\hat{h}_{p,q} = \hat{h}^{\rm BHM}_{p,q} + \hat{h}^{x}_{p,q} + \hat{h}^{y}_{p,q}, \tag{4.20}$$

where, the single-site Bose-Hubbard model Hamiltonian is

$$\begin{aligned}\hat{h}^{\rm BHM}_{p,q} &= -J\left[\left(\phi^*_{p+1,q}\hat{b}_{p,q} - \phi^*_{p+1,q}\phi_{p,q} + \phi^*_{p,q+1}\hat{b}_{p,q} - \phi^*_{p,q+1}\phi_{p,q}\right) + \text{H.c.}\right] \\ &\quad +\frac{U}{2}\hat{n}_{p,q}(\hat{n}_{p,q}-1) - \mu_{p,q}\hat{n}_{p,q},\end{aligned} \tag{4.21}$$

the single-site mean field Hamiltonian arising from the long range interaction along x-axis is

$$\hat{h}^{x}_{p,q} = \frac{C_{\rm dd}}{2}\sum_{p'}\left(\langle\hat{n}_{p',q}\rangle\hat{n}_{p,q} - \langle\hat{n}_{p',q}\rangle\langle\hat{n}_{p,q}\rangle\right), \tag{4.22}$$

with $p' = p-1$ and $p+1$. Similarly, for the long range interaction along the y-axis, the single-site mean field Hamiltonian is

$$\hat{h}^{y}_{p,q} = \frac{U_{\rm dd}(\theta)}{2}\sum_{q'}\left(\langle\hat{n}_{p,q'}\rangle\hat{n}_{p,q} - \langle\hat{n}_{p,q'}\rangle\langle\hat{n}_{p,q}\rangle\right), \tag{4.23}$$

with $q' = q - 1$ and $q + 1$. The total mean field Hamiltonian of the system is then

$$\hat{H}^{\mathrm{MF}} = \sum_{p,q} \hat{h}_{p,q}.$$

We use the Gutzwiller ansatz and diagonalize the single-site Hamiltonian $\hat{h}_{p,q}$ self consistently.

To identify the quantum phases of the dipolar BHM, we use different order parameters. The ground state of the standard BHM exhibits two quantum phases: MI phase at low J/U values, and the SF phase at large J/U values. However, the dipolar BHM model can harbour additional phases of the system. The translational symmetry of the system is spontaneously broken by the dipolar interactions. This leads to the structured phases like the DW and the SS phases. These phases have diagonal long-range crystalline order. This means that there is a periodic modulation in the density profile of these phases. The SS phase also displays the ODLRO. That is, there is a simultaneous solidity and superfluidity in the SS phase. Hence, it has non-zero ϕ and periodic modulation of the real valued $\langle \hat{n}_{p,q} \rangle$. To capture the periodic density modulation, the static structure factor is used. This is defined as the Fourier transform of the density-density correlation, given as

$$S(\mathbf{k}) = \frac{1}{N^2} \sum_{i,j} e^{i\mathbf{k}.(\mathbf{r}_i - \mathbf{r}_j)} \langle \hat{n}_i \hat{n}_j \rangle, \tag{4.24}$$

where $\mathbf{k} = k_x \hat{i} + k_y \hat{j}$ is the two-dimensional reciprocal lattice vector, and N is the total number of bosons in the lattice. When $\theta > \theta_M$, anisotropy of the dipolar interaction induces the periodic density modulations along the x-axis only. This is because the interaction along the y-axis is attractive, and the dipoles prefer to be aligned along the y-axis. Hence, the $S(\mathbf{k})$ for $(k_x, k_y) = (\pi, 0)$ is non-zero in the density modulated DW and SS phases. This implies that the translational symmetry is broken along the x direction. These quantum phases have striped pattern, and are referred to as striped density wave SDW (n_A, n_B) and striped supersolid (SSS) phases. Here, n_A and n_B are the occupancies of the two consecutive lattice sites along the x direction. When $\theta < \theta_M$, the dipolar interaction between the dipoles separated along the y axis is repulsive. Then, there is periodic density modulation along both the x and y - directions. The quantum phases have checkerboard order, and are as checkerboard density wave (CBDW) and checkerboard supersolid (CBSS) phases. The checkerboard density mod-

ulation can be captured by the $S(\pi, \pi)$. Table 4.1 summarizes the classification of all the quantum phases exhibited by the dipolar BHM.

Quantum phases	$n_{p,q}$	$\phi_{p,q}$	$S(\pi, 0)$	$S(\pi, \pi)$
Mott insulator (MI)	Integer	0	0	0
Striped Density wave (SDW)	Integer	0	$\neq 0$	0
Striped Supersolid (SSS)	Real	$\neq 0$	$\neq 0$	0
Checkerboard Density wave (CBDW)	Integer	0	0	$\neq 0$
Checkerboard Supersolid (SSS)	Real	$\neq 0$	0	$\neq 0$
Superfluid (SF)	Real	$\neq 0$	0	0

Table 4.1: Classification of quantum phases based on different order parameters.

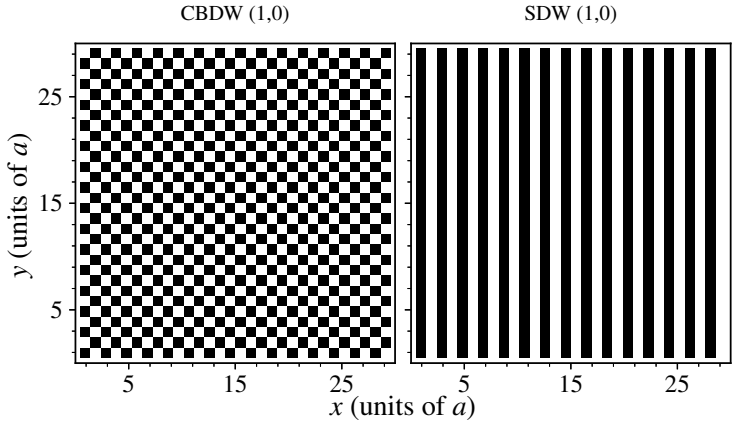

Figure 4.13: Shows the density pattern of the system in distinct density wave phases. Black squares mark those lattice sites which are vacant, and white squares denote singly occupied lattice sites. The states are illustrated for fixed $\mu/U = 0.495$, $C_{\rm dd}/U = 0.8$ and $J/U = 0.033$. The CBDW (1,0) and SDW (1,0) states are obtained for $\theta = 0^\circ$ and 37° respectively.

The checkerboard and stripe density distributions in the structured density wave phase is shown in Fig 4.13. Here the integer pair (n_1, n_2) denote the occupancies of two consecutive lattice sites along x-direction. The density modulation of the CBDW (1,0) is along both the x and y direction. And for the SDW(1,0) phase, the density modulation is only the x-direction. For the parameter domain near the stripe to checkerboard

transition, the dipolar BHM also exhibits the emulsion states, which features regions of both types of density modulations [84]. That is, the checkerboard and stripe pattern coexist in the emulsion states. The density distribution of the checkerboard SS and the striped SS states are similar to the density pattern in Fig 4.13, except that the densities are real number.

We now consider the quantum quench across the SDW(1,0) to SSS phase transition exhibited by the dipolar BHM. This phase transition can be crossed by the varying the hopping amplitude across the critical point of the SDW-SSS transition. We consider $\theta = 40^\circ$ for this study, as this θ value induces the striped pattern, and also avoids the instabilities associated with large θ. As done for the quench across the MI-SF QPT, we consider a system of size 100×100 for this study as well. We investigate the scaling laws, predicted in the KZM, for this second order QPT, and obtain the critical exponents of the correlation length and the topological defects.

4.3.3 Equilibrium phase diagram

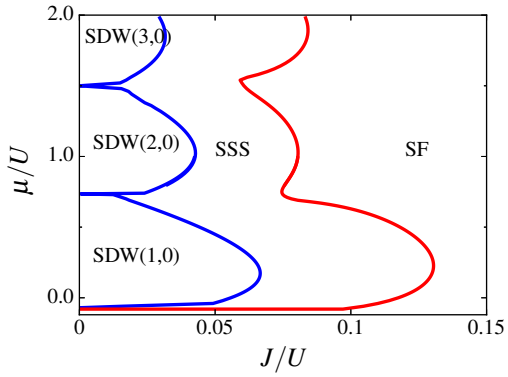

Figure 4.14: Phase diagram of dipolar BHM for $\theta = 40^\circ$ in the $J/U - \mu/U$ plane. The blue line denotes the SDW - SSS phase boundary, while the red line denotes the SSS-SF phase boundary.

The equilibrium phase diagram of the Hamiltonian given by Eq. (4.19) is shown in Fig. 4.14. As mentioned before, we have fixed $\theta = 40^\circ$ in our study. We have used the SGMF method to obtain this phase diagram. At low values of J/U that correspond to strongly interacting domain, the ground state is the insulating SDW phase. The phase diagram comprises of a lobe structure, analogous to the MI lobes, such that each SDW

lobe corresponds to an unique set of densities n_1 and n_2 on the two NN sites along the x-direction. As stated before, the SDW phase is incompressible and thus has $\phi = 0$. As like the MI phase, there is no ODLRO in this phase. However, the SDW phase has periodic density modulation along the x-direction. Thus the $S(\pi, 0)$ equals unity in the SDW(1,0) phase. At large J/U, the system is in the SF phase. This phase has uniform density distribution, and therefore the structure factor $S(\pi, 0) = 0$ in this phase. And, due to the ODLRO in the SF phase, the SF order parameter $\phi \neq 0$. Therefore, there are transition points in the intermediate values of J/U at which the order parameters $S(\pi, 0)$ and ϕ becomes non-zero. Their variation with J/U and $\mu = 0.17U$ is shown in Fig. 4.15. The order parameters are calculated using the equilibrium, or the ground state wavefunctions. We observe a parameter domain of J/U, as illustrated by the grey shaded region in Fig. 4.15, where both these order parameters are non-zero. This region is of the SS phase, as there is simultaneous presence of solidity and superfluidity [43, 84, 249, 251].

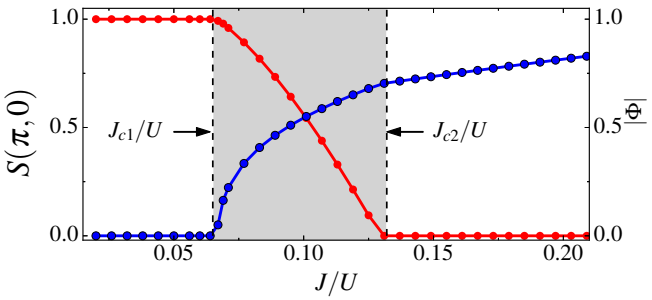

Figure 4.15: $S(\pi, 0)$ (red) and $|\Phi|$ (blue) as a function of J/U, for $\mu/U = 0.17$. The black arrows mark the two transition points J_{c1}/U and J_{c2}/U, for the SDW to SSS and SSS to SF phase transition, respectively.

The SDW-SSS is an incompressible to compressible phase transition, similar to the MI-SF transition. At the tip of the lobe of the SDW(1,0) lobe, which is at $\mu = 0.17U$, the transition belongs to the universality class of the 3D XY model. As mentioned previously, the critical exponents are $\nu = 2/3$ and $z = 1$ for this universality class. And the prediction of the mean-field universality class is $\nu = 1/2$ and $z = 2$.

4.3.4 Transition from SDW to SSS

To study the non-equilibrium SDW-SSS quantum phase transition, we employ the following linear quantum quench protocol

$$J(t) = J_i + \frac{(J_c - J_i)}{\tau_Q}(t + \tau_Q). \tag{4.25}$$

Note that this is similar to the quench protocol employed to study the quench dynamics across the MI-SF transition, given by Eq. (4.12). With this protocol, we have, $J(-\tau_Q) = J_i$ and $J(0) = J_c$. For our study we take $J_i = 0.02U$ and $J_f = 0.11U$, and fix the chemical potential $\mu = 0.17U$. The critical value is $J_c = 0.067U$ for this value of μ. Thus, at $t = -\tau_Q$, the system is in the SDW(1,0) phase, and at $t = t_f$, it is in the SSS phase when the quantum quench ends. The quench protocol employed in our simulations is shown in the Fig. 4.16, for $\tau_Q = 100$. As shown in the figure, once the quench is terminated, we evolve the system freely so that the order parameters attain the steady values.

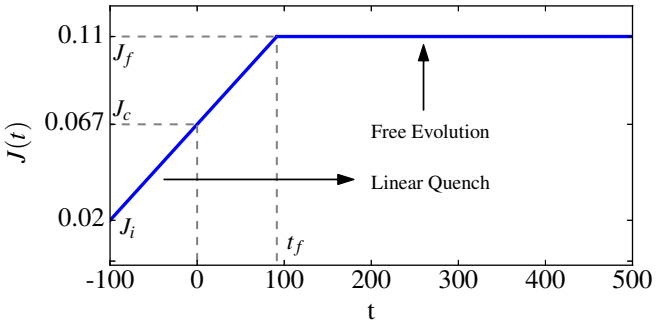

Figure 4.16: A schematic figure to illustrate the quench protocol used in our simulations. The hopping amplitude is ramped up from value J_i to J_c in time τ_Q (here $\tau_Q = 100$). After the quench is terminated at J_f, the system is freely evolved to attain a steady state. The value J_i corresponds to the SDW(1,0) phase, and the value J_f to the SSS phase.

As an initial condition for the time evolution, the equilibrium wavefunction for $J = J_i$ is obtained, and then the density and phase fluctuations are added to it. These fluctuations are introduced following the steps similar to ones described in 4.2.2, for the MI-SF quench dynamics. We have considered 80 such randomized initial states and the physical observables are obtained by averaging over all the 80 samples.

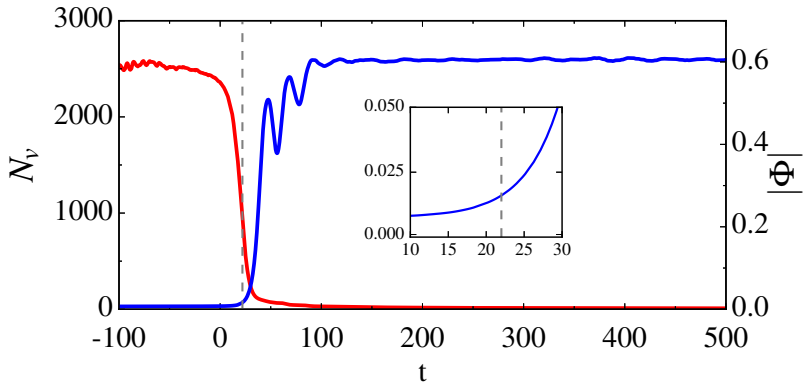

Figure 4.17: The time evolution of $|\Phi|$ (blue) and N_v (red) for $\tau_Q = 100$ is shown in the figure. The inset depicts the behaviour of $|\Phi|$ near $\hat{t}$. The critical point of the phase transition is passed at $t = 0$. The dashed line in (a) indicates the time $\hat{t}$, at which the SF order parameter rises steeply, as illustrated in the inset. As the system enters the SSS phase, there is an annihilation of the vortices and hence, N_v decreases to zero.

$|\Phi|$

We present the dynamical evolution of $|\Phi|$ and N_v during the quench for $\tau_Q = 100$ in Fig. 4.17. The average amplitude of the SF order parameter $|\Phi|$ is of the order $O(10^{-4})$ and stays almost constant when the system passes through the SDW(1,0) parameter domain. This small value is due to the density and phase fluctuations during the initial state preparation. The value of $|\Phi|$ continues to remain small till time $\hat{t}$ where $\hat{t} > 0$. This is because of the delayed response of the system for the symmetry breaking as the system is in the impulse domain. After time $\hat{t}$, the evolution becomes adiabatic, leading to the symmetry breaking and development of the order parameter. An exponential increase in the value of $|\Phi|$ is noticeable after $\hat{t}$. At a later time, a damped oscillatory trend sets in while the average value tend towards the steady state value. The quantum quench is terminated at t_f, after which the $|\Phi|$ stops increasing. During the free evolution followed after t_f, the $|\Phi|$ settles to its steady state value.

To examine the local symmetry broken domains, we present snapshots of $|\phi_{p,q}|$ at certain time instants during the quench dynamics in the Fig. 4.18. These correspond to evolution of one initial state out of the ensemble of 80 states. At the beginning of the quench $t = -\tau_Q$, as discussed earlier and visible in Fig. 4.18(a), $|\phi_{p,q}|$ has small value. The fluctuations though are prominent in the Fig. 4.18 (a). Similar configurations of

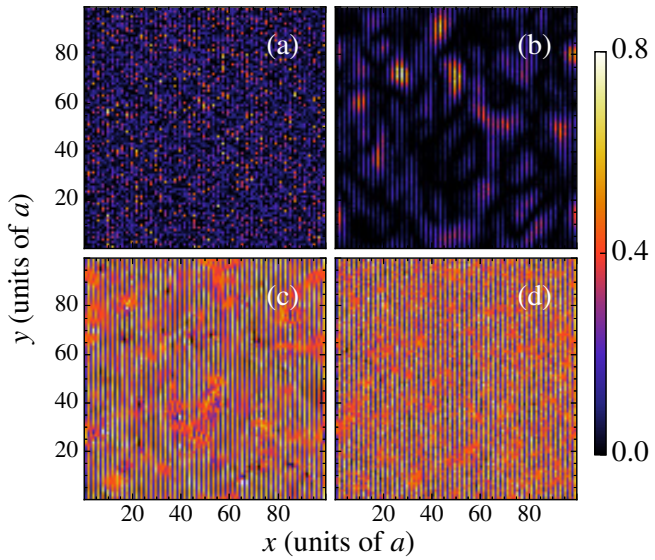

Figure 4.18: Snapshots of $|\phi_{p,q}|$ at certain times for $\tau_Q = 100$. Initially at $t = -\tau_Q$, $|\phi_{p,q}|$ is small as shown in (a). As time progresses, the magnitude of $|\phi_{p,q}|$ increases as shown in (b). Plot (b) is at $t = \hat{t} = 28$. Domains of non-zero $|\phi_{p,q}|$ are formed at this time, and they grow in size, thereby increasing the value of $|\Phi|$. The representative progress of the phase ordering and domain merging can be seen in (c) and (d). Plot (c) is at $t = 92$, while plot (d) is at $t = 400$.

the $|\phi_{p,q}|$ are seen till time $\hat{t}$. After $\hat{t}$, the value of $|\phi_{p,q}|$ is shown in Fig. 4.18 (b). As discussed previously, there are small SSS domains visible as the system exits the impulse domain and re-enters the adiabatic evolution domain. When the J/U is further increased, or for later times, the domains grow in size and phase ordering occurs. In this time period, the domains merge. The representative progress of the phase ordering are shown in Fig. 4.18(c) and (d). Note that the underlying stripe pattern of the two quantum phases - SDW(1,0) and SSS phases, is evident in the time evolution.

N_v

The vortex density N_v is a measure of the vortices present in the system. Similar to the MI-SF QPT, the SDW-SSS transition breaks the global $U(1)$ symmetry spontaneously, in which case the phase of the order parameter acquires a definite value in the SSS phase.The vortex density is very high $N_v \approx 2500$ at the beginning of the quench. This is due to the phase imprinting due to the phase fluctuations added to the initial

wavefunction. It remains of this order till crossing the critical point at $t = 0$. As the system enters the SSS phase, domains of almost uniform phase are formed. That is, there is phase coherence within the domains. However, the two domains need not be correlated. As the time progresses, the system tries to restore the phase coherence via the domain mergers. This is accompanied by the annihilation of the vortex-antivortex pairs, reducing the N_v. And at late times, in the free evolution, the N_v approaches zero, making the system phase coherent. This behaviour is similar to the one exhibited in the quench dynamics across the MI-SF QPT discussed earlier.

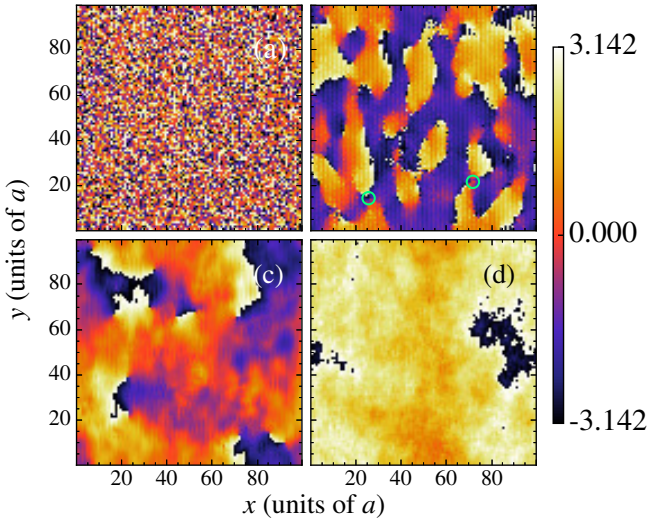

Figure 4.19: Snapshots of the phase of $\phi_{p,q}$ at certain times for $\tau_Q = 100$. Initially at $t = -\tau_Q$, the vortex density is high, as shown in (a), owing to the phase fluctuations imprinted to the system. The domains of uniform phase are formed after the system crosses the critical point, as shown in (b), which is at $t = \hat{t} = 28$. As an illustration of the vortices in the system, we show two of them by the green circles. There is phase ordering process which increases the size of the domains and eventually system retains an almost uniform phase, as shown in (c) and (d). Plot (c) is at $t = 92$ and (d) is at $t = 400$.

The snapshots of the phase of the SF order parameter $\phi_{p,q}$ are shown in Fig. 4.19. The distribution of the phase elucidates the vortices (or antivortices) in the system. The phase fluctuations, and thereby many vortices can be noticed from Fig. 4.19 (a), which is for $t = -\tau_Q$. At time $t = \hat{t}$, after the system exits the impulse domain, we observe SF domains as shown in Fig. 4.19(b). The phase coherence within each of the domains

indicated by the near uniform color. And the points where two or more domains meet illustrate the presence of vortices. The number of vortices or antivortices reduce when the vortex-antivortex annihilation takes place. This also results in the domain mergers, and an increase in the size of the domains, which is the phase ordering process. In plots Fig. 4.19 (c-d), the consolidation of the domain size is prominent. And, at very late times, the system has almost uniform phase.

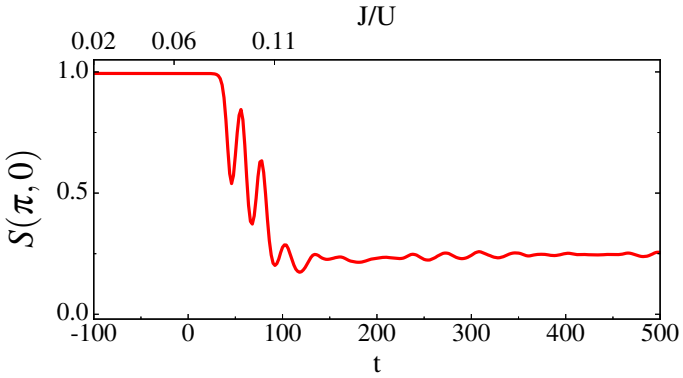

Figure 4.20: $S(\pi, 0)$ as a function of time, for $\tau_Q = 100$. Since the SDW phase has crystalline property, $S(\pi, 0)$ equals unity in this phase. In the SSS phase, the solidity persists, but there is also superfluid character in the system, and $S(\pi, 0)$ deviates from unity. The hopping parameter J/U corresponding to time t is shown on the axis on the top.

We plot the evolution of the structure factor $S(\pi, 0)$ during the quench dynamics in Fig. 4.20. As denoted in Table 4.1, the value of $S(\pi, 0)$ equals unity in the SDW(1,0) phase. Thus, in Fig. 4.20, the $S(\pi, 0)$ equals upto time $t = \hat{t}$. It then deviates from unity, when a few SSS domains are developed in the system. The average value decays as the J/U is increased, and there are large amplitude oscillations visible. Once the quantum quench is terminated and the system is in the free evolution stage, $S(\pi, 0)$ exhibits small amplitude oscillations about the steady state value.

Critical exponents and scaling relations

Next, we study the KZM scaling laws for the SDW(1,0)-SSS QPT. To determine the critical exponents b and d, we do a series of computations over a range of τ_Q. The values of N_v and ξ obtained at time $\hat{t}$ of the corresponding τ_Q are shown in Fig. 4.21(a-b).

The red line is the least square fit to the data points, and the exponents b and d are obtained. They are $b = 0.19$ and $d = 0.41$. We note that these exponents approximately satisfy the KZM scaling relation $d = 2b$. The scaling law of the transition time $\hat{t}$ as a function of τ_Q is shown in Fig. 4.21(c). Using the expressions of b and d in Eq. (4.9) and Eq. (4.10), we obtain $z \approx 2$ and $\nu \approx 1/3$. The exponent z is in good agreement with the mean-field theory prediction ($z = 2$). However, the exponent ν of the equilibrium correlation length differs from the predicted value ($\nu = 1/2$). It is to be noted that previous works [143, 230, 231] employing the Gutzwiller mean-field have also reported such deviations.

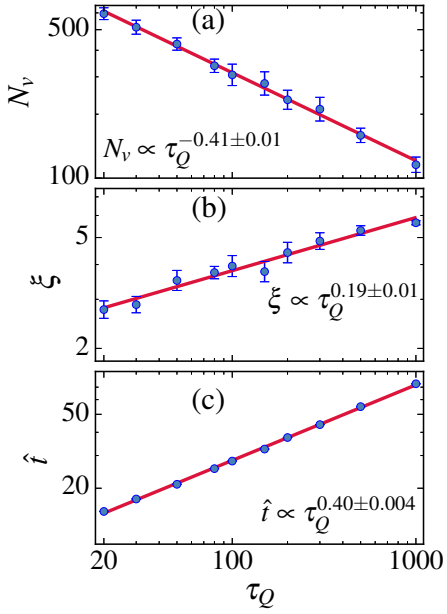

Figure 4.21: Power law scaling of N_v, ξ and $\hat{t}$ with respect to τ_Q. The exponent $d = 0.41$, $b = 0.19$ and the $\hat{t} \propto \tau_Q^{0.40}$. The obtained exponents b and d approximately satisfy the scaling relation $d = 2b$. The blue error bars denote the standard deviation of the data values.

We have also studied the quantum quench dynamics across the SDW(2,0)-SSS QPT, in a similar way by varying the hopping amplitude. The quench protocol is similar to the case of SDW(1,0)-SSS transition. The order parameters evolve in a qualitatively similar way. From the results we get critical exponents as $b = 0.19$, and $d = 0.39$, satisfying the KZM scaling relations.

4.4 Quench dynamics across Stripe Supersolid wave to Checkerboard Supersolid phase transition

After studying the KZ scaling across the continuous QPT, we now consider the possible universal dynamics across a first order QPT. In our system of dipolar gases in optical lattice, a first order structural QPT can be realized by tuning the tilt angle θ. When θ is quenched across the magic angle θ_M in the system, the dipolar interaction along the y-axis changes from repulsive to attractive, which thereby leads to a first order QPT from the striped to checkerboard order. This quenching of the tilt angle θ can be done in experiments by changing the orientation of the external magnetic field [26].

The first order phase transitions are different from the second order phase transitions. They are characterized by the co-existence of multiple phases at the transition point. These transitions exhibit metastability when quenched across the critical point. That is, the evolving state after crossing the critical point remains trapped in the local minimum that corresponds to the metastable state. The evolution towards the ground state, characterized by the global minimum, is hindered due to the potential barrier. The decay of the *false* vacuum state then proceeds by tunneling to the *true* vacuum due to the fluctuations. The potential barrier is overcome beyond the critical point, delaying the transition to the true ground state and making the dynamics non-adiabatic. The decay of the metastable state via the nucleation phenomenon has provided a good theoretical basis to study the dynamics of first-order phase transitions. The nucleation theory involves the rate equations for the dynamics of droplets that cause the decay of metastable state. These droplets of the actual ground state grow in size, governed by these rate equations [252]. Thus the metastability gives rise to the non-adiabatic dynamics across the first order phase transitions. So a natural question to be asked is whether it is possible to find any universal dynamical scaling like the KZ scaling for the first order phase transitions. Motivated by this, we investigate the quench dynamics across a first order phase transition, in the system of dipolar bosons in 2D square lattice.

We study the dynamics of this phase transition from the perspective of investigating the universal scaling laws similar to KZM. There are previous works that have

studied the KZM across the first-order phase transitions. But, not all of them show the power-law scaling of the defect density with the quench rate. In [241], a power law dependence is obtained for the topological vortices across the density wave-to-superfluid transition, while in [253], an exponential saturation of the defects is observed for the dynamics of a quantum search. The works in [254, 255] demonstrate the KZM scalings in spinor condensates. The KZM scalings for the first order classical phase transitions in magnetic systems have been reported [256]. Apart from the KZM, the decay of the false vacuum across the first order QPTs via formation of quantized bubbles has been studied [257, 258]. There have been extensive works on the scaling properties exhibited by the first-order QPTs, and the sensitivity on the boundary conditions by Vicari and co-workers [259–265]. It is thus pertinent to check for the presence of the impulse and adiabatic regimes in the dynamics of striped to checkerboard transition, and the associated power-law scalings.

Equilibrium ground state

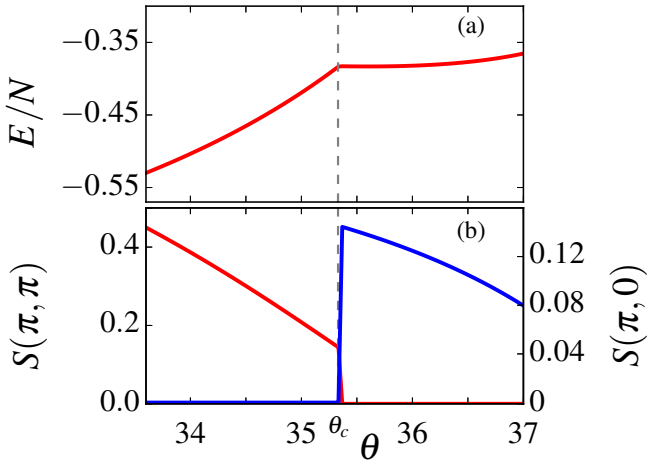

Figure 4.22: (a)Energy per particle of the ground state of the dipolar system as a function of the tilt angle θ. There is a discontinuity in the first derivative of the energy around $\theta_c = 35.3°$. The θ values are denoted in units of degrees. (b) Structure factors $S(\pi, \pi)$ (red) and $S(\pi, 0)$ (blue) as a function of the tilt angle θ. Both the quantities show a discontinuous jump at θ_c.

The system parameters are fixed as $J = 0.05U$ and $\mu = 0.75U$. At these fixed parameter values, there is a parameter domain for the tilt angle θ whereby the SSS-

CBSS transition can be probed [84]. The corresponding critical tilt angle θ_c is 35.3°. To examine the order of the phase transition, we study the equilibrium ground state energy per particle E/N as a function of θ. In particular, the kink in the energy per particle E/N of the ground state at the θ_c, as shown in Fig. 4.22(a), indicates a first order quantum phase transition. For $\theta > \theta_c$, the system has striped order along the y-axis. While for $\theta < \theta_c$, there is checkerboard ordering in the system. These two orders are discernible from the structure factors $S(\pi, \pi)$ and $S(\pi, 0)$. As shown in Fig. 4.22(b), $S(\pi, \pi)$ and $S(\pi, 0)$ are non-zero for the phases with checkerboard and striped order, respectively. In the neighbourhood of θ_M, the converged solutions are sensitive to the initial state. In this parameter domain, the common ground state solution is a metastable emulsion phase, that exhibits a superposition of the checkerboard and striped orders [84, 249]. The density distribution of such an emulsion density wave phase is shown in Fig. 4.23, exhibiting simultaneous existence of the two orders. So, to identify the equilibrium ground state, we use different initial states and consider the converged solution with the lowest energy as the ground state.

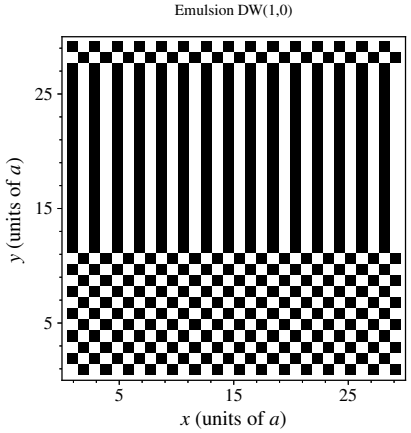

Figure 4.23: The density pattern in the emulsion density wave phase. This phase exhibits a simultaneous existence of the checkerboard and striped orders.

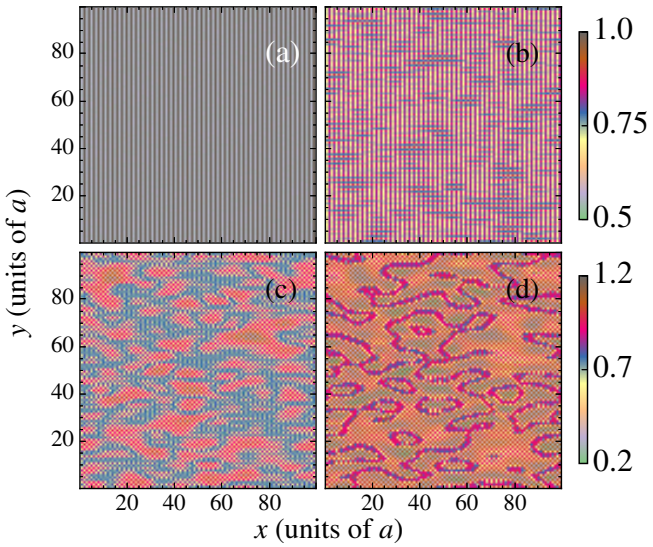

Figure 4.24: Snapshots of the density at certain times in the time evolution across SSS-CBSS transition, for $\tau_Q = 20$. The subplot (a) corresponds to the initial state at time $t = -\tau_Q$, (b) corresponds to the state at time $\hat{t} = 44$, (c) denotes the density profile at $t = 50$, and (d) corresponds to the density profile at the end of the quench. We observe domains of checkerboard order emerging at $\hat{t}$. The density ordering can be noticed from subplots (b)-(d) in the figure.

SSS-CBSS quench dynamics

After establishing the order of the SSS-CBSS transition, we shall now discuss the quench dynamics across it. The quench protocol employed in our studies is

$$\theta(t) = \theta_i - \frac{(\theta_i - \theta_c)}{\tau_Q}(t + \tau_Q). \tag{4.26}$$

As mentioned earlier, we consider $J = 0.05U$, and $\mu = 0.75U$ for the quench dynamics. Using the above linear quenching protocol, we have $\theta(-\tau_Q) = \theta_i$, and $\theta(0) = \theta_c$. That is, from $t = -\tau_Q$ to $t = 0$, the θ changes from θ_i to θ_c. The simulations are performed with $\theta_i = 37^\circ$ and $\theta_f = 32^\circ$ for different quench times τ_Q. The choice of these parameters are based on the ground state phase diagram of the model Hamiltonian of the system [84]. Similar to the J quenching across SDW-SSS transition, the quantum fluctuations essential to initiate quantum phase transition are incorporated through the addition of noise to the coefficients in the Gutzwiller wave function. The role of the quantum fluctuations becomes very important as we have verified that the phase transition occurs only when the initial fluctuations are seeded.

To illustrate the development of the checkerboard order in the system in the dynamics, we show the density profiles at different stages of the evolution in Fig. 4.24. At the start of the quench ($t = -\tau_Q$), the density has striped order as can be seen in Fig. 4.24 (a). The striped order is, then, altered after the system crosses the critical tilt angle θ_c. The resulting density deformations emerge as patches of checkerboard domains and the system appears like shown in Fig. 4.24(b). We shall later investigate the number of such domains formed when quenched with different rates. These domains grow in size and the density ordering progresses. At late times, there are large domains of checkerboard order separated by a "network" of remnant striped order as seen in Fig. 4.24(d).

Scaling of $\hat{t}$

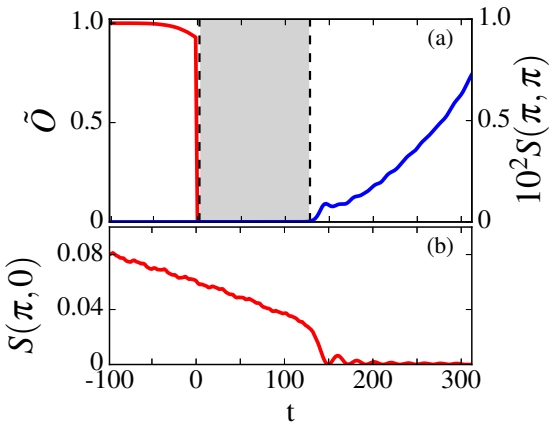

Figure 4.25: Overlap $\tilde{O}$ between the ground state and the dynamically evolved state, and the structure factor $S(\pi, \pi)$ as a function of time is shown in (a). The grey shaded region denotes the non-adiabatic domain in the dynamics. The time instant $\hat{t}$, which marks the end of this domain, is when the $S(\pi, \pi)$ becomes non-zero. In (b), we show the $S(\pi, 0)$ as a function of time. There is a decreasing trend in the $S(\pi, 0)$, and near $\hat{t}$, the decay is steeper.

We use the overlap $\tilde{O}$ as an indicator of the adiabaticity in the quench dynamics, thus identifying the adiabatic and non-adiabatic domains. It is the overlap of the quenched state with the equilibrium ground state having same θ value. The trend of $\tilde{O}(t)$ is as shown in the Fig. 4.25(a) with the red colored plot. At initial times, the overlap is close to the unit value, signifying the adiabatic evolution. Due to the growing

fluctuations, as the quench progresses, it deviates from unity, and becomes zero at a particular time. This then marks the beginning of the non-adiabatic domain. This non-adiabatic domain is akin to the impulse domain encountered in the dynamics across continuous phase transitions, due to the critical slowing down. We refer it as impulse-like domain. The ground state of the system for $\theta < \theta_c$ has a checkerboard ordering and does not show good fidelity with the quenched state. The time instant when the overlap becomes zero depends on the quench rate, but it is located near θ_c. After the system leaves the impulse-like domain, it can be expected that $\tilde{O}$ becomes non-zero, as the dynamics becomes adiabatic. However, the state is populated with topological defects. And, thus this state does not show good fidelity with the corresponding equilibrium ground state. So, $\tilde{O}(t)$ is not a good indicator of the adiabatic domain following the impulse-like domain.

To indicate the end of the impulse-like domain, the structure factor $S(\pi, \pi)$ is a good order parameter. Its trend with time is as shown by the blue color plot in the Fig. 4.25(a). The $S(\pi, \pi)$ is zero in the SSS phase, but finite in the CBSS phase. Thus, the emergence of the checkerboard order is signalled when $S(\pi, \pi)$ becomes non-zero. This also means the end of the non-adiabatic domain in the dynamics. In analogy with the J quenching, we mark this time instant as $\hat{t}$. Thus the impulse-like domain in the dynamics persists from around $t = 0$ to $t = \hat{t}$, as indicated by the grey shaded region. In other words, there is a time delay in the emergence of the checkerboard order after crossing θ_c. This delay implies the extent of the non-adiabaticity in the quench dynamics. We now investigate the scaling of the $\hat{t}$ for different quench rates. The behaviour of $\hat{t}$ with τ_Q is shown in the Fig. 4.26(a). The plot shows the power-law nature of $\hat{t}$ with τ_Q, and the corresponding critical exponent is 0.70. That is, for the SSS-CBSS quantum phase transition $\hat{t} \propto \tau_Q^{0.70}$. As the quench dynamics progresses, the $S(\pi, 0)$ decreases and this trend is discernible from the plot in the Fig. 4.25(b). This trend continues after crossing the θ_c at $t = 0$, and it arises from the density fluctuations present in the impulse domain. Thus the non-adiabatic domain does not correspond to the frozen state in the dynamics, as is the case assumed in the KZM. So even though the system displays a striped pattern in the impulse-like domain, the fluctuations continue to evolve, causing local density changes, thereby changing the $S(\pi, 0)$. After crossing

the critical point, the striped ordered state is a metastable state and the evolving state remains close to this metastable state. In this regard, the dynamics across the continuous phase transitions is different than the first order phase transitions. Once the $\hat{t}$ is crossed, the $S(\pi, 0)$ has a steeper decrease, as the system enters the adiabatic domain. It becomes zero after some characteristic oscillations as the checkerboard order sets in as the ground state. Another point to note is that there is a finite time interval after $\hat{t}$, where both the $S(\pi, 0)$ and $S(\pi, \pi)$ are non-zero. That is, post $\hat{t}$, there are domains of checkerboard order with the striped order as the background, it resembles the emulsion phase [84]. However, as the quench progresses further, the striped pattern diminishes, and the $S(\pi, 0)$ becomes zero.

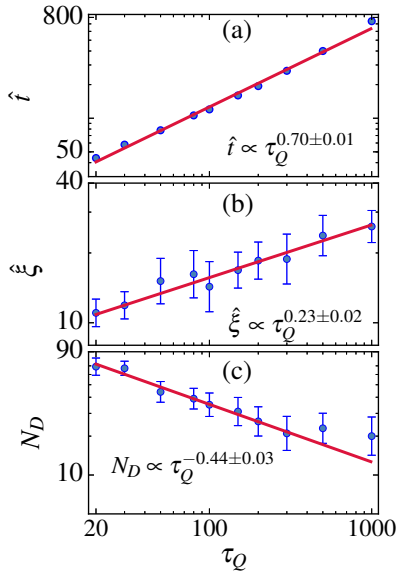

Figure 4.26: Scaling of $\hat{t}$, $\hat{\xi}$ and N_D with τ_Q, for the SSS-to-CBSS phase transition. The power-law scaling of $\hat{t}$ is discernible in (a), and the exponent is 0.70. In (b), the scaling of $\hat{\xi}$ is presented and the exponent is $b = 0.23$. The power-law scaling of N_D is shown in (c), and the exponent is $d = 0.44$. Note that the scaling exponents b and d satisfy the scaling relation $d = 2b$.

Scaling of the number of domains and correlation length

A key result of KZM is scaling of the defect density with the quench rate, as stated in Eq. 4.10. The domains of the uniform order parameter are because of the local spontaneous symmetry breaking, and this number also exhibits a scaling relation with τ_Q.

The SSS-CBSS transition is a density driven transition between the quantum phases of different density orders. Therefore, the vortex density N_v is not the correct measure to indicate the defects produced across this transition. In other words, for the SSS-CBSS transition, defects are not vortices. Then, as a measure of the extent of symmetry broken across the SSS-CBSS transition, we consider the number of domains N_D of the checkerboard order. We study the scaling relation of N_D with τ_Q. As a first step, a scheme to differentiate the SSS and CBSS domains is required. For that, we introduce the density contrast order parameter at the (i, j) lattice site as

$$N_{i,j} = \frac{1}{2}\left(\left|\langle\hat{n}_{i,j}\rangle - \langle\hat{n}_{i,j+1}\rangle\right| + \left|\langle\hat{n}_{i+1,j}\rangle - \langle\hat{n}_{i+1,j+1}\right|\right). \tag{4.27}$$

The value of this order parameter is ideally $(n_A - n_B)$ and 0 for the checkerboard and striped order, respectively. Hence it serves to contrast between the two ordered phases, and classify the site (i, j) in a checkerboard or striped domain. In the quenched dynamics, the $N_{i,j}$ has a range of values, as shown in Fig. 4.27(a). Then, a threshold value

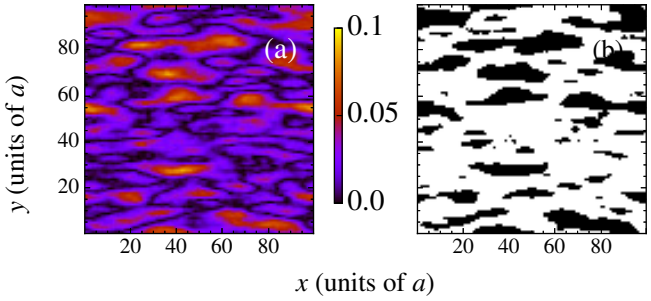

Figure 4.27: (a) Plot of the density contrast order parameter $N_{i,j}$. The regions with the values of this order parameter smaller than a threshold value correspond to the striped phase, while those with larger values denote the domains of checkerboard order that are formed in the time dynamics. (b) The plot of the distribution of the binary values 0 and -1, obtained after applying the threshold to the plot (a). The black colored domains indicate those of label 0, while the white regions indicate the domains of label -1. The domains of the label 0 are counted numerically.

ϵ of $N_{i,j}$ is used to differentiate between the checkerboard and striped domains. This threshold is obtained by considering the value of $N_{i,j}$ over the prominent SSS regions in the system. Based on this definition, we obtain $\epsilon = 0.04$ in our computations. So the sites where $N_{i,j} > \epsilon$ are considered in CBSS phase and those with lower value in SSS

phase. The lattice sites are, then, labeled as 0 and -1 for the CBSS and SSS phases, respectively. Thus we have a lattice with sites labeled with 0 and -1, as can be seen in Fig. 4.27(b). Now the task is to count the number of domains of label 0. For this, we use the methods in percolation analysis [173, 266], and use the domain counting method outlined in chapter-2. As a check , we calculate the N_D for the SDW(1,0)-SSS phase transition. And, we obtain the critical exponent $d = 0.37$, which is in good agreement with the value $d = 0.41$ obtained from the scaling of N_v as shown earlier in the Fig. 4.21. Then for the SSS-CBSS transition, the scaling of N_D at $\hat{t}$ with τ_Q is presented in Fig. 4.26 (c). We obtain a power-law scaling with the quench rate, as expected from the KZM. The critical exponent is 0.44.

Next we compute the average linear size of the domains. This can also be thought of as the correlation length of the system, highlighting the size of the correlated checkerboard domains formed. We again use the percolation methods to compute the percolation correlation length, ξ. This correlation length is based on the geometrical properties of the domains of the checkerboard order, and is defined as an average over the radii of the domains in the system:

$$\xi^2 = \frac{\sum_s R_s^2 s^2 n_s}{\sum_s s^2 n_s}, \tag{4.28}$$

where R_s is the gyration radius of the cluster of s sites, and the n_s denotes the average number of clusters of size s per site. In the summation, the contribution from the infinite, percolating clusters is omitted [167, 168]. The scaling of this correlation length at time $\hat{t}$ with the quench time τ_Q is shown in Fig. 4.26 (b). The power-law scaling exponent obtained is 0.23. An important point to be noted is that the scaling exponents of ξ and N_D obtained satisfy the scaling relation $d = 2b$, similar to the case for the SDW-SSS second order quantum phase transition. Note that we have used the percolation correlation length for the analysis. The correlation length "extracted" from the two-point correlation function $\langle \hat{b}_i^\dagger \hat{b}_j \rangle$ is an improper choice for this phase transition, as the SF order parameter ϕ is non-zero in both SSS and CBSS quantum phases. The correlation length obtained by this method is a constant as a function of τ_Q.

Thus, the quantum phase transition from the striped supersolid to checkerboard supersolid phase exhibits the universal scaling relations with the quench rate. The

scaling exponents obtained satisfy the scaling relations. Using the expressions of the power-law scalings, we obtain the critical exponents $\nu \approx 1$ and $z \approx 3$ for the SSS-CBSS phase transition.

4.5 Summary of the chapter

In this chapter, we have studied the quench dynamics and the associated KZ scaling laws across some QPTs exhibited by the ultracold atoms. In particular, we have studied the dynamics across the MI-SF quantum phase transition, and have investigated the KZ scaling relations and the critical exponents. We have analysed both the defect density, and the number of domains formed, and have seen the consistency in the scaling behaviour of these two quantities. For the dipolar bosons in the optical lattice, we have studied the quenching of the hopping amplitude across the SDW(1,0)-SSS transition, and have reported the KZ scaling laws. Specifically, we obtain the power-law scaling of the vortex density, and the correlation length of the system, at time instant $\hat{t}$. The critical exponents b and d obtained by quenching across MI-SF and SDW-SS transition both obey the scaling relation $d = 2b$. Then, the structural first-order quantum phase transition from the striped to the checkerboard supersolid phase is studied by quenching the tilt angle θ. There is a non-adiabatic domain in this transition owing to the metastability of the evolving state across the critical point. The duration of this non-adiabatic domain, or the time $\hat{t}$ obeys a power-law scaling with the quench rate, quite similar to the classic KZM. Motivated by this, we further compute the percolation correlation length and the number of domains of the checkerboard order and obtain their power-law scaling with the quench rate, as is expected in the KZM. These findings suggest the description of the dynamics of first order QPT with the KZM-like physics.

Chapter 5

Percolation analysis of BG-to-SF transition

Disorder has profound importance in understanding the properties of materials theoretically and experimentally. Most of the condensed matter systems inevitably possess impurities like vacancies and extended defects. Therefore the consideration of its effects on the material properties becomes important. For instance, the Anderson localization [267] for non-interacting systems and many-body localization [202] for interacting systems are due to the effects of the disorder. The interplay between the disorder and interactions among the constituent particles lie at the heart of the rich physics exhibited by the disordered quantum systems. This interplay results in the novel low-temperature glassy phases that are obtained only in the presence of the disorder. The study of transport properties of disordered solids and the associated universality classes of the metal-insulator transitions have been extensively studied. The transition in the nature of states at the Fermi energy from extended to localized is the reason behind the metal-insulator transition [268]. The strong interactions lead to insulating quantum phases, for instance, the Mott Insulator. The presence of disorder imparts an insulating nature, as the wavefunctions in disordered systems are localized. Thus, the combined effects of interactions and disorder on the QPTs are important to study. This study is posed with several questions [269–272]: Does the QPT remains sharp or becomes smeared due to the disorder? Do (and if yes, how) the critical exponents change? Are the bulk phases obtained in the clean counterpart stable?

The effect of the disorder on the bosons in lattices has gained importance following the work by Fisher *et al* [19]. It was shown that the direct Mott Insulator-to-superfluid transition is prohibited in disordered lattice potential, as the novel Bose glass (BG) phase intervenes the two. The BG phase is characterized by finite compressibility yet is an insulating phase. It can be understood as the Griffiths phase of the superfluid-insulator transition. That is, in the BG phase, the rare large regions of the superfluid order coexist with the bulk insulating phase. These SF islands are responsible for the finite compressibility of the BG phase. However, they do not generate a phase coherence across the system. In the SF phase, however, there is phase coherence throughout the system. Such an establishment of the phase coherence occurs as the SF islands grow in size and merge to become a single island. Therefore, the BG-to-SF transition can be studied using the percolation theory. In the BG phase, the SF islands are non-percolating; and in the SF phase, these islands percolate.

In this chapter, we shall study the percolation analysis of the SF clusters in the BG phase. We wish to understand the critical properties of the BG-to-SF transition in a 2D square optical lattice. We begin by discussing the disordered Bose-Hubbard model (DBHM) apt to model the physics of disordered bosons in lattices. We then present the percolation analysis of the SF clusters in the BG phase for increasing values of the hopping amplitude across the critical value of the BG-SF transition. We compute the correlation length of the system and demonstrate its divergence near the critical point of the BG-to-SF transition. These calculations are done employing the fine-grained method that we have developed for the percolation analysis using linked-lists, as discussed in Chapter 2. We calculate the critical exponent ν characterizing the critical divergence and find it belongs to the 2D percolation universality class. The trend of the superfluid stiffness further strengthens our results as it shows an increase near the critical point obtained via the percolation analysis. Here we mention that there are previous works [273, 274] that study the geometric properties of the SF clusters in the BG phase. In our study, however, we have explicitly computed the correlation length based on the size of the clusters and supported the percolation results with the computations of the superfluid stiffness.

5.1 Disordered Bose-Hubbard model

5.1.1 Theory

The DBHM for a square lattice with nearest neighbour hopping is defined by the Hamiltonian [19, 105, 275–277]

$$\begin{aligned}\hat{H} &= -\sum_{p,q}\left[J_x\left(\hat{b}^{\dagger}_{p+1,q}\hat{b}_{p,q}+\text{H.c.}\right)+J_y\left(\hat{b}^{\dagger}_{p,q+1}\hat{b}_{p,q}+\text{H.c.}\right)\right]\\ &\quad+\sum_{p,q}\hat{n}_{p,q}\left[\frac{U}{2}(\hat{n}_{p,q}-1)-\tilde{\mu}_{p,q}\right].\end{aligned} \tag{5.1}$$

where p (q) is the lattice index along x (y) axis, J_x (J_y) is the hopping strength between two nearest neighbour sites along x (y) axis, $U > 0$ is the on-site inter-atomic interaction strength, and $\tilde{\mu}_{p,q} = \mu - \epsilon_{p,q}$ is the local chemical potential. The disorder is introduced through the random energy offset $\epsilon_{p,q}$ which is a univariate random number in the range $[-\Delta, \Delta]$, where Δ denotes the strength of the disorder. The offset $\epsilon_{p,q}$ modifies the diagonal term in the Hamiltonian, and so such a disorder is called the diagonal disorder. On the contrary, randomness can also be introduced in the off-diagonal terms, for instance in the hopping strength J_x (or J_y), which is then referred as the off-diagonal disorder [278–281]. For the off-diagonal disorder, the phase diagram becomes richer, and an additional Mott-glass (MG) phase is obtained. Disorder can also be introduced in the interparticle interaction U by manipulating the Feshbach resonance [282–284].

The study of the superfluid helium adsorbed on porous media motivated the study of the disorder and interactions among the bosons in lattices [285, 286]. Cold atoms in optical lattices constitute relatively recent and efficient systems to study the effects of disorder on the atoms in lattices. In these systems, the DBHM is realized by considering a disordered lattice potential generated by shining speckle beam [137, 287–289], using non-commensurate lattice potentials [290, 291], or using distinguishable, randomly distributed atom species [30, 292]. These controlled ways of introducing the disorder make these systems efficient for studying the effects of the disorder, contrary to the condensed matter systems. The experimental measurements on the BF-SF transition have been reported [137, 291, 293–295].

We make a note that the disorder that we consider in our studies is quenched disorder, which is a static or frozen-in disorder, whereby the impurities do not move or change over the system timescales. Therefore, every disorder realization is different in the case of quenched disorder, and the physical quantities need to be ensemble averaged over the disorder realizations. To obtain reliable statistics, it is essential to consider a large number of disorder realizations and large system sizes to eliminate the finite-size effects.

5.1.2 Quantum phases of DBHM

The ground state phase diagram of the DBHM is extensively studied using various techniques: the mean-field method [296], stochastic mean-field theory [277, 297, 298], Gutzwiller technique [156, 157], the QMC [278, 282, 299–301], strong coupling expansion [302], density matrix renormalization group (DMRG) for one-dimensional systems [303–305]. The ground state phase diagram of the DBHM exhibits the quantum phases determined by the competition between the hopping energy J, the interaction energy U and the disorder strength Δ. For a moderate Δ and small J/U, the strong on-site repulsion favours the incompressible MI phase. As discussed before, the system has integer commensurate filling in the MI phase and the number fluctuations are suppressed. For large J/U, the strong hopping overcomes the on-site repulsion and the system favours the compressible SF phase. The atoms possess itinerant property and the number fluctuations are present in the SF phase. There is a long-range phase coherence in the system. In the intermediate J/U, the two phases are separated by the BG phase. The BG phase structurally has the SF islands inlaid in the background insulating MI phase. This is an insulating yet compressible glassy phase obtained solely due to the finite disorder in the system. As discussed in [306], the BG phase is characterized by complex energy landscapes with many metastable minima. This results in the long relaxational times, as is a signature of the glassy systems, hence the name Bose Glass phase. The different metastable configurations in the BG phase differs in the phase alignment of the SF islands in the BG phase. That is, in an island, the phase of the SF order parameter is uniform, but differs across the SF islands. Therefore, such an existence of metastable states is considered the reason for the glassy feature of the

BG phase.

The MI and SF phases of the clean BHM are distinguished using the SF order parameter ϕ. As discussed earlier, the ϕ is zero in the MI phase and is non-zero in the SF phase. Apart from the SF order parameter, the number fluctuation $\delta n_{p,q}$ at a lattice site can be used to distinguish the MI and the SF phase. With the inclusion of the disorder, the MI to BG phase transition can be identified using the number fluctuations or the SF order parameter ϕ. The number fluctuations are finite in the BG phase owing to the SF islands, while they are negligibly small in the number coherent MI phase. Also, due to the SF islands, $\phi \neq 0$. To demarcate the BG-SF phase boundary, the SF stiffness ρ_s is used. The SF phase exhibits phase coherence. In other words, a finite amount of energy is required to alter the phase coherence or to change the phase. This property is utilized in the superfluid stiffness ρ_s. Twisted boundary conditions (TBC) are imposed on the state to compute the ρ_s. The twisted boundary condition for the wavefunction is defined as [307]

$$\Psi(x_1, x_2, \ldots x_i + N_x, \ldots) = e^{i\varphi}\Psi(x_1, x_2, \ldots x_i, \ldots), \tag{5.2}$$

where the $\{x_i\}$ are the co-ordinates of the wavefunction and N_x is the size of the system. If the TBC is applied along the x direction, the hopping term in the DBHM is transformed as

$$J_x(\hat{b}^\dagger_{p+1,q}\hat{b}_{p,q} + \text{H.c}) \rightarrow J_x(\hat{b}^\dagger_{p+1,q}\hat{b}_{p,q}e^{i2\pi\varphi/L} + \text{H.c}), \tag{5.3}$$

where, φ is the phase shift or twist applied to the PBC, L is the size of the lattice along x direction, and $2\pi\varphi/L$ is phase shift of an atom when it hops between nearest neighbours. Accordingly, ρ_s is computed employing the following expression [305, 307]

$$\rho_s = \frac{L}{8\pi^2}\frac{\partial^2 E_0}{\partial\varphi^2}\bigg|_{\varphi=0}, \tag{5.4}$$

where E_0 is the ground state energy with twisted boundary condition. In the BG phase, due to the absence of a global phase coherence, $\rho_s = 0$ while in SF phase, $\rho_s \neq 0$. We summarize the different quantum phases and their characterization using order parameters in Table. 5.1.

Quantum phase	ρ_s	$\delta n_{p,q}$	ϕ
Superfluid (SF)	$\neq 0$	$\neq 0$	$\neq 0$
Mott insulator (MI)	0	0	0
Bose glass (BG)	0	$\neq 0$	$\neq 0$

Table 5.1: Classification of quantum phases and the order parameters supported by DBHM at zero temperature.

5.1.3 Single site Gutzwiller mean field for DBHM

We use the SGMF theory to obtain the ground state of the DBHM. The details of this method were introduced in Chapter 2. After decomposing the creation and annihilation operators into a mean field and fluctuation operator, the DBHM Hamiltonian given in Eq. (5.1) reduces to the mean-field Hamiltonian which is a sum of single site Hamiltonians $\hat{H}_{\text{MF}} = \sum_{p,q} \hat{h}_{p,q}$. The single-site Hamiltonian $\hat{h}_{p,q}$ is given as

$$\begin{aligned}
\hat{h}_{p,q} &= -J_x\left[\left(\hat{b}^{\dagger}_{p+1,q}\phi_{p,q} + \phi^{*}_{p+1,q}\hat{b}_{p,q} - \phi^{*}_{p+1,q}\phi_{p,q}\right) + \text{H.c.}\right] \\
&\quad -J_y\left[\left(\hat{b}^{\dagger}_{p,q+1}\phi_{p,q} + \phi^{*}_{p,q+1}\hat{b}_{p,q} - \phi^{*}_{p,q+1}\phi_{p,q}\right) + \text{H.c.}\right] \\
&\quad +\left[\frac{U}{2}\hat{n}_{p,q}(\hat{n}_{p,q}-1) - \tilde{\mu}_{p,q}\hat{n}_{p,q}\right],
\end{aligned} \tag{5.5}$$

To obtain the ground state of the system, the site dependent Gutzwiller ansatz is used. The phase diagram computed using the SGMF method for $\Delta = 1.2U$ shown in Fig. 5.1, and consists of the BG and SF phases.

The absence of the MI phase is due to the high disorder strength. For the further computations, we fix $\mu = 0.2U$ and scan the quantum phases as a function of J/U. The snapshots of $|\phi_{p,q}|$ for selected values of J/U are shown in Fig. 5.2, for a 100×100 system. In the figure, the rare SF islands in the BG phase are noticeable in Fig.5.2(a) which is for $J/U = 0.009$. These SF islands increase in size as the J/U is increased. This can be seen in Fig. 5.2 (b) which shows $|\phi_{p,q}|$ for $J/U = 0.015$. The SF islands though large, are non-percolating, and hence, introducing a phase twist does not cost energy. On reaching critical J/U, a spanning cluster emerges, and the system undergoes percolation transition. This is illustrated in the Fig. 5.2(c), the system supports a

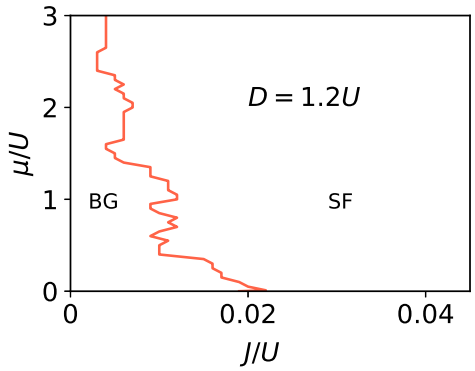

Figure 5.1: Phase diagram of DBHM with SGMF method for disorder strength $\Delta = 1.2U$, in the $J/U - \mu/U$ plane. The BG phase is obtained in the strongly interacting limit, that is, at low J/U value. The SF phase is obtained for large values of J/U. The two quantum phases are distinguished by the stiffness ρ_s averaged over 500 disorder realizations. Reprinted figure from [Sukla *et* al., PRA, **99**, 053610 (2018).] Copyright © 2018, American Physical Society.

spanning cluster for $J/U = 0.019$. Due to the spanning SF cluster, introducing a phase twist costs energy, and superfluid stiffness ρ_s assumes a finite value. Upon further increase of J/U, the background MI phase region is completely depleted and the entire system is in the SF phase. This is discernible from the Fig. 5.2 (d).

5.2 Percolation theory

Based on the previous discussions, the BG-to-SF transition can be studied by using the percolation theory. The percolation theory analyses the statistical and geometrical properties of the clusters of sites on a lattice [167]. An essential feature of the percolation systems is their universal properties near the percolation transition point p_c. The percolation transitions exhibit critical phenomena similar to those encountered for the continuous thermal and quantum phase transitions. The different percolation quantities, related to the size of the clusters, follow a power-law scaling as a function of the reduced distance from the p_c. One such property which exhibits a power-law divergence at the transition is the correlation length of the system ξ. It is defined as an

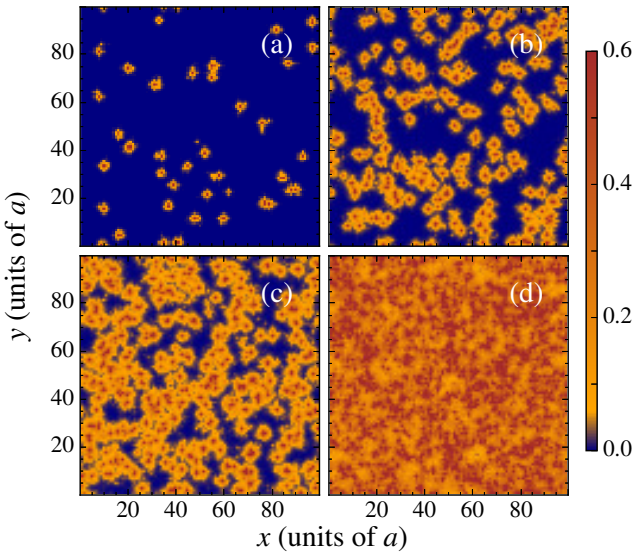

Figure 5.2: Snapshots of $|\phi_{p,q}|$ at different J/U values. Panels (a)-(d) correspond to the J/U values as 0.009, 0.015, 0.019 and 0.025 respectively. As the J/U is increased, the SF domains percolate and the system undergoes a transition from BG to SF phase. Here $J_c \approx 0.017U$ for the system parameters $\mu = 0.2U$ and $\Delta = 1.2U$ considered in the computations.

average over the cluster radii in the system

$$\xi^2 = \frac{\sum_s R_s^2 s^2 n_s}{\sum_s s^2 n_s}, \tag{5.6}$$

where R_s is the gyration radius of the cluster of s sites, and the n_s denotes the average number of clusters of size s per site. In the summation, the contribution from the infinite, percolating clusters is omitted [167, 168]. At the percolation transition ξ shows power-law divergence

$$\xi \propto |p - p_c|^{-\nu} \tag{5.7}$$

where ν is the corresponding critical exponent. The radius of gyration of a cluster is defined as the root mean-square distance r_i of the constituting cluster sites from the center of mass of the cluster r_c

$$R_s^2 = \left\langle \frac{\sum_i (r_i - r_c)^2}{s} \right\rangle. \tag{5.8}$$

As the Eq. (5.8) implies, the calculation of R_s requires the distance of a lattice site from the center of mass of the cluster. For systems with the PBC, there are two possible

definitions of the distance between two lattice sites, owing to the absence of edges. Therefore, to resolve this shortcoming in a consistent way, we unwrap the system. After this is done, the clusters in the original system are mapped onto a larger system with double dimensions. The distance between the lattice sites in a cluster is defined without ambiguity in the larger system. We have outlined the steps of this procedure in the Appendix D. The fine-grained approach of our method using paths, introduced in Section 2.4.3, helps in evaluating the geometric properties of the SF clusters.

In the following, we demonstrate the divergence of the correlation length near the BG-SF transition. In the BG phase, the sites with non-zero SF order parameter are considered occupied. A threshold of 10^{-3} is imposed on the SF order parameter to identify the occupied sites. Thus, the sites with SF order parameter greater than 10^{-3} are the sites of the SF region and the remaining sites constitute the MI phase. We expect the SF clusters to percolate as the critical J_c of the BG-to-SF transition is approached. Therefore, the power-law divergence of the correlation length can be equivalently written in terms of reduced hopping strength as

$$\xi \propto |J - J_c|^{-\nu}. \tag{5.9}$$

For our studies based on the statistics of the SF clusters in the BG phase, we choose the system size as 1000×1000. We have observed finite-size effects for system sizes up to 100×100. The finite-size effects are due to the poor statistics resulting from fewer domains in a small system. To fix this, we use a larger system size to obtain reasonable domain statistics. The sample to sample variation in the correlation length gets reduced as the statistics is improved. However, the calculation of ρ_s is performed with a 100×100 system, as the computations with the twisted boundary conditions require a long execution time for a 1000×1000 system. The loop over the twist angles in the computation of the ρ_s is responsible for long execution time. Also, in general, the system size of 100×100 is suitable for other studies to probe the average or coarse-grained properties, such as the determination of the phase diagram and quench dynamics. The order parameters are ensemble averaged over 60 disorder realizations.

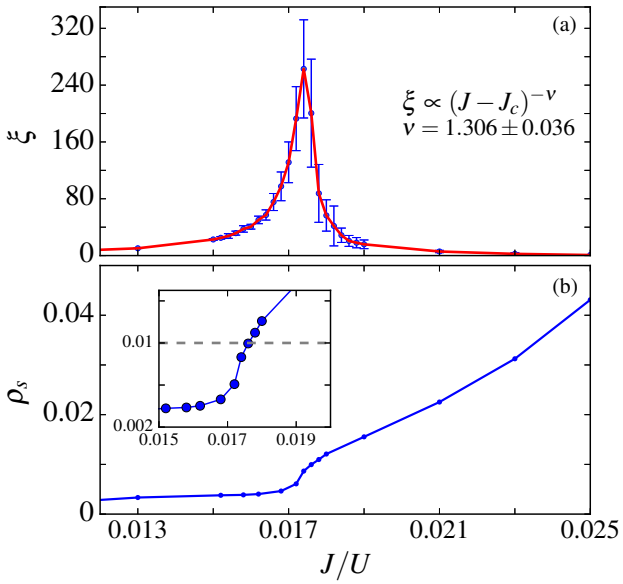

Figure 5.3: Plot of the correlation length ξ and the superfluid stiffness ρ_s as a function of J/U. The chemical potential is $\mu = 0.2U$ and disorder strength is $\Delta = 1.2U$ for these calculations. The results are obtained by averaging over 60 disorder realizations. In plot (a), we observe a divergence of ξ, signaling the percolation transition from the BG to SF phase, with $J_c \approx 0.017U$. The critical exponent is $\nu = 1.306 \pm 0.036$. The standard deviation from the average value is shown by the blue error bar. Plot (b) denotes the stiffness ρ_s as a function of J/U. There is an increase in the stiffness near $J/U \approx 0.017$ as shown in the inset. For numerical calculations, the threshold value 0.01 (shown in gray dashed line) is considered to distinguish between the BG and SF phase.

5.2.1 Results of BG-to-SF transition

The correlation length ξ as a function of J/U is shown in the Fig. 5.3 (a). As evident from the figure, ξ diverges at $J/U \approx 0.017$. The divergence of ξ signals a percolation transition from the BG phase to the SF phase. For small J/U values corresponding to the BG phase, the ξ is small. This is due to the small sized non-percolating SF clusters in the BG phase. However, the ξ increases as the J_c is approached. As the contribution from the infinite, percolating clusters is omitted, the ξ reduces after crossing the J_c. Using the relation in Eq. (5.9), we calculate the exponent ν which quantifies the divergence. Our calculations yield $\nu = 1.306 \pm 0.036$. The obtained ν value is in excellent agreement with the value of $\nu = 4/3$ corresponding to the universality class of a 2D

random site percolation model. The exponent ν was also computed in previous studies [277, 308] and the values reported are in good agreement with our results.

As a further study of the BG-SF transition, we compute the superfluid stiffness ρ_s, across the J_c. The plot of ρ_s is shown in Fig. 5.3 (b). The ρ_s has small value in the BG phase, as the global phase coherence is absent in the system. It shows an increase as the system enters the SF domain. Based on the experience in the previous work [105], we consider $\rho_s \approx 10^{-2}$ as a threshold for distinguishing the BG and SF phase. The plot shows an increase in ρ_s at $J/U \approx 0.017$, and the threshold is crossed at $J = 0.0174U$. The ξ also exhibits a divergence close to this J value. Thus, the identification of the BG-SF transition with the order parameter ρ_s matches with the percolation analysis.

5.3 Summary of the chapter

In conclusion, we have studied the percolation analysis of the BG-to-SF phase transition in the DBHM. We have computed the correlation length ξ using the percolation theory across the BG-SF transition. There is a power-law divergence of ξ near the J_c of the transition. The critical exponent of the divergence is $\nu = 1.306 \pm 0.036$. This analysis demonstrates that the BG-SF transition belongs to the 2D site percolation universality class. We have also computed the superfluid stiffness ρ_s across the BG-SF transition. The critical point J_c obtained with the order parameter ρ_s agrees with the percolation analysis. Therefore, the percolation analysis provides a suitable identification of the BG-SF quantum phase transition.

Chapter 6

Scopes for future work

6.1 Thesis conclusions

To summarize the thesis, we have investigated the quantum phases of dipolar bosonic atoms loaded in square lattice potentials. We have modeled the system with the extended Bose-Hubbard model (eBHM) which is the isotropic limit of the dipolar interaction. We present the phase diagrams of the system and discuss on the parameter domain of the novel supersolid (SS) phase. We have demonstrated the qualitative as well as quantitative differences in the phase diagrams computed by the single site Gutzwiller and cluster Gutzwiller mean-field theories due to the quantum fluctuations incorporated in the latter. For instance, the parameter domain of the SS phase is shrinked with the CGMF method. We have demonstrated this key role of quantum fluctuations by the cluster finite-size scaling analysis. For the density wave to supersolid transition, the critical J_c decreases; while for the Mott Insulator to superfluid transition, the J_c increases. Furthermore, we have shown that in the presence of the artificial gauge field, the domain of the SS phase is enhanced. This increase in the domain of the supersolidity is due to the cyclotronic motion of the atoms in the artificial gauge field. We have also demonstrated the gauge invariance of the phase boundaries in the phase diagrams.

Next, we have investigated the quantum quench dynamics of the ultracold bosonic atoms in optical lattices. For the quenching of the hopping amplitude J across the MI-SF QPT, we have studied the development of the SF order parameter during the dynamics. Based on the Kibble-Zurek mechanism (KZM), we have identified the im-

pulse and the adiabatic regimes in the dynamics, and more importantly have precisely located the transition time instant $\hat{t}$ between the adiabatic and impulse regimes, using the overlap protocol. As expected in the KZM, We have demonstrated the KZ scaling of the $\hat{t}$, the correlation length and the amount of the defects generated as a function of quenching rate. The scaling exponents of these scaling laws also obey the scaling relations. Similar to the quench across the MI-SF QPT, we quench across the stripe density wave to stripe supersolid transition in the dipolar Bose-Hubbard model and obtain the KZ scalings and the critical exponents. The anisotropic dipolar interaction in the dipolar BHM, however, leads to additional novel possibilities, one of them being the quenching across the stripe to checkerboard ordering by tuning the polarization angle of the dipoles. We investigate the dynamics across this first-order QPT and study the evolution of the structure factors capturing the underlying density distribution. We observe that the evolving state remains metastable (in stripe pattern) after crossing the critical point, and after a certain delay (based on the quench rate), the evolving state exhibits the checkerboard domains. We quantify the number of these checkerboard domains and demonstrate that it obeys a power-law scaling with the quench rate.

Finally, we have investigated the quantum phases in the presence of disorder and have studied the critical properties of the Bose-glass (BG) to SF transition using methods of percolation theory. We identify the SF clusters that are characteristic of the BG phase; and study their average size as the BG-SF transition is approached. This correlation length exhibits a power-law divergence near the critical point; the critical exponent value indicates that the BG-SF transition belongs to 2D site percolation universality class.

6.2 Future directions

The studies on the equilibrium quantum phases of the eBHM can be extended in various directions. One immediate extension is to examine the effects of the dipolar interaction terms beyond the nearest-neighbouring sites. Even though it suffices to consider the NN interaction terms as it captures qualitative features, there are important quantitative differences that emerge when interaction terms beyond NN are considered.

These studies can also be extended to other lattice geometries like the triangular and hexagonal optical lattices.

In chapter 4, we have discussed the quench dynamics studies and have obtained the KZ scaling laws. These studies can be extended in various ways. It would be interesting to examine the growth of the domains and the phase ordering kinetics in the quench dynamics. Apart from that, there are relatively few works on the KZ scaling laws for the QPTs in the presence of disorder; and it is interesting to investigate the dynamics across the BG-SF transition. We also plan to investigate the quench dynamics using the time-dependent cluster Gutzwiller mean-field methods, thereby considering the fluctuations and their role in the dynamics. Our studies on the percolation analysis of the BG-SF transition as discussed in chapter 5 can be extended to compute the fractal properties and the fractal dimension of the SF clusters. In this context, the algorithm for the percolation studies can be extended to 3D lattices.

Appendix A

Comparison with known algorithms

We have compared the execution times for the domain identification required by the HK, DC and the recursive neighbour search algorithms. For this comparison, we have generated 40 lattice configurations in which the lattice sites are randomly labeled with 0 and -1 with probability p and $1-p$, and we have fixed $p = 0.5$. For every generated configuration, we have identified the domains using the three algorithms and have noted the time required. We have averaged the execution time over these 40 samples. The Fortran implementation of these algorithms have been executed on an HP EliteDesk PC with Intel i7 processor.

As stated earlier, the comparison between the execution times taken by the HK and the DC algorithms in main panel in Fig. 2.11. We have used the implementation of the HK algorithm in the Fortran language from GitHub [309] to obtain the results with the HK algorithm. The plot indicates that the DC algorithm is faster than the HK algorithm. The least square fit to the data yields $T_{\rm DC} = 9.58{\rm N_s}^{1.01}$ nanoseconds and $T_{\rm HK} = 16.05{\rm N_s}^{1.00}$ nanoseconds, where $T_{\rm DC}(T_{\rm HK})$ denote the execution time required in the DC (HK) algorithm. Bsed on these quantitative results, only for the lattices of size $\approx 10^{12} \times 10^{12}$, the DC algorithm shall require more execution time than the HK algorithm. In the main panel of Fig. 2.11, the time comprises of the time required for the first scan and for the following post-processing steps. The post-processing step in the DC algorithm is about reassigning the cluster labels in ascending order. as the cluster labels after the first scan are not in sequential. Also, the post-processing step in the HK algorithm is required to label the clusters uniquely as the algorithm is a

multiple-cluster labeling technique. However, in the DC algorithm, the post-processing is for rearranging the cluster labels; the clusters are labeled with unique labels even at the end of the first scan. This is another advantage of the DC algorithm.

The post-processing in the DC and HK algorithms are because of the domain mergers. There are no domain merging scenarios in the recursive neighbour search method, and therefore there is no post-processing of labels in the recursion method. Hence we have compared the exection times of the algorithms till the first scan, avoiding the post-processing of the data. This is shown in inset plot in Fig. 2.11. We have illustrated the comparison for a small range of lattice sizes for better readability of the figure. The DC algorithm requires extra time, around 4% more relative to the HK algorithm. This extra time is related to the construction of the linked-lists. This also suggests that the post-processing in the DC algorithm requires lesser time than that in the HK algorithm. In the DC approach, the post-processing involves transfer of the linked-lists from the old to new cluster labels, without involving a second scan. However, for the HK algorithm, the post-processing is the secondary lattice scan. It is also evident that the recursive neighbour search is slower than the DC and the HK algorithm, which is another disadvantage of this method.

Appendix B

Time-dependent Gutzwiller method

In this appendix, we shall derive the time-dependent Gutzwiller mean-field equations that we use to study the quench dynamics. For deriving the equations, We consider the evolution under the BHM Hamiltonian. Other variations of the BHM, like the extended BHM or the dipolar BHM, can be accordingly modified in the equations derived below. The time-dependent variational principle is utilized and the single-site Lagrangian for site (p, q) is given as [310]

$$L_{p,q} = i\,{}_{p,q}\langle\Psi(t)|\partial_t\,|\Psi(t)\rangle_{p,q} - {}_{p,q}\langle\Psi(t)|\hat{h}_{p,q}\,|\Psi(t)\rangle_{p,q} \tag{B.1}$$

The Gutzwiller ansatz for the time-dependent wavefunction $|\Psi(t)\rangle_{p,q}$, whereby the coefficients $c_n^{(p,q)}$ now become time-dependent. The first term on the right-hand side of Eq. (B.1) is given as

$$\begin{aligned} & i\,{}_{p,q}\langle\Psi(t)|\partial_t\,|\Psi(t)\rangle_{p,q} \\ = \;& i\sum_{m,n} c_m^{(p,q)*}\partial_t c_n^{(p,q)}\langle m|n\rangle \\ = \;& i\sum_{n} c_n^{(p,q)*}\partial_t c_n^{(p,q)} \end{aligned} \tag{B.2}$$

The second term on the right-hand side of Eq. (B.1) is

$$\begin{aligned} & {}_{p,q}\langle\Psi(t)|\hat{h}_{p,q}\,|\Psi(t)\rangle_{p,q} \\ = \;& -\Big[J_x\left(\phi^*_{p+1,q}\sqrt{n}c_m^{(p,q)*}c_n^{(p,q)}\delta_{m,n-1} - \phi^*_{p+1,q}\phi_{p,q}c_m^{(p,q)*}c_n^{(p,q)}\delta_{m,n}\right) \\ & + J_x^*\left(\phi^*_{p+1,q}\sqrt{m}c_m^{(p,q)*}c_n^{(p,q)}\delta_{m-1,n} - \phi^*_{p,q}\phi_{p+1,q}c_m^{(p,q)*}c_n^{(p,q)}\delta_{m,n}\right)\Big] \\ & - \Big[J_x\left(\phi_{p-1,q}\sqrt{m}c_m^{(p,q)*}c_n^{(p,q)}\delta_{m-1,n} - \phi^*_{p,q}\phi_{p-1,q}c_m^{(p,q)*}c_n^{(p,q)}\delta_{m,n}\right) \end{aligned}$$

$$
\begin{aligned}
&+ \quad J_x^* \left(\phi_{p-1,q}^* \sqrt{n} c_m^{(p,q)*} c_n^{(p,q)} \delta_{m,n-1} - \phi_{p-1,q}^* \phi_{p,q} c_m^{(p,q)*} c_n^{(p,q)} \delta_{m,n}\right)\Big] \\
&- \quad \Big[J_y \left(\phi_{p,q+1} \sqrt{m} c_m^{(p,q)*} c_n^{(p,q)} \delta_{m-1,n} - \phi_{p,q}^* \phi_{p,q+1} c_m^{(p,q)*} c_n^{(p,q)} \delta_{m,n}\right) \\
&+ \quad J_y^* \left(\phi_{p,q+1}^* \sqrt{n} c_m^{(p,q)*} c_n^{(p,q)} \delta_{m,n-1} - \phi_{p,q+1}^* \phi_{p,q} c_m^{(p,q)*} c_n^{(p,q)} \delta_{m,n}\right)\Big] \\
&- \quad \Big[J_y \left(\phi_{p,q-1}^* \sqrt{n} c_m^{(p,q)*} c_n^{(p,q)} \delta_{m,n-1} - \phi_{p,q-1}^* \phi_{p,q} c_m^{(p,q)*} c_n^{(p,q)} \delta_{m,n}\right) \\
&+ \quad J_y^* \left(\phi_{p,q-1} \sqrt{m} c_m^{(p,q)*} c_n^{(p,q)} \delta_{m-1,n} - \phi_{p,q}^* \phi_{p,q-1} c_m^{(p,q)*} c_n^{(p,q)} \delta_{m,n}\right)\Big] \\
&+ \quad \frac{U}{2} n(n-1) - \mu n
\end{aligned}
\tag{B.3}
$$

Using the Lagrangian equations of motion,

$$
\partial_t \left[\frac{\partial L}{\partial \left(\partial_t c_n^{(p,q)}\right)}\right] = \frac{\partial L}{\partial c_n^{(p,q)}} \tag{B.4}
$$

A set of first-order coupled differential equations for $c_n^{(p,q)}$ is then obtained:

$$
\begin{aligned}
i\partial_t c_n^{(p,q)} = \quad &- \quad \Big[\sqrt{n} c_{n-1}^{(p,q)} \left(J_x^* \phi_{p+1,q} + J_x \phi_{p-1,q} + J_y^* \phi_{p,q-1} + J_y \phi_{p,q+1}\right) \\
&+ \quad \sqrt{n+1} c_{n+1}^{(p,q)} \left(J_x^* \phi_{p-1,q}^* + J_x \phi_{p+1,q}^* + J_y^* \phi_{p,q+1}^* + J_y \phi_{p,q-1}^*\right) \\
&- \quad c_n^{(p,q)} \left(J_x^* \phi_{p+1,q} \phi_{p,q}^* + J_x \phi_{p+1,q}^* \phi_{p,q} + J_x^* \phi_{p,q} \phi_{p-1,q}^* + J_x \phi_{p,q}^* \phi_{p-1,q}\right. \\
&+ \quad \left. J_y^* \phi_{p,q+1}^* \phi_{p,q} + J_y \phi_{p,q+1} \phi_{p,q}^* + J_y^* \phi_{p,q}^* \phi_{p,q-1} + J_y \phi_{p,q} \phi_{p,q-1}^*\right)\Big] \\
&+ \quad \Big[\frac{U}{2} n(n-1) - \mu n\Big] c_n^{(p,q)}
\end{aligned}
\tag{B.5}
$$

So for every site (p, q), there is a set of coupled differential equations for the coefficients of the wavefunction. We solve this set of equations using the fourth-order Runge Kutta method. It is to be noted that we have explicitly considered the diagonal $\phi^*\phi$ type of terms in the dynamical equations. We have seen that in the equilibrium studies these diagonal terms are a constant shift in energy and do not alter the phase diagrams. However, this is not the case in the dynamical evolution. There is a significant difference in the dynamics based on the inclusion of these terms.

Appendix C

Bogoliubov excitations in optical lattices

The choice of the strength Δ for the density fluctuqtions is based on the collective excitations of the equilibrium ground state at initial time. To obtain these Bogoliubov-de Gennes (BdG) modes, fluctuations are added to the equilibrium ground state [311–315].

$$c_n^{(p,q)}(t) = \left(\bar{c}_n^{(p,q)} + \delta c_n^{(p,q)}(t)\right) e^{-i\omega_0^{(p,q)}t}, \tag{C.1}$$

where $\bar{c}_n^{(p,q)}$ corresponds to the equilibrium ground state coefficient, $\delta c_n^{(p,q)}(t)$ is the fluctuation added to the ground state and the $\omega_0^{(p,q)}$ corresponds to the energy of the unperturbed state at the lattice site (p, q). To obtain the collective excitations, we use the Bogoliubov approximation and define

$$\delta c_n^{(p,q)}(t) = u_n^{(p,q)} e^{-i\omega t} + v_n^{*(p,q)} e^{i\omega t}, \tag{C.2}$$

where ω is the energy of the collective mode, and (u_n, v_n) is the amplitude of the collective mode. The $c_n^{(p,q)}(t)$ are substituted in the dynamical Gutzwiller equations, and terms linear in the fluctuation operator are retained. That is, we linearize the equations. The resulting set of equations is referred to as the BdG equations. After solving the equations, we obtain the δc_n. Once we obtain δc_n, we use it to calculate the $\delta\langle\hat{n}\rangle$ given as

$$\delta\langle\hat{n}_{p,q}\rangle = \sum_k k \left(\bar{c}_k^{*(p,q)} \delta c_k^{(p,q)} + \bar{c}_k^{(p,q)} \delta c_k^{*(p,q)}\right). \tag{C.3}$$

The order of the magnitude of the $\delta\langle\hat{n}_{p,q}\rangle$ is then used to fix the Δ.

Appendix D

System Unwrapping

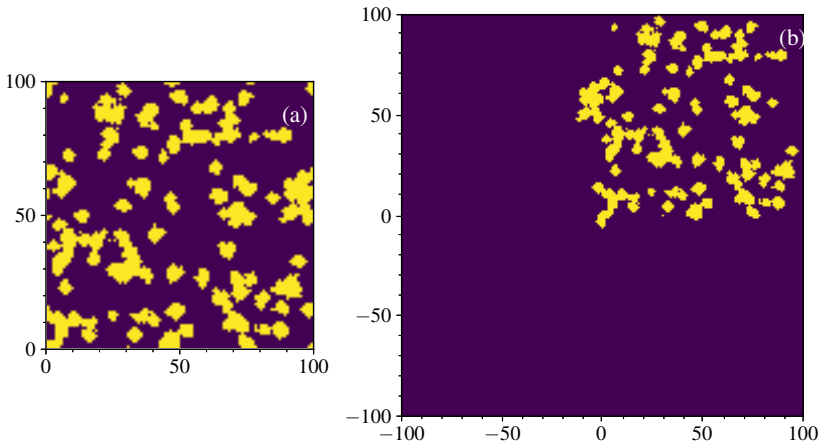

Figure D.1: Unwrapping of clusters in the percolation theory. In (a), the original distribution of the clusters of label 0 is shown, while in (b), the clusters in (a) are unwrapped and mapped onto a larger system (that is quadrapolar in size as compared to the original system).

In this appendix, we describle the unwrapping procedure that is used to compute the distances within the lattice without any ambiguity. We map the system of size $L_x \times L_y$ with periodic boundary conditions to a larger system of size $2L_x \times 2L_y$ with open boundary condition. The clusters that touch the edges of the system require a shift, and hence these clusters are identified first. Suppose a cluster straddles the left and the right

edge of a system, and with the PBC, these left and right chunks are a part of the same cluster. In this case, the right chunk is provided with a x-shift that translates it along the negative x-direction by a distance L_x, making it appear side-by-side, and connected. For certain cases, a cluster may straddle across both directions, thereby requiring both x-shift and y-shift. As an illustration, we have shown the unwrapping of the clusters in Fig. D.1. Once these steps are performed, we compute the geometrical properties of the clusters, with unique distance notion. These steps would fail for percolating clusters that are infinite in length. In such cases, it is not possible to accomodate them in a system of finite size. However, as stated in the main text, the percolation analysis of the system generally ignores the contribution from the percolating clusters, thereby shifting the finite sized non-percolating clusters suffices to perform the percolation studies.

Bibliography

[1] S. Sachdev, *Quantum Phase Transitions* (Cambridge University Press, 2011), 2nd ed.

[2] H. Nishimori and G. Oritz, *Elements of Phase Transitions and Critical Phenomena* (Oxford University Press (Oxford), 2010).

[3] C. N. Cohen-Tannoudji, *Nobel Lecture: Manipulating atoms with photons,* Rev. Mod. Phys. **70**, 707 (1998).

[4] S. Chu, *Nobel Lecture: The manipulation of neutral particles,* Rev. Mod. Phys. **70**, 685 (1998).

[5] W. D. Phillips, *Nobel Lecture: Laser cooling and trapping of neutral atoms,* Rev. Mod. Phys. **70**, 721 (1998).

[6] W. Ketterle, *Nobel lecture: When atoms behave as waves: Bose-einstein condensation and the atom laser,* Rev. Mod. Phys. **74**, 1131–1151 (2002).

[7] F. Dalfovo, S. Giorgini, L. P. Pitaevskii, and S. Stringari, *Theory of Bose-Einstein condensation in trapped gases,* Rev. Mod. Phys. **71**, 463 (1999).

[8] A. Einstein, *Quantentheorie des einatomigen idealen gases,* S. B. Preuss. Akad. Wiss. phys.-math. Klasse (1924).

[9] S. N. Bose, *Plancks gesetz und lichtquantenhypothese,* Zeitschrift für Physik **26**, 178 (1924).

[10] C. Chin, R. Grimm, P. Julienne, and E. Tiesinga, *Feshbach resonances in ultracold gases,* Rev. Mod. Phys. **82**, 1225 (2010).

[11] P. Soltan-Panahi, J. Struck, P. Hauke, A. Bick, W. Plenkers, G. Meineke, C. Becker, P. Windpassinger, M. Lewenstein, and K. Sengstock, *Multi-component quantum gases in spin-dependent hexagonal lattices,* Nature Physics **7**, 434–440 (2011).

[12] D.-S. Lühmann, O. Jürgensen, M. Weinberg, J. Simonet, P. Soltan-Panahi, and K. Sengstock, *Quantum phases in tunable state-dependent hexagonal optical lattices,* Phys. Rev. A **90**, 013614 (2014).

[13] C. Becker, P. Soltan-Panahi, J. Kronjger, S. Drscher, K. Bongs, and K. Sengstock, *Ultracold quantum gases in triangular optical lattices,* New Journal of Physics **12**, 065025 (2010).

[14] J. Struck, M. Weinberg, C. Ölschläger, P. Windpassinger, J. Simonet, K. Sengstock, R. Höppner, P. Hauke, A. Eckardt, M. Lewenstein, and L. Mathey, *Engineering ising-xy spin-models in a triangular lattice using tunable artificial gauge fields,* Nature Physics **9**, 738–743 (2013).

[15] L. Santos, M. A. Baranov, J. I. Cirac, H.-U. Everts, H. Fehrmann, and M. Lewenstein, *Atomic quantum gases in kagomé lattices,* Phys. Rev. Lett. **93**, 030601 (2004).

[16] T. H. Barter, T.-H. Leung, M. Okano, M. Block, N. Y. Yao, and D. M. Stamper-Kurn, *Spatial coherence of a strongly interacting bose gas in the trimerized kagome lattice,* Phys. Rev. A **101**, 011601 (2020).

[17] M. Greiner, O. Mandel, T. Esslinger, T. W. Hänsch, and I. Bloch, *Quantum phase transition from a superfluid to a Mott insulator in a gas of ultracold atoms,* Nature (London) **415**, 39 (2002).

[18] M. Greiner, O. Mandel, T. W. Hänsch, and I. Bloch, *Collapse and revival of the matter wave field of a bose-einstein condensate,* Nature **419**, 51 (2002).

[19] M. P. A. Fisher, P. B. Weichman, G. Grinstein, and D. S. Fisher, *Boson localization and the superfluid-insulator transition,* Phys. Rev. B **40**, 546 (1989).

[20] D. Jaksch, C. Bruder, J. I. Cirac, C. W. Gardiner, and P. Zoller, *Cold bosonic atoms in optical lattices,* Phys. Rev. Lett. **81**, 3108 (1998).

[21] J. Hubbard, *Electron correlations in narrow energy bands,* Proc. Royal Soc. A **276**, 238 (1963).

[22] A. Griesmaier, J. Werner, S. Hensler, J. Stuhler, and T. Pfau, *Bose-Einstein condensation of chromium,* Phys. Rev. Lett. **94**, 160401 (2005).

[23] A. Griesmaier, *Generation of a dipolar bose–einstein condensate,* Journal of Physics B: Atomic, Molecular and Optical Physics **40**, R91–R134 (2007).

[24] M. Lu, N. Q. Burdick, S. H. Youn, and B. L. Lev, *Strongly dipolar Bose-Einstein condensate of dysprosium,* Phys. Rev. Lett. **107**, 190401 (2011).

[25] K. Aikawa, A. Frisch, M. Mark, S. Baier, A. Rietzler, R. Grimm, and F. Ferlaino, *Bose-Einstein condensation of erbium,* Phys. Rev. Lett. **108**, 210401 (2012).

[26] S. Baier, M. J. Mark, D. Petter, K. Aikawa, L. Chomaz, Z. Cai, M. Baranov, P. Zoller, and F. Ferlaino, *Extended Bose-Hubbard models with ultracold magnetic atoms,* Science **352**, 201 (2016).

[27] L. Chomaz, R. M. W. van Bijnen, D. Petter, G. Faraoni, S. Baier, J. H. Becher, M. J. Mark, F. Wächtler, L. Santos, and F. Ferlaino, *Observation of roton mode population in a dipolar quantum gas,* Nature Physics **14**, 442 (2018).

[28] D. Petter, G. Natale, R. M. W. van Bijnen, A. Patscheider, M. J. Mark, L. Chomaz, and F. Ferlaino, *Probing the roton excitation spectrum of a stable dipolar Bose gas,* Phys. Rev. Lett. **122**, 183401 (2019).

[29] Y. Miyazawa, R. Inoue, H. Matsui, G. Nomura, and M. Kozuma, *Bose-einstein condensation of europium,* (2022).

[30] S. Ospelkaus, C. Ospelkaus, O. Wille, M. Succo, P. Ernst, K. Sengstock, and K. Bongs, *Localization of bosonic atoms by fermionic impurities in a three-dimensional optical lattice,* Phys. Rev. Lett. **96**, 180403 (2006).

[31] S. Ospelkaus, A. Pe'er, K.-K. Ni, J. J. Zirbel, B. Neyenhuis, S. Kotochigova, P. S. Julienne, J. Ye, and D. S. Jin, *Efficient state transfer in an ultracold dense gas of heteronuclear molecules,* Nature Physics **4**, 622–626 (2008).

[32] S. Ospelkaus, K.-K. Ni, M. H. G. de Miranda, B. Neyenhuis, D. Wang, S. Kotochigova, P. S. Julienne, D. S. Jin, and J. Ye, *Ultracold polar molecules near quantum degeneracy,* Faraday Discuss **142**, 351 (2009).

[33] K.-K. Ni, S. Ospelkaus, M. H. G. de Miranda, A. Pe'er, B. Neyenhuis, J. J. Zirbel, S. Kotochigova, P. S. Julienne, D. S. Jin, and J. Ye, *A high phase-space-density gas of polar molecules,* Science **322**, 231 (2008).

[34] J. G. Danzl, E. Haller, M. Gustavsson, M. J. Mark, R. Hart, N. Bouloufa, O. Dulieu, H. Ritsch, and H.-C. Nägerl, *Quantum gas of deeply bound ground state molecules,* Science **321**, 1062 (2008).

[35] H. Kadau, M. Schmitt, M. Wenzel, C. Wink, T. Maier, I. Ferrier-Barbut, and T. Pfau, *Observing the rosensweig instability of a quantum ferrofluid,* Nature **530**, 194 (2016).

[36] T. Lahaye, C. Menotti, L. Santos, M. Lewenstein, and T. Pfau, *The physics of dipolar bosonic quantum gases,* Reports on Progress in Physics **72**, 126401 (2009).

[37] C. Trefzger, C. Menotti, and M. Lewenstein, *Ultracold dipolar gas in an optical lattice: The fate of metastable states,* Phys. Rev. A **78**, 043604 (2008).

[38] C. Menotti, C. Trefzger, and M. Lewenstein, *Metastable states of a gas of dipolar bosons in a 2d optical lattice,* Phys. Rev. Lett. **98**, 235301 (2007).

[39] T. Lahaye, T. Koch, B. Fröhlich, M. Fattori, J. Metz, A. Griesmaier, S. Giovanazzi, and T. Pfau, *Strong dipolar effects in a quantum ferrofluid,* Nature **448**, 672 (2007).

[40] A. F. Andreev and I. M. Lifshitz, *Quantum theory of defects in crystals,* Sov. Phys. JETP **29**, 1107 (1969).

[41] D. J. Thouless, *The flow of a dense superfluid,* Ann. Phys. **52**, 403 (1969).

[42] G. V. Chester, *Speculations on Bose-Einstein condensation and quantum crystals,* Phys. Rev. A **2**, 256 (1970).

[43] A. J. Leggett, *Can a solid be superfluid?* Phys. Rev. Lett. **25**, 1543 (1970).

[44] O. Penrose and L. Onsager, *Bose-Einstein condensation and liquid helium,* Phys. Rev. **104**, 576 (1956).

[45] H. Matsuda and T. Tsuneto, *Off-diagonal long-range order in solids*), Progress of Theoretical Physics Supplement **46**, 411–436 (1970).

[46] E. Kim and M. H. W. Chan, *Probable observation of a supersolid helium phase,* Nature (London) **427**, 225 (2004).

[47] E. Kim and M. H. W. Chan, *Observation of superflow in solid helium,* Science **305**, 1941 (2004).

[48] D. Y. Kim and M. H. W. Chan, *Absence of supersolidity in solid helium in porous vycor glass,* Phys. Rev. Lett. **109**, 155301 (2012).

[49] M. H. W. Chan, R. B. Hallock, and L. Reatto, *Overview on solid 4he and the issue of supersolidity,* Journal of Low Temperature Physics **172**, 317 (2013).

[50] L. Santos, G. V. Shlyapnikov, and M. Lewenstein, *Roton-maxon spectrum and stability of trapped dipolar Bose-Einstein condensates,* Phys. Rev. Lett. **90**, 250403 (2003).

[51] L. Tanzi, E. Lucioni, F. Famà, J. Catani, A. Fioretti, C. Gabbanini, R. N. Bisset, L. Santos, and G. Modugno, *Observation of a dipolar quantum gas with metastable supersolid properties,* Phys. Rev. Lett. **122**, 130405 (2019).

[52] F. Böttcher, J.-N. Schmidt, M. Wenzel, J. Hertkorn, M. Guo, T. Langen, and T. Pfau, *Transient supersolid properties in an array of dipolar quantum droplets,* Phys. Rev. X **9**, 011051 (2019).

[53] L. Chomaz, D. Petter, P. Ilzhöfer, G. Natale, A. Trautmann, C. Politi, G. Durastante, R. M. W. van Bijnen, A. Patscheider, M. Sohmen, M. J. Mark, and F. Ferlaino, *Long-lived and transient supersolid behaviors in dipolar quantum gases,* Phys. Rev. X **9**, 021012 (2019).

[54] M. A. Norcia, C. Politi, L. Klaus, E. Poli, M. Sohmen, M. J. Mark, R. N. Bisset, L. Santos, and F. Ferlaino, *Two-dimensional supersolidity in a dipolar quantum gas,* Nature **596**, 357–361 (2021).

[55] T. Bland, E. Poli, C. Politi, L. Klaus, M. A. Norcia, F. Ferlaino, L. Santos, and R. N. Bisset, *Two-dimensional supersolid formation in dipolar condensates,* Phys. Rev. Lett. **128**, 195302 (2022).

[56] R. Landig, L. Hruby, N. Dogra, M. Landini, R. Mottl, T. Donner, and T. Esslinger, *Quantum phases from competing short- and long-range interactions in an optical lattice,* Nature (London) **532**, 476 (2016).

[57] R. Mottl, F. Brennecke, K. Baumann, R. Landig, T. Donner, and T. Esslinger, *Roton-type mode softening in a quantum gas with cavity-mediated long-range interactions,* Science **336**, 1570 (2012).

[58] J. Lonard, A. Morales, P. Zupancic, T. Esslinger, and T. Donner, *Supersolid formation in a quantum gas breaking a continuous translational symmetry,* Nature (London) **543**, 87 (2017).

[59] J.-R. Li, J. Lee, W. Huang, S. Burchesky, B. Shteynas, F. . Top, A. O. Jamison, and W. Ketterle, *A stripe phase with supersolid properties in spin-orbit-coupled Bose-Einstein condensates,* Nature (London) **543**, 91 (2017).

[60] M. A. Khamehchi, Y. Zhang, C. Hamner, T. Busch, and P. Engels, *Measurement of collective excitations in a spin-orbit-coupled Bose-Einstein condensate,* Phys. Rev. A **90**, 063624 (2014).

[61] S.-C. Ji, L. Zhang, X.-T. Xu, Z. Wu, Y. Deng, S. Chen, and J.-W. Pan, *Softening of roton and phonon modes in a Bose-Einstein condensate with spin-orbit coupling,* Phys. Rev. Lett. **114**, 105301 (2015).

[62] T. M. Bersano, J. Hou, S. Mossman, V. Gokhroo, X.-W. Luo, K. Sun, C. Zhang, and P. Engels, *Experimental realization of a long-lived striped Bose-Einstein condensate induced by momentum-space hopping,* Phys. Rev. A **99**, 051602 (2019).

[63] F. Cinti, P. Jain, M. Boninsegni, A. Micheli, P. Zoller, and G. Pupillo, *Supersolid droplet crystal in a dipole-blockaded gas,* Phys. Rev. Lett. **105**, 135301 (2010).

[64] N. Henkel, R. Nath, and T. Pohl, *Three-dimensional roton excitations and supersolid formation in rydberg-excited Bose-Einstein condensates,* Phys. Rev. Lett. **104**, 195302 (2010).

[65] G. Natale, R. M. W. van Bijnen, A. Patscheider, D. Petter, M. J. Mark, L. Chomaz, and F. Ferlaino, *Excitation spectrum of a trapped dipolar supersolid and its experimental evidence,* Phys. Rev. Lett. **123**, 050402 (2019).

[66] L. Tanzi, S. M. Roccuzzo, E. Lucioni, F. Fam, A. Fioretti, C. Gabbanini, G. Modugno, A. Recati, and S. Stringari, *Supersolid symmetry breaking from compressional oscillations in a dipolar quantum gas,* Nature **574**, 382 (2019).

[67] M. Guo, F. Bttcher, J. Hertkorn, J.-N. Schmidt, M. Wenzel, H. P. Bchler, T. Langen, and T. Pfau, *The low-energy goldstone mode in a trapped dipolar supersolid,* Nature **574**, 386 (2019).

[68] T. Sowiński, O. Dutta, P. Hauke, L. Tagliacozzo, and M. Lewenstein, *Dipolar molecules in optical lattices,* Phys. Rev. Lett. **108**, 115301 (2012).

[69] G. G. Batrouni and R. T. Scalettar, *Phase separation in supersolids,* Phys. Rev. Lett. **84**, 1599 (2000).

[70] S. Wessel, *Phase diagram of interacting bosons on the honeycomb lattice,* Phys. Rev. B **75**, 174301 (2007).

[71] J. Y. Gan, Y. C. Wen, J. Ye, T. Li, S.-J. Yang, and Y. Yu, *Extended Bose-Hubbard model on a honeycomb lattice,* Phys. Rev. B **75**, 214509 (2007).

[72] A. van Otterlo, K.-H. Wagenblast, R. Baltin, C. Bruder, R. Fazio, and G. Schön, *Quantum phase transitions of interacting bosons and the supersolid phase,* Phys. Rev. B **52**, 16176–16186 (1995).

[73] P. Sengupta, L. P. Pryadko, F. Alet, M. Troyer, and G. Schmid, *Supersolids versus phase separation in two-dimensional lattice bosons,* Phys. Rev. Lett. **94**, 207202 (2005).

[74] T. Ohgoe, T. Suzuki, and N. Kawashima, *Ground-state phase diagram of the two-dimensional extended bose-hubbard model,* Phys. Rev. B **86**, 054520 (2012).

[75] T. Flottat, L. d. deParny, F. Hébert, V. G. Rousseau, and G. G. Batrouni, *Phase diagram of bosons in a two-dimensional optical lattice with infinite-range cavity-mediated interactions,* Phys. Rev. B **95**, 144501 (2017).

[76] L. Mathey, I. Danshita, and C. W. Clark, *Creating a supersolid in one-dimensional Bose mixtures,* Phys. Rev. A **79**, 011602(R) (2009).

[77] G. G. Batrouni, F. Hébert, and R. T. Scalettar, *Supersolid phases in the one-dimensional extended soft-core bosonic Hubbard model,* Phys. Rev. Lett. **97**, 087209 (2006).

[78] R. Sachdeva, M. Singh, and T. Busch, *Extended Bose-Hubbard model for two-leg ladder systems in artificial magnetic fields,* Phys. Rev. A **95**, 063601 (2017).

[79] K. Góral, L. Santos, and M. Lewenstein, *Quantum phases of dipolar bosons in optical lattices,* Phys. Rev. Lett. **88**, 170406 (2002).

[80] V. W. Scarola and S. Das Sarma, *Quantum phases of the extended Bose-Hubbard Hamiltonian: Possibility of a supersolid state of cold atoms in optical lattices,* Phys. Rev. Lett. **95**, 033003 (2005).

[81] S. Yi, T. Li, and C. P. Sun, *Novel quantum phases of dipolar Bose gases in optical lattices,* Phys. Rev. Lett. **98**, 260405 (2007).

[82] K.-K. Ng and Y.-C. Chen, *Supersolid phases in the bosonic extended Hubbard model,* Phys. Rev. B **77**, 052506 (2008).

[83] B. Capogrosso-Sansone, C. Trefzger, M. Lewenstein, P. Zoller, and G. Pupillo, *Quantum phases of cold polar molecules in 2D optical lattices,* Phys. Rev. Lett. **104**, 125301 (2010).

[84] S. Bandyopadhyay, R. Bai, S. Pal, K. Suthar, R. Nath, and D. Angom, *Quantum phases of canted dipolar bosons in a two-dimensional square optical lattice,* Phys. Rev. A **100**, 053623 (2019).

[85] S. Wessel and M. Troyer, *Supersolid hard-core bosons on the triangular lattice,* Phys. Rev. Lett. **95**, 127205 (2005).

[86] D. Heidarian and K. Damle, *Persistent supersolid phase of hard-core bosons on the triangular lattice,* Phys. Rev. Lett. **95**, 127206 (2005).

[87] R. G. Melko, A. Paramekanti, A. A. Burkov, A. Vishwanath, D. N. Sheng, and L. Balents, *Supersolid order from disorder: Hard-core bosons on the triangular lattice,* Phys. Rev. Lett. **95**, 127207 (2005).

[88] M. Boninsegni and N. Prokof'ev, *Supersolid phase of hard-core bosons on a triangular lattice,* Phys. Rev. Lett. **95**, 237204 (2005).

[89] A. Sen, P. Dutt, K. Damle, and R. Moessner, *Variational wave-function study of the triangular lattice supersolid,* Phys. Rev. Lett. **100**, 147204 (2008).

[90] D. Yamamoto, I. Danshita, and C. A. R. Sá de Melo, *Dipolar bosons in triangular optical lattices: Quantum phase transitions and anomalous hysteresis,* Phys. Rev. A **85**, 021601(R) (2012).

[91] S. V. Isakov, S. Wessel, R. G. Melko, K. Sengupta, and Y. B. Kim, *Hard-core bosons on the kagome lattice: Valence-bond solids and their quantum melting,* Phys. Rev. Lett. **97**, 147202 (2006).

[92] D. Huerga, S. Capponi, J. Dukelsky, and G. Ortiz, *Staircase of crystal phases of hard-core bosons on the kagome lattice,* Phys. Rev. B **94**, 165124 (2016).

[93] C. Trefzger, C. Menotti, and M. Lewenstein, *Pair-supersolid phase in a bilayer system of dipolar lattice bosons,* Phys. Rev. Lett. **103**, 035304 (2009).

[94] B. Xi, F. Ye, W. Chen, F. Zhang, and G. Su, *Global phase diagram of three-dimensional extended boson Hubbard model: A continuous-time quantum Monte Carlo study,* Phys. Rev. B **84**, 054512 (2011).

[95] T. Ohgoe, T. Suzuki, and N. Kawashima, *Commensurate supersolid of three-dimensional lattice bosons,* Phys. Rev. Lett. **108**, 185302 (2012).

[96] M. Boninsegni and N. V. Prokof'ev, *Colloquium: Supersolids: What and where are they?* Rev. Mod. Phys. **84**, 759–776 (2012).

[97] M. Aidelsburger, M. Atala, S. Nascimbène, S. Trotzky, Y.-A. Chen, and I. Bloch, *Experimental realization of strong effective magnetic fields in an optical lattice,* Phys. Rev. Lett. **107**, 255301 (2011).

[98] M. Aidelsburger, M. Atala, M. Lohse, J. T. Barreiro, B. Paredes, and I. Bloch, *Realization of the hofstadter hamiltonian with ultracold atoms in optical lattices,* Phys. Rev. Lett. **111**, 185301 (2013).

[99] J. Struck, C. lschlger, R. L. Targat, P. Soltan-Panahi, A. Eckardt, M. Lewenstein, P. Windpassinger, and K. Sengstock, *Quantum simulation of frustrated classical magnetism in triangular optical lattices,* Science **333**, 996–999 (2011).

[100] J. Dalibard, F. Gerbier, G. Juzeliūnas, and P. Öhberg, *Colloquium: Artificial gauge potentials for neutral atoms,* Rev. Mod. Phys. **83**, 1523–1543 (2011).

[101] M. Aidelsburger, *Artificial gauge fields and topology with ultracold atoms in optical lattices,* Journal of Physics B: Atomic, Molecular and Optical Physics **51**, 193001 (2018).

[102] N. R. Cooper, J. Dalibard, and I. B. Spielman, *Topological bands for ultracold atoms,* Rev. Mod. Phys. **91**, 015005 (2019).

[103] P. Hauke and I. Carusotto, *Quantum hall and synthetic magnetic-field effects in ultra-cold atomic systems,* (2022).

[104] Y. Kuno, K. Shimizu, and I. Ichinose, *Bosonic analogs of the fractional quantum Hall state in the vicinity of Mott states,* Phys. Rev. A **95**, 013607 (2017).

[105] S. Pal, R. Bai, S. Bandyopadhyay, K. Suthar, and D. Angom, *Enhancement of the bose glass phase in the presence of an artificial gauge field,* Phys. Rev. A **99**, 053610 (2019).

[106] Y. Kuno, T. Nakafuji, and I. Ichinose, *Phase diagrams of the Bose-Hubbard model and the Haldane-Bose-Hubbard model with complex hopping amplitudes,* Phys. Rev. A **92**, 063630 (2015).

[107] M. Rigol, V. Dunjko, and M. Olshanii, *Thermalization and its mechanism for generic isolated quantum systems,* Nature **452**, 854–858 (2008).

[108] R. Nandkishore and D. A. Huse, *Many-body localization and thermalization in quantum statistical mechanics,* Annual Review of Condensed Matter Physics **6**, 15–38 (2015).

[109] T. W. B. Kibble, *Topology of cosmic domains and strings,* Journal of Physics A: Mathematical and General **9**, 1387 (1976).

[110] W. H. Zurek, *Cosmological experiments in superfluid helium?* Nature **317**, 505 (1985).

[111] A. Polkovnikov, K. Sengupta, A. Silva, and M. Vengalattore, *Colloquium: Nonequilibrium dynamics of closed interacting quantum systems,* Rev. Mod. Phys. **83**, 863–883 (2011).

[112] A. del Campo and W. H. Zurek, *Universality of phase transition dynamics: Topological defects from symmetry breaking,* International Journal of Modern Physics A **29**, 1430018 (2014).

[113] A. J. Bray, *Theory of phase-ordering kinetics,* Advances in Physics **51**, 481–587 (2002).

[114] S. Puri, *Kinetics of phase transitions* (CRC press, 2009).

[115] J. Dziarmaga, *Dynamics of a quantum phase transition and relaxation to a steady state,* Advances in Physics **59**, 1063 (2010).

[116] P. C. Hendry, N. S. Lawson, R. A. M. Lee, P. V. E. McClintock, and C. D. H. Williams, *Generation of defects in superfluid 4he as an analogue of the formation of cosmic strings,* Nature **368**, 315–317 (1994).

[117] C. Bäuerle, Y. M. Bunkov, S. N. Fisher, H. Godfrin, and G. R. Pickett, *Laboratory simulation of cosmic string formation in the early universe using superfluid 3he,* Nature **382**, 332 (1996).

[118] V. M. H. Ruutu, V. B. Eltsov, A. J. Gill, T. W. B. Kibble, M. Krusius, Y. G. Makhlin, B. Plaçais, G. E. Volovik, and W. Xu, *Vortex formation in neutron-irradiated superfluid 3he as an analogue of cosmological defect formation,* Nature **382**, 334 (1996).

[119] I. Chuang, R. Durrer, N. Turok, and B. Yurke, *Cosmology in the laboratory: Defect dynamics in liquid crystals,* Science **251**, 1336 (1991).

[120] M. J. Bowick, L. Chandar, E. A. Schiff, and A. M. Srivastava, *The cosmological kibble mechanism in the laboratory: String formation in liquid crystals,* Science **263**, 943 (1994).

[121] R. Carmi, E. Polturak, and G. Koren, *Observation of spontaneous flux generation in a multi-josephson-junction loop,* Phys. Rev. Lett. **84**, 4966–4969 (2000).

[122] A. Maniv, E. Polturak, and G. Koren, *Observation of magnetic flux generated spontaneously during a rapid quench of superconducting films,* Phys. Rev. Lett. **91**, 197001 (2003).

[123] R. Monaco, J. Mygind, R. J. Rivers, and V. P. Koshelets, *Spontaneous fluxoid formation in superconducting loops,* Phys. Rev. B **80**, 180501 (2009).

[124] S.-Z. Lin, X. Wang, Y. Kamiya, G.-W. Chern, F. Fan, D. Fan, B. Casas, Y. Liu, V. Kiryukhin, W. H. Zurek, and S.-W. Batista, Cristian D.and Cheong, *Topological defects as relics of emergent continuous symmetry and higgs condensation of disorder in ferroelectrics,* Nature Physics **10**, 970 (2014).

[125] G. D. Chiara, A. del Campo, G. Morigi, M. B. Plenio, and A. Retzker, *Spontaneous nucleation of structural defects in inhomogeneous ion chains,* New Journal of Physics **12**, 115003 (2010).

[126] M. Mielenz, J. Brox, S. Kahra, G. Leschhorn, M. Albert, T. Schaetz, H. Landa, and B. Reznik, *Trapping of topological-structural defects in coulomb crystals,* Phys. Rev. Lett. **110**, 133004 (2013).

[127] S. Ulm, J. Roßnagel, G. Jacob, C. Degünther, S. T. Dawkins, U. G. Poschinger, R. Nigmatullin, A. Retzker, M. B. Plenio, F. Schmidt-Kaler, and K. Singer, *Observation of the kibble–zurek scaling law for defect formation in ion crystals,* Nature Communications **4**, 2290 (2013).

[128] K. Pyka, J. Keller, H. L. Partner, R. Nigmatullin, T. Burgermeister, D. M. Meier, K. Kuhlmann, A. Retzker, M. B. Plenio, W. H. Zurek, A. del Campo, and T. E. Mehlstäubler, *Topological defect formation and spontaneous symmetry breaking in ion coulomb crystals,* Nature Communications **4**, 2291 (2013).

[129] W. H. Zurek, U. Dorner, and P. Zoller, *Dynamics of a quantum phase transition,* Phys. Rev. Lett. **95**, 105701 (2005).

[130] B. Damski, *The simplest quantum model supporting the kibble-zurek mechanism of topological defect production: Landau-zener transitions from a new perspective,* Phys. Rev. Lett. **95**, 035701 (2005).

[131] T. Donner, S. Ritter, T. Bourdel, A. ttl, M. Khl, and T. Esslinger, *Critical behavior of a trapped interacting bose gas,* Science **315**, 1556–1558 (2007).

[132] C. N. Weiler, T. W. Neely, D. R. Scherer, A. S. Bradley, M. J. Davis, and B. P. Anderson, *Spontaneous vortices in the formation of bose–einstein condensates,* Nature **455**, 948 (2008).

[133] L. Chomaz, L. Corman, T. Bienaimé, R. Desbuquois, C. Weitenberg, S. Nascimbène, J. Beugnon, and J. Dalibard, *Emergence of coherence via transverse condensation in a uniform quasi-two-dimensional bose gas,* Nature Communications **6**, 6162 (2015).

[134] S. Donadello, S. Serafini, T. Bienaimé, F. Dalfovo, G. Lamporesi, and G. Ferrari, *Creation and counting of defects in a temperature-quenched bose-einstein condensate,* Phys. Rev. A **94**, 023628 (2016).

[135] K. Damle, S. N. Majumdar, and S. Sachdev, *Phase ordering kinetics of the bose gas,* Phys. Rev. A **54**, 5037–5041 (1996).

[136] D. Chen, M. White, C. Borries, and B. DeMarco, *Quantum quench of an atomic mott insulator,* Phys. Rev. Lett. **106**, 235304 (2011).

[137] C. Meldgin, U. Ray, P. Russ, D. Chen, D. M. Ceperley, and B. DeMarco, *Probing the Bose glass-superfluid transition using quantum quenches of disorder,* Nat. Phys. **12**, 646 (2016).

[138] A. Keesling, A. Omran, H. Levine, H. Bernien, H. Pichler, S. Choi, R. Samajdar, S. Schwartz, P. Silvi, S. Sachdev, P. Zoller, M. Endres, M. Greiner, V. Vuletić, and M. D. Lukin, *Quantum kibble–zurek mechanism and critical dynamics on a programmable rydberg simulator,* Nature **568**, 207–211 (2019).

[139] P. Weinberg, M. Tylutki, J. M. Rönkkö, J. Westerholm, J. A. Åström, P. Manninen, P. Törmä, and A. W. Sandvik, *Scaling and diabatic effects in quantum annealing with a d-wave device,* Phys. Rev. Lett. **124**, 090502 (2020).

[140] Y. Bando, Y. Susa, H. Oshiyama, N. Shibata, M. Ohzeki, F. J. Gómez-Ruiz, D. A. Lidar, S. Suzuki, A. del Campo, and H. Nishimori, *Probing the universality of topological defect formation in a quantum annealer: Kibble-zurek mechanism and beyond,* Phys. Rev. Research **2**, 033369 (2020).

[141] A. D. King, S. Suzuki, J. Raymond, A. Zucca, T. Lanting, F. Altomare, A. J. Berkley, S. Ejtemaee, E. Hoskinson, S. Huang, E. Ladizinsky, A. MacDonald, G. Marsden, T. Oh, G. Poulin-Lamarre, M. Reis, C. Rich, Y. Sato, J. D. Whittaker, J. Yao, R. Harris, D. A. Lidar, H. Nishimori, and M. H. Amin, *Coherent quantum annealing in a programmable 2000-qubit ising chain,* (2022).

[142] S. Braun, M. Friesdorf, S. S. Hodgman, M. Schreiber, J. P. Ronzheimer, A. Riera, M. del Rey, I. Bloch, J. Eisert, and U. Schneider, *Emergence of coherence*

and the dynamics of quantum phase transitions, Proceedings of the National Academy of Sciences **112**, 3641 (2015).

[143] K. Shimizu, Y. Kuno, T. Hirano, and I. Ichinose, *Dynamics of a quantum phase transition in the bose-hubbard model: Kibble-zurek mechanism and beyond,* Phys. Rev. A **97**, 033626 (2018).

[144] I. Bloch, *Ultracold quantum gases in optical lattices,* Nature Physics **1**, 23 (2005).

[145] I. Bloch, J. Dalibard, and W. Zwerger, *Many-body physics with ultracold gases,* Rev. Mod. Phys. **80**, 885 (2008).

[146] I. Bloch, J. Dalibard, and S. Nascimbène, *Quantum simulations with ultracold quantum gases,* Nature Physics **8**, 267–276 (2012).

[147] C. J. Pethick and H. Smith, *Bose-Einstein condensation in Dilute Gases* (Cambridge University Press (New York), 2002).

[148] M. Ueda, *Fundamentals and New Frontiers of Bose-Einstein Condensation* (World Scientific, 2010).

[149] R. O. Umucal ılar and E. J. Mueller, *Fractional quantum hall states in the vicinity of mott plateaus,* Phys. Rev. A **81**, 053628 (2010).

[150] R. Bai, S. Bandyopadhyay, S. Pal, K. Suthar, and D. Angom, *Bosonic quantum Hall states in single-layer two-dimensional optical lattices,* Phys. Rev. A **98**, 023606 (2018).

[151] D. Jaksch and P. Zoller, *The cold atom Hubbard toolbox,* Annals of Physics **315**, 52 (2005).

[152] M. Lewenstein, A. Sanpera, V. Ahufinger, B. Damski, A. Sen(De), and U. Sen, *Ultracold atomic gases in optical lattices: mimicking condensed matter physics and beyond,* Adv. Phys. **56**, 243 (2007).

[153] O. Dutta, M. Gajda, P. Hauke, M. Lewenstein, D.-S. Lhmann, B. A. Malomed, T. Sowiski, and J. Zakrzewski, *Non-standard Hubbard models in optical lattices: a review,* Reports on Progress in Physics **78**, 066001 (2015).

[154] J. M. Zhang and R. X. Dong, *Exact diagonalization: the bose–hubbard model as an example,* European Journal of Physics **31**, 591–602 (2010).

[155] D. Raventós, T. Graß, M. Lewenstein, and B. Juliá-Díaz, *Cold bosons in optical lattices: a tutorial for exact diagonalization,* Journal of Physics B: Atomic, Molecular and Optical Physics **50**, 113001 (2017).

[156] D. S. Rokhsar and B. G. Kotliar, *Gutzwiller projection for bosons,* Phys. Rev. B **44**, 10328 (1991).

[157] K. Sheshadri, H. R. Krishnamurthy, R. Pandit, and T. V. Ramakrishnan, *Superfluid and insulating phases in an interacting-boson model: Mean-field theory and the RPA,* EPL **22**, 257 (1993).

[158] W. Krauth, M. Caffarel, and J.-P. Bouchaud, *Gutzwiller wave function for a model of strongly interacting bosons,* Phys. Rev. B **45**, 3137–3140 (1992).

[159] D. van Oosten, P. van der Straten, and H. T. C. Stoof, *Quantum phases in an optical lattice,* Phys. Rev. A **63**, 053601 (2001).

[160] D.-S. Lühmann, *Cluster gutzwiller method for bosonic lattice systems,* Phys. Rev. A **87**, 043619 (2013).

[161] B. Capogrosso-Sansone, i. m. c. G. m. c. Söyler, N. Prokof'ev, and B. Svistunov, *Monte carlo study of the two-dimensional bose-hubbard model,* Phys. Rev. A **77** (2008).

[162] P. Anders, E. Gull, L. Pollet, M. Troyer, and P. Werner, *Dynamical mean-field theory for bosons,* New Journal of Physics **13**, 075013 (2011).

[163] G. Semerjian, M. Tarzia, and F. Zamponi, *Exact solution of the Bose-Hubbard model on the bethe lattice,* Phys. Rev. B **80**, 014524 (2009).

[164] J. K. Freericks and H. Monien, *Phase diagram of the Bose-Hubbard model,* Europhysics Letters (EPL) **26**, 545 (1994).

[165] N. Teichmann, D. Hinrichs, M. Holthaus, and A. Eckardt, *Process-chain approach to the Bose-Hubbard model: Ground-state properties and phase diagram,* Phys. Rev. B **79**, 224515 (2009).

[166] N. Dupuis and K. Sengupta, *Superfluid to mott-insulator transition of cold atoms in optical lattices,* Physica B: Condensed Matter **404**, 517–520 (2009).

[167] D. Stauffer and A. Aharony, *Introduction To Percolation Theory* (Taylor and Francis, 1992).

[168] M. Sahimi and A. G. Hunt, *Complex Media and Percolation Theory* (Springer, New York, NY, 2021).

[169] M. E. J. Newman and R. M. Ziff, *Efficient monte carlo algorithm and high-precision results for percolation,* Phys. Rev. Lett. **85**, 4104–4107 (2000).

[170] A. Newell and J. C. Shaw, *Programming the logic theory machine,* in "Proceedings of the Western Joint Computer Conference," (Association for Computing Machinery (New York), 1957).

[171] R. M. Ziff, P. T. Cummings, and G. Stells, *Generation of percolation cluster perimeters by a random walk,* Journal of Physics A: Mathematical and General **17**, 3009–3017 (1984).

[172] R. M. Ziff, *Hull-generating walks,* Physica D: Nonlinear Phenomena **38**, 377–383 (1989).

[173] J. Hoshen and R. Kopelman, *Percolation and cluster distribution. i. cluster multiple labeling technique and critical concentration algorithm,* Phys. Rev. B **14**, 3438 (1976).

[174] J. Hoshen, M. W. Berry, and K. S. Minser, *Percolation and cluster structure parameters: The enhanced hoshen-kopelman algorithm,* Phys. Rev. E **56**, 1455–1460 (1997).

[175] S. Frijters, T. Krüger, and J. Harting, *Parallelised hoshen-kopelman algorithm for lattice-boltzmann simulations,* Computer Physics Communications **189**, 92–98 (2015).

[176] J. M. Constantin, M. W. Berry, and B. T. V. Zanden, *Parallelization of the hoshen-kopelman algorithm using a finite state machine,* The International Journal of Supercomputer Applications and High Performance Computing **11**, 34–48 (1997).

[177] N. R. Moloney and G. Pruessner, *Asynchronously parallelized percolation on distributed machines,* Phys. Rev. E **67**, 037701 (2003).

[178] J. Teuler and J. Gimel, *A direct parallel implementation of the hoshen-kopelman algorithm for distributed memory architectures,* Computer Physics Communications **130**, 118–129 (2000).

[179] N. Sendra, T. Gwizdałła, and J. Czerbniak, *Reducing algorithm for percolation cluster analysis,* Annales Universitatis Mariae Curie-Sklodowska, sectio AI–Informatica **5**, 87–91 (2006).

[180] R. Moreira and M. Barrufet, *Spatial distribution of oil after deep-fat frying of tortilla chips from a stochastic model,* Journal of Food Engineering **27**, 279–290 (1996).

[181] L. Zhang and N. Seaton, *Simulation of catalyst fouling at the particle and reactor levels,* Chemical Engineering Science **51**, 3257–3272 (1996).

[182] M. Berry, J. Comiskey, and K. Minser, *Parallel analysis of clusters in landscape ecology,* IEEE Computational Science and Engineering **1**, 24–38 (1994).

[183] F. Eddi, J. Mariani, and G. Waysand, *Transient synaptic redundancy in the developing cerebellum and isostatic random stacking of hard spheres,* Biological Cybernetics **74**, 139–146 (1996).

[184] J. Martín-Herrero, *Hybrid object labelling in digital images,* Machine Vision and Applications **18**, 1–15 (2007).

[185] G. Mazzarella, S. M. Giampaolo, and F. Illuminati, *Extended bose hubbard model of interacting bosonic atoms in optical lattices: From superfluidity to density waves,* Phys. Rev. A **73**, 013625 (2006).

[186] O. Jürgensen, F. Meinert, M. J. Mark, H.-C. Nägerl, and D.-S. Lühmann, *Observation of density-induced tunneling,* Phys. Rev. Lett. **113**, 193003 (2014).

[187] D.-S. Lhmann, O. Jrgensen, and K. Sengstock, *Multi-orbital and density-induced tunneling of bosons in optical lattices,* New Journal of Physics **14**, 033021 (2012).

[188] D. Johnstone, N. Westerberg, C. W. Duncan, and P. Öhberg, *Staggered ground states in an optical lattice,* Phys. Rev. A **100**, 043614 (2019).

[189] T. Wang and T. Ying, *Benchmark study of the sf-mi phase transition of the bose-hubbard model with density-induced tunneling,* Physics Letters A **383**, 680–683 (2019).

[190] R. Kraus, K. Biedroń, J. Zakrzewski, and G. Morigi, *Superfluid phases induced by dipolar interactions,* Phys. Rev. B **101**, 174505 (2020).

[191] K. Suthar, R. Kraus, H. Sable, D. Angom, G. Morigi, and J. Zakrzewski, *Staggered superfluid phases of dipolar bosons in two-dimensional square lattices,* Phys. Rev. B **102**, 214503 (2020).

[192] M. Iskin, *Route to supersolidity for the extended Bose-Hubbard model,* Phys. Rev. A **83**, 051606 (2011).

[193] M. Iskin, *Artificial gauge fields for the Bose-Hubbard model on a checkerboard superlattice and extended Bose-Hubbard model,* Eur. Phys. J. B **85**, 76 (2012).

[194] D. Yamamoto, A. Masaki, and I. Danshita, *Quantum phases of hardcore bosons with long-range interactions on a square lattice,* Phys. Rev. B **86**, 054516 (2012).

[195] T. McIntosh, P. Pisarski, R. J. Gooding, and E. Zaremba, *Multisite mean-field theory for cold bosonic atoms in optical lattices,* Phys. Rev. A **86**, 013623 (2012).

[196] D. R. Hofstadter, *Energy levels and wave functions of bloch electrons in rational and irrational magnetic fields,* Phys. Rev. B **14**, 2239–2249 (1976).

[197] H. Miyake, G. A. Siviloglou, C. J. Kennedy, W. C. Burton, and W. Ketterle, *Realizing the Harper Hamiltonian with laser-assisted tunneling in optical lattices,* Phys. Rev. Lett. **111**, 185302 (2013).

[198] M. Atala, M. Aidelsburger, M. Lohse, J. T. Barreiro, B. Paredes, and I. Bloch, *Observation of chiral currents with ultracold atoms in bosonic ladders,* Nature (London) **10**, 588 (2014).

[199] C. J. Kennedy, W. C. Burton, W. C. Chung, and W. Ketterle, *Observation of Bose-Einstein condensation in a strong synthetic magnetic field,* Nature (London) **11**, 859 (2015).

[200] O. Boada, A. Celi, J. I. Latorre, and V. Picó, *Simulation of gauge transformations on systems of ultracold atoms,* New Journal of Physics **12**, 113055 (2010).

[201] G. Möller and N. R. Cooper, *Condensed ground states of frustrated Bose-Hubbard models,* Phys. Rev. A **82**, 063625 (2010).

[202] D. A. Abanin, E. Altman, I. Bloch, and M. Serbyn, *Colloquium: Many-body localization, thermalization, and entanglement,* Rev. Mod. Phys. **91**, 021001 (2019).

[203] T. Kibble, *Some implications of a cosmological phase transition,* Physics Reports **67**, 183 (1980).

[204] W. Zurek, *Cosmological experiments in condensed matter systems,* Physics Reports **276**, 177 (1996).

[205] A. Polkovnikov, *Universal adiabatic dynamics in the vicinity of a quantum critical point,* Phys. Rev. B **72**, 161201 (2005).

[206] R. Schützhold, M. Uhlmann, Y. Xu, and U. R. Fischer, *Sweeping from the superfluid to the mott phase in the bose-hubbard model,* Phys. Rev. Lett. **97**, 200601 (2006).

[207] J. Dziarmaga, *Dynamics of a quantum phase transition: Exact solution of the quantum ising model,* Phys. Rev. Lett. **95**, 245701 (2005).

[208] V. Mukherjee, U. Divakaran, A. Dutta, and D. Sen, *Quenching dynamics of a quantum xy spin-$\frac{1}{2}$ chain in a transverse field,* Phys. Rev. B **76**, 174303 (2007).

[209] F. M. Cucchietti, B. Damski, J. Dziarmaga, and W. H. Zurek, *Dynamics of the bose-hubbard model: Transition from a mott insulator to a superfluid,* Phys. Rev. A **75**, 023603 (2007).

[210] H. Saito, Y. Kawaguchi, and M. Ueda, *Kibble-zurek mechanism in a quenched ferromagnetic bose-einstein condensate,* Phys. Rev. A **76**, 043613 (2007).

[211] L. Cincio, J. Dziarmaga, M. M. Rams, and W. H. Zurek, *Entropy of entanglement and correlations induced by a quench: Dynamics of a quantum phase transition in the quantum ising model,* Phys. Rev. A **75**, 052321 (2007).

[212] K. Sengupta, D. Sen, and S. Mondal, *Exact results for quench dynamics and defect production in a two-dimensional model,* Phys. Rev. Lett. **100**, 077204 (2008).

[213] J. Dziarmaga, J. Meisner, and W. H. Zurek, *Winding up of the wave-function phase by an insulator-to-superfluid transition in a ring of coupled bose-einstein condensates,* Phys. Rev. Lett. **101**, 115701 (2008).

[214] C. De Grandi, V. Gritsev, and A. Polkovnikov, *Quench dynamics near a quantum critical point,* Phys. Rev. B **81**, 012303 (2010).

[215] F. Pollmann, S. Mukerjee, A. G. Green, and J. E. Moore, *Dynamics after a sweep through a quantum critical point,* Phys. Rev. E **81**, 020101 (2010).

[216] S. Sharma, S. Suzuki, and A. Dutta, *Quenches and dynamical phase transitions in a nonintegrable quantum ising model,* Phys. Rev. B **92**, 104306 (2015).

[217] M. M. Rams, J. Dziarmaga, and W. H. Zurek, *Symmetry breaking bias and the dynamics of a quantum phase transition,* Phys. Rev. Lett. **123**, 130603 (2019).

[218] R. Puebla, O. Marty, and M. B. Plenio, *Quantum kibble-zurek physics in long-range transverse-field ising models,* Phys. Rev. A **100**, 032115 (2019).

[219] A. Sinha, M. M. Rams, and J. Dziarmaga, *Kibble-zurek mechanism with a single particle: Dynamics of the localization-delocalization transition in the aubry-andré model,* Phys. Rev. B **99**, 094203 (2019).

[220] D. Sen, K. Sengupta, and S. Mondal, *Defect production in nonlinear quench across a quantum critical point,* Phys. Rev. Lett. **101**, 016806 (2008).

[221] L. E. Sadler, J. M. Higbie, S. R. Leslie, M. Vengalattore, and D. M. Stamper-Kurn, *Spontaneous symmetry breaking in a quenched ferromagnetic spinor bose–einstein condensate,* Nature **443**, 312 (2006).

[222] L. W. Clark, L. Feng, and C. Chin, *Universal space-time scaling symmetry in the dynamics of bosons across a quantum phase transition,* Science **354**, 606–610 (2016).

[223] B. Gardas, J. Dziarmaga, W. H. Zurek, and M. Zwolak, *Defects in quantum computers,* Scientific Reports **8**, 4539 (2018).

[224] O. Morsch and M. Oberthaler, *Dynamics of bose-einstein condensates in optical lattices,* Rev. Mod. Phys. **78**, 179–215 (2006).

[225] G. Lamporesi, S. Donadello, S. Serafini, F. Dalfovo, and G. Ferrari, *Spontaneous creation of kibble–zurek solitons in a bose–einstein condensate,* Nature Physics **9**, 656 (2013).

[226] B. Damski and W. H. Zurek, *Quantum phase transition in space in a ferromagnetic spin-1 bose–einstein condensate,* New Journal of Physics **11**, 063014 (2009).

[227] B. Damski and W. H. Zurek, *Soliton creation during a bose-einstein condensation,* Phys. Rev. Lett. **104**, 160404 (2010).

[228] J. Beugnon and N. Navon, *Exploring the kibble–zurek mechanism with homogeneous bose gases,* Journal of Physics B: Atomic, Molecular and Optical Physics **50**, 022002 (2017).

[229] A. Eckardt, C. Weiss, and M. Holthaus, *Superfluid-insulator transition in a periodically driven optical lattice,* Phys. Rev. Lett. **95**, 260404 (2005).

[230] K. Shimizu, T. Hirano, J. Park, Y. Kuno, and I. Ichinose, *Out-of-equilibrium dynamics of multiple second-order quantum phase transitions in an extended bose-hubbard model: Superfluid, supersolid, and density wave,* Phys. Rev. A **98**, 063603 (2018).

[231] Y. Zhou, Y. Li, R. Nath, and W. Li, *Quench dynamics of rydberg-dressed bosons on two-dimensional square lattices,* Phys. Rev. A **101**, 013427 (2020).

[232] A. del Campo, G. De Chiara, G. Morigi, M. B. Plenio, and A. Retzker, *Structural defects in ion chains by quenching the external potential: The inhomogeneous kibble-zurek mechanism,* Phys. Rev. Lett. **105**, 075701 (2010).

[233] A. del Campo, A. Retzker, and M. B. Plenio, *The inhomogeneous kibble–zurek mechanism: vortex nucleation during bose–einstein condensation,* New Journal of Physics **13**, 083022 (2011).

[234] F. J. Gómez-Ruiz and A. del Campo, *Universal dynamics of inhomogeneous quantum phase transitions: Suppressing defect formation,* Phys. Rev. Lett. **122**, 080604 (2019).

[235] Y. Machida and K. Kasamatsu, *Application of the inhomogeneous kibble-zurek mechanism to quench dynamics in the transition from a mott insulator to a superfluid in a finite system,* Phys. Rev. A **103**, 013310 (2021).

[236] G. Biroli, L. F. Cugliandolo, and A. Sicilia, *Kibble-zurek mechanism and infinitely slow annealing through critical points,* Phys. Rev. E **81**, 050101 (2010).

[237] K. Jeong, B. Kim, and S. J. Lee, *Growth kinetics of the two-dimensional ising model with finite cooling rates,* Phys. Rev. E **99**, 022113 (2019).

[238] K. Roychowdhury, R. Moessner, and A. Das, *Dynamics and correlations at a quantum phase transition beyond kibble-zurek,* Phys. Rev. B **104**, 014406 (2021).

[239] J. Dziarmaga, M. Tylutki, and W. H. Zurek, *Quench from mott insulator to superfluid,* Phys. Rev. B **86**, 144521 (2012).

[240] B. Damski and W. H. Zurek, *Adiabatic-impulse approximation for avoided level crossings: From phase-transition dynamics to landau-zener evolutions and back again,* Phys. Rev. A **73**, 063405 (2006).

[241] K. Shimizu, T. Hirano, J. Park, Y. Kuno, and I. Ichinose, *Dynamics of first-order quantum phase transitions in extended bose–hubbard model: from density wave to superfluid and vice versa,* New Journal of Physics **20**, 083006 (2018).

[242] J. Stuhler, A. Griesmaier, T. Koch, M. Fattori, T. Pfau, S. Giovanazzi, P. Pedri, and L. Santos, *Observation of dipole-dipole interaction in a degenerate quantum gas,* Phys. Rev. Lett. **95**, 150406 (2005).

[243] B. Pasquiou, G. Bismut, E. Maréchal, P. Pedri, L. Vernac, O. Gorceix, and B. Laburthe-Tolra, *Spin relaxation and band excitation of a dipolar Bose-Einstein condensate in 2d optical lattices,* Phys. Rev. Lett. **106**, 015301 (2011).

[244] Y. Tang, N. Q. Burdick, K. Baumann, and B. L. Lev, *BoseEinstein condensation of 162 dy and 160 dy,* New Journal of Physics **17**, 045006 (2015).

[245] C. Ospelkaus, S. Ospelkaus, L. Humbert, P. Ernst, K. Sengstock, and K. Bongs, *Ultracold heteronuclear molecules in a 3d optical lattice,* Phys. Rev. Lett. **97**, 120402 (2006).

[246] A. Chotia, B. Neyenhuis, S. A. Moses, B. Yan, J. P. Covey, M. Foss-Feig, A. M. Rey, D. S. Jin, and J. Ye, *Long-lived dipolar molecules and feshbach molecules in a 3d optical lattice,* Phys. Rev. Lett. **108**, 080405 (2012).

[247] A. Frisch, M. Mark, K. Aikawa, S. Baier, R. Grimm, A. Petrov, S. Kotochigova, G. Quéméner, M. Lepers, O. Dulieu, and F. Ferlaino, *Ultracold dipolar molecules composed of strongly magnetic atoms,* Phys. Rev. Lett. **115**, 203201 (2015).

[248] I. Danshita and C. A. R. Sá de Melo, *Stability of superfluid and supersolid phases of dipolar bosons in optical lattices,* Phys. Rev. Lett. **103**, 225301 (2009).

[249] C. Zhang, A. Safavi-Naini, A. M. Rey, and B. Capogrosso-Sansone, *Equilibrium phases of tilted dipolar lattice bosons,* New Journal of Physics **17**, 123014 (2015).

[250] H.-K. Wu and W.-L. Tu, *Competing quantum phases of hard-core bosons with tilted dipole-dipole interaction,* Phys. Rev. A **102**, 053306 (2020).

[251] T. Ohgoe, T. Suzuki, and N. Kawashima, *Quantum phases of hard-core bosons on two-dimensional lattices with anisotropic dipole-dipole interaction,* Phys. Rev. A **86**, 063635 (2012).

[252] K. Binder, *Theory of first-order phase transitions,* Reports on Progress in Physics **50**, 783–859 (1987).

[253] I. B. Coulamy, A. Saguia, and M. S. Sarandy, *Dynamics of the quantum search and quench-induced first-order phase transitions,* Phys. Rev. E **95**, 022127 (2017).

[254] L.-Y. Qiu, H.-Y. Liang, Y.-B. Yang, H.-X. Yang, T. Tian, Y. Xu, and L.-M. Duan, *Observation of generalized kibble-zurek mechanism across a first-order quantum phase transition in a spinor condensate,* Science Advances **6** (2020).

[255] H.-Y. Liang, L.-Y. Qiu, Y.-B. Yang, H.-X. Yang, T. Tian, Y. Xu, and L.-M. Duan, *Observation of heat scaling across a first-order quantum phase transition in a spinor condensate,* New Journal of Physics **23**, 033038 (2021).

[256] S. Scopa and S. Wald, *Dynamical off-equilibrium scaling across magnetic first-order phase transitions,* Journal of Statistical Mechanics: Theory and Experiment **2018**, 113205 (2018).

[257] A. Sinha, T. Chanda, and J. Dziarmaga, *Nonadiabatic dynamics across a first-order quantum phase transition: Quantized bubble nucleation,* Phys. Rev. B **103**, L220302 (2021).

[258] G. Lagnese, F. M. Surace, M. Kormos, and P. Calabrese, *False vacuum decay in quantum spin chains,* Phys. Rev. B **104**, L201106 (2021).

[259] M. Campostrini, A. Pelissetto, and E. Vicari, *Finite-size scaling at quantum transitions,* Phys. Rev. B **89**, 094516 (2014).

[260] H. Panagopoulos and E. Vicari, *Off-equilibrium scaling behaviors across first-order transitions,* Phys. Rev. E **92**, 062107 (2015).

[261] A. Pelissetto and E. Vicari, *Dynamic finite-size scaling at first-order transitions,* Phys. Rev. E **96**, 012125 (2017).

[262] A. Pelissetto, D. Rossini, and E. Vicari, *Out-of-equilibrium dynamics driven by localized time-dependent perturbations at quantum phase transitions,* Phys. Rev. B **97**, 094414 (2018).

[263] A. Pelissetto, D. Rossini, and E. Vicari, *Finite-size scaling at first-order quantum transitions when boundary conditions favor one of the two phases,* Phys. Rev. E **98**, 032124 (2018).

[264] A. Pelissetto, D. Rossini, and E. Vicari, *Scaling properties of the dynamics at first-order quantum transitions when boundary conditions favor one of the two phases,* Phys. Rev. E **102**, 012143 (2020).

[265] D. Rossini and E. Vicari, *Coherent and dissipative dynamics at quantum phase transitions,* Physics Reports **936**, 110 (2021).

[266] N. Shitara, S. Bir, and P. B. Blakie, *Domain percolation in a quenched ferromagnetic spinor condensate,* New Journal of Physics **19**, 095003 (2017).

[267] P. W. Anderson, *Absence of diffusion in certain random lattices,* Phys. Rev. **109**, 1492 (1958).

[268] B. Kramer and A. MacKinnon, *Localization: theory and experiment,* Reports on Progress in Physics **56**, 1469–1564 (1993).

[269] T. Vojta, *Rare region effects at classical, quantum and nonequilibrium phase transitions,* Journal of Physics A: Mathematical and General **39** (2006).

[270] T. Vojta, *Quantum griffiths effects and smeared phase transitions in metals: Theory and experiment,* Journal of Low Temperature Physics **161**, 299–323 (2010).

[271] T. Vojta, *Phases and phase transitions in disordered quantum systems,* AIP Conference Proceedings **1550**, 188–247 (2013).

[272] T. Vojta, *Disorder in quantum many-body systems,* Annual Review of Condensed Matter Physics **10**, 233–252 (2019).

[273] A. Barman, S. Dutta, A. Khan, and S. Basu, *Understanding the bose glass phase via a percolation scenario,* The European Physical Journal B **86**, 308 (2013).

[274] S. N. Nabi and S. Basu, *Percolation analysis of a disordered spinor bose gas,* Journal of Physics B: Atomic, Molecular and Optical Physics **49**, 125301 (2016).

[275] P. Buonsante, V. Penna, A. Vezzani, and P. B. Blakie, *Mean-field phase diagram of cold lattice bosons in disordered potentials,* Phys. Rev. A **76**, 011602 (2007).

[276] L. Pollet, *A review of monte carlo simulations for the bosehubbard model with diagonal disorder,* Comptes Rendus Physique **14**, 712–724 (2013).

[277] A. E. Niederle and H. Rieger, *Superfluid clusters, percolation and phase transitions in the disordered, two-dimensional Bose-Hubbard model,* New J. Phys. **15**, 075029 (2013).

[278] N. Prokof'ev and B. Svistunov, *Superfluid-insulator transition in commensurate disordered bosonic systems: Large-scale worm algorithm simulations,* Phys. Rev. Lett. **92**, 015703 (2004).

[279] K. G. Balabanyan, N. Prokof'ev, and B. Svistunov, *Superfluid-insulator transition in a commensurate one-dimensional bosonic system with off-diagonal disorder,* Phys. Rev. Lett. **95**, 055701 (2005).

[280] P. Sengupta and S. Haas, *Quantum glass phases in the disordered Bose-Hubbard model,* Phys. Rev. Lett. **99**, 050403 (2007).

[281] A. M. Piekarska and T. K. Kopeć, *Quantum glass of interacting bosons with off-diagonal disorder,* Phys. Rev. Lett. **120**, 160401 (2018).

[282] H. Gimperlein, S. Wessel, J. Schmiedmayer, and L. Santos, *Ultracold atoms in optical lattices with random on-site interactions,* Phys. Rev. Lett. **95**, 170401 (2005).

[283] S. Gimperlein, H.and Wessel, J. Schmiedmayer, and L. Santos, *Random on-site interactions versus random potential in ultra cold atoms in optical lattices,* Applied Physics B **82**, 217–224 (2006).

[284] A. E. Niederle and H. Rieger, *Bosons in a two-dimensional bichromatic quasiperiodic potential: Analysis of the disorder in the bose-hubbard parameters and phase diagrams,* Phys. Rev. A **91**, 043632 (2015).

[285] A. Goldman and Y. Liu, *The two-dimensional superconductor-insulator transition,* Physica D: Nonlinear Phenomena **83**, 163–177 (1995).

[286] P. A. Crowell, J. D. Reppy, S. Mukherjee, J. Ma, M. H. W. Chan, and D. W. Schaefer, *Critical behavior of superfluid* ^{4}He *films adsorbed in aerogel glass,* Phys. Rev. B **51**, 12721–12736 (1995).

[287] D. Clément, A. F. Varón, M. Hugbart, J. A. Retter, P. Bouyer, L. Sanchez-Palencia, D. M. Gangardt, G. V. Shlyapnikov, and A. Aspect, *Suppression of transport of an interacting elongated bose-einstein condensate in a random potential,* Phys. Rev. Lett. **95**, 170409 (2005).

[288] D. Clément, P. Bouyer, A. Aspect, and L. Sanchez-Palencia, *Density modulations in an elongated bose-einstein condensate released from a disordered potential,* Phys. Rev. A **77**, 033631 (2008).

[289] M. White, M. Pasienski, D. McKay, S. Q. Zhou, D. Ceperley, and B. DeMarco, *Strongly interacting bosons in a disordered optical lattice,* Phys. Rev. Lett. **102**, 055301 (2009).

[290] B. Damski, J. Zakrzewski, L. Santos, P. Zoller, and M. Lewenstein, *Atomic bose and anderson glasses in optical lattices,* Phys. Rev. Lett. **91**, 080403 (2003).

[291] L. Fallani, J. E. Lye, V. Guarrera, C. Fort, and M. Inguscio, *Ultracold atoms in a disordered crystal of light: Towards a bose glass,* Phys. Rev. Lett. **98**, 130404 (2007).

[292] U. Gavish and Y. Castin, *Matter-wave localization in disordered cold atom lattices,* Phys. Rev. Lett. **95**, 020401 (2005).

[293] M. Pasienski, D. McKay, M. White, and B. DeMarco, *A disordered insulator in an optical lattice,* Nat. Phys. **6**, 677 (2010).

[294] B. Gadway, D. Pertot, J. Reeves, M. Vogt, and D. Schneble, *Glassy behavior in a binary atomic mixture,* Phys. Rev. Lett. **107**, 145306 (2011).

[295] R. Yu, C. F. Miclea, F. Weickert, R. Movshovich, A. Paduan-Filho, V. S. Zapf, and T. Roscilde, *Quantum critical scaling at a bose-glass/superfluid transition: Theory and experiment for a model quantum magnet,* Phys. Rev. B **86**, 134421 (2012).

[296] K. V. Krutitsky, A. Pelster, and R. Graham, *Mean-field phase diagram of disordered bosons in a lattice at nonzero temperature,* New J. Phys. **8**, 187 (2006).

[297] U. Bissbort and W. Hofstetter, *Stochastic mean-field theory for the disordered bose-hubbard model,* EPL (Europhysics Letters) **86**, 50007 (2009).

[298] U. Bissbort, R. Thomale, and W. Hofstetter, *Stochastic mean-field theory: Method and application to the disordered bose-hubbard model at finite temperature and speckle disorder,* Phys. Rev. A **81**, 063643 (2010).

[299] M. Makivić, N. Trivedi, and S. Ullah, *Disordered bosons: Critical phenomena and evidence for new low energy excitations,* Phys. Rev. Lett. **71**, 2307–2310 (1993).

[300] i. m. c. G. Söyler, M. Kiselev, N. V. Prokof'ev, and B. V. Svistunov, *Phase diagram of the commensurate two-dimensional disordered bose-hubbard model,* Phys. Rev. Lett. **107**, 185301 (2011).

[301] J.-W. Lee, M.-C. Cha, and D. Kim, *Phase diagram of a disordered boson hubbard model in two dimensions,* Phys. Rev. Lett. **87**, 247006 (2001).

[302] J. K. Freericks and H. Monien, *Strong-coupling expansions for the pure and disordered bose-hubbard model,* Phys. Rev. B **53**, 2691–2700 (1996).

[303] R. V. Pai, R. Pandit, H. R. Krishnamurthy, and S. Ramasesha, *One-dimensional disordered bosonic Hubbard model: A density-matrix renormalization group study,* Phys. Rev. Lett. **76**, 2937 (1996).

[304] S. Rapsch, U. Schollwöck, and W. Zwerger, *Density matrix renormalization group for disordered bosons in one dimension,* EPL **46**, 559 (1999).

[305] M. Gerster, M. Rizzi, F. Tschirsich, P. Silvi, R. Fazio, and S. Montangero, *Superfluid density and quasi-long-range order in the one-dimensional disordered bose–hubbard model,* New Journal of Physics **18**, 015015 (2016).

[306] P. Buonsante, F. Massel, V. Penna, and A. Vezzani, *Glassy features of a bose glass,* Laser Physics **18**, 653–658 (2008).

[307] R. Roth and K. Burnett, *Superfluidity and interference pattern of ultracold bosons in optical lattices,* Phys. Rev. A **67**, 031602 (2003).

[308] J. P. Álvarez Zúñiga, D. J. Luitz, G. Lemarié, and N. Laflorencie, *Critical properties of the superfluid—bose-glass transition in two dimensions,* Phys. Rev. Lett. **114**, 155301 (2015).

[309] A. Johansson, *anjohan/fortperc: 0.1.0,* (2022).

[310] J. Zakrzewski, *Mean-field dynamics of the superfluid-insulator phase transition in a gas of ultracold atoms,* Phys. Rev. A **71**, 043601 (2005).

[311] K. V. Krutitsky, J. Larson, and M. Lewenstein, *Dark solitons near the mott-insulator–superfluid phase transition,* Phys. Rev. A **82**, 033618 (2010).

[312] K. V. Krutitsky and P. Navez, *Excitation dynamics in a lattice bose gas within the time-dependent gutzwiller mean-field approach,* Phys. Rev. A **84**, 033602 (2011).

[313] T. Saito, I. Danshita, T. Ozaki, and T. Nikuni, *Detecting the superfluid critical momentum of bose gases in optical lattices through dipole oscillations,* Phys. Rev. A **86**, 023623 (2012).

[314] R. Bai, D. Gaur, H. Sable, S. Bandyopadhyay, K. Suthar, and D. Angom, *Segregated quantum phases of dipolar bosonic mixtures in two-dimensional optical lattices,* Phys. Rev. A **102**, 043309 (2020).

[315] M. Malakar, S. Ray, S. Sinha, and D. Angom, *Phases and collective modes of bosons in a triangular lattice at finite temperature: A cluster mean field study,* Phys. Rev. B **102**, 184515 (2020).

List of Publications

1. **Hrushikesh Sable**, Deepak Gaur, and D. Angom, *Fine-grained domain counting and percolation analysis in 2D lattice systems with linked-lists*,
   arXiv preprint arXiv:2112.15527 (2021).

2. **Hrushikesh Sable**, Deepak Gaur, Soumik Bandyopadhyay, Rejish Nath, and D. Angom, *Quantum quench dynamics of tilted dipolar bosons in 2D optical lattices*,
   arXiv preprint arXiv:2106.01725 (2021).

3. Kuldeep Suthar, **Hrushikesh Sable**, Rukmani Bai, Soumik Bandyopadhyay, Sukla Pal, and D Angom, *Supersolid phase of the extended Bose-Hubbard model with an artificial gauge field*,
   Phys. Rev. A **102**, 013320 (2020).

4. **Hrushikesh Sable**, Deepak Gaur, and D Angom, *Emergence of structured quantum phases with variable range of range of long-range dipolar interactions*,
   (under preparation).

5. Soumik Bandyopadhyay, **Hrushikesh Sable**, Deepak Gaur, Rukmani Bai, and D Angom, *Quantum phases of dipolar bosons in multilayer optical lattice*,
   arXiv preprint arXiv:2106.14430 (2021).

6. Kuldeep Suthar, Rebecca Kraus, **Hrushikesh Sable**, D Angom, Giovanna Morigi, and Jakub Zakrzewski, *Staggered superfluid phases of dipolar bosons in two-dimensional square lattices*,
   Phys. Rev. B **102**, 214503 (2020).

7. Rukmani Bai, Deepak Gaur, **Hrushikesh Sable**, Soumik Bandyopadhyay, Kuldeep. Suthar, and D. Angom, *Segregated quantum phases of dipolar bosonic mixtures in two-dimensional optical lattices*,
   Phys. Rev. A **102**,043309 (2020).

Publications attached with thesis

1. Kuldeep Suthar, **Hrushikesh Sable**, Rukmani Bai, Soumik Bandyopadhyay, Sukla Pal, and D Angom,
   Supersolid phase of the extended Bose-Hubbard model with an artificial gauge field,
   Phys. Rev. A **102**, 013320 (2020).
   doi: 10.1103/PhysRevA.102.013320

2. **Hrushikesh Sable**, Deepak Gaur, and D. Angom,
   Fine-grained domain counting and percolation analysis in 2D lattice systems with linked-lists,
   arXiv preprint arXiv:2112.15527 (2021).
   10.48550/ARXIV.2112.15527

3. **Hrushikesh Sable**, Deepak Gaur, Soumik Bandyopadhyay, Rejish Nath, and D. Angom, *Quantum quench dynamics of tilted dipolar bosons in 2D optical lattices*,
   arXiv preprint arXiv:2106.01725 (2021).
   10.48550/ARXIV.2106.01725